harender thesis plagiarism.pdf

Delhi Technological University

Document Details

Submission ID
trn:oid:::27535:126242208

Submission Date
Jan 15, 2026, 3:05 PM GMT+5:30

Download Date
Jan 15, 2026, 3:08 PM GMT+5:30

File Name
harender thesis plagiarism.pdf

File Size
3.6 MB

90 Pages

29,089 Words

150,630 Characters

6% Overall Similarity

The combined total of all matches, including overlapping sources, for each database.

Filtered from the Report

- Bibliography
- Quoted Text
- Small Matches (less than 14 words)

Exclusions

- 2 Excluded Sources

Match Groups

59 Not Cited or Quoted 5%
Matches with neither in-text citation nor quotation marks

14 Missing Quotations 1%
Matches that are still very similar to source material

0 Missing Citation 0%
Matches that have quotation marks, but no in-text citation

0 Cited and Quoted 0%
Matches with in-text citation present, but no quotation marks

Top Sources

5% Internet sources
3% Publications
1% Submitted works (Student Papers)

Integrity Flags

0 Integrity Flags for Review

No suspicious text manipulations found.

Our system's algorithms look deeply at a document for any inconsistencies that would set it apart from a normal submission. If we notice something strange, we flag it for you to review.

A Flag is not necessarily an indicator of a problem. However, we'd recommend you focus your attention there for further review.

Match Groups

- **59** Not Cited or Quoted 5%
  Matches with neither in-text citation nor quotation marks
- **14** Missing Quotations 1%
  Matches that are still very similar to source material
- **0** Missing Citation 0%
  Matches that have quotation marks, but no in-text citation
- **0** Cited and Quoted 0%
  Matches with in-text citation present, but no quotation marks

Top Sources

5% Internet sources
3% Publications
1% Submitted works (Student Papers)

Top Sources

The sources with the highest number of matches within the submission. Overlapping sources will not be displayed.

1	Internet	dspace.dtu.ac.in:8080 3%
2	Internet	vdoc.pub 1%
3	Internet	www.physics.uiowa.edu <1%
4	Internet	www.science.gov <1%
5	Publication	P.K Shukla, A.A Mamun. "Introduction to Dusty Plasma Physics", CRC Press, 2019 <1%
6	Publication	Kavita Rani Segwal, Suresh C. Sharma. "A Nonlocal Theory of Current-Driven Low-... <1%
7	Internet	merlino.lab.uiowa.edu <1%
8	Internet	www.mpe.mpg.de <1%
9	Internet	asmedigitalcollection.asme.org <1%
10	Publication	B M Annaratone. "A note on the potential acquired by a dust particle in an electro... <1%

11 Internet

erewhon.superkuh.com <1%

12 Publication

Bivash Dolai, Ram Prasad Prajapati. "Kelvin-Helmholtz instability in sheared dust... <1%

13 Publication

Bivash Dolai, R. P. Prajapati. "Rayleigh-Taylor instability and internal waves in str... <1%

14 Submitted works

Noakhali Science and Technology University on 2025-12-17 <1%

15 Publication

P. K. Shukla, B. Eliasson. " : Fundamentals of dust-plasma interactions ", Reviews ... <1%

16 Publication

S. Tarofder, A. Mannan, A.A. Mamun. "Solitary wave solution of (3+1)-dimensional ... <1%

17 Internet

en.wikipedia.org <1%

18 Internet

epdf.tips <1%

19 Publication

Chitrita Dasgupta, Sarit Maitra. "Vortex in a strongly coupled dusty plasma embe... <1%

20 Internet

eprints.lancs.ac.uk <1%

21 Publication

A Garscadden. Plasma Sources Science and Technology, 08/1994 <1%

22 Publication

Chengkai Li, Youyou Kang, Yunliang Wang. "The combined effects of quantum an... <1%

23 Publication

M. S. Rahman, A. A. Mamun. "Adiabatic effects on nonlinear dust-acoustic solitary... <1%

Chapter 1

Introduction

1.1 Plasma

“In the beginning was the plasma" [1]. Alfvén concluded his Nobel lecture in 1970 with this statement to remind us of the origin of both ourselves and our environment. In the early 19th century, Michael Faraday proposed the existence of a fourth state of matter. He observed that physical properties of substances (shape, softness, colour, opacity etc.) are gradually diminishing during phase transitions, from solids to liquids to gases. Faraday hypothesized that this trend of decreasing properties did not abruptly end with the gaseous state. He believed that matter could undergo a further transformation beyond the gaseous state, a change as significant as the transition from liquid to gas. He termed this hypothetical state "radiant matter." [2] William Crookes linked Faraday's concept of "radiant matter" to the phenomena he observed in low-pressure electrical discharges [3]. J.J. Thomson's discovery of the electron provided an explanation for the phenomena observed by Crookes in low-pressure electrical discharges. This marked the first discovery of a subatomic particle. Thomson's work suggested that the "fourth state of matter" was composed of a mixture of positively and negatively charged particles. In the early 20th century, Irving Langmuir further developed this understanding and established the field of plasma physics.

Gas molecules break apart into atoms when the kinetic energy of the particles surpasses the molecular binding energy. With further increases in kinetic energy (or temperature), the atomic gas becomes ionized. When the level of ionization is high enough, this state is referred to as plasma. Plasma typically exists at high temperatures and low pressures, conditions that are rarely found on Earth. It is a conducting gas composed of electrons, ions, and some neutral particles, with the overall electric charge of the system being zero (Quasi-neutrality). Plasma is not merely a hot and disordered state of matter; it can also exist in gaseous, liquid, and even crystalline solid forms.

It is often stated that 99% of the universe is composed of plasma (such as stars and the interplanetary medium). Consequently, space plasma physics has become a well-established field of research.

1.1.1 Dust in Plasma

A dusty plasma refers to a mixture of electrons, ions, neutral atoms and charged dust grains with their size ranging between nanometre to several hundred microns. Dust grains possess extremely large masses on the order of 10^{12} times that of a proton. A key feature that makes dusty plasma research scientifically significant and technologically relevant is that these grains accumulate substantial electric charge, typically becoming negatively charged. This occurs because the grains interact far more frequently with fast-moving electrons than with the comparatively slow ions present in the plasma. The charge acquired by dust particles of about 1 μm in size, typically lies in the range of 10^3 e to 10^4 e, where e denotes the elementary charge.

Dust grains exist in two configurations isolated and non-isolated. This is decided by the length scales and the Havnes parameter, $H = \frac{Z_d n_d}{n_i}$, it tells about the extent to which dust grains contribute to the overall charge balance of the plasma by comparing the charge carried by dust to that carried by the ions. The dust grains are said to be Isolated when their radius is much smaller than both the plasma Debye length (λ_D) and the average distance between neighbouring grains (a_d) i.e. $, a \ll \lambda_D < a_d$ and hold much less charge than the background plasma $|H| \approx 0$

In this regime, individual grains doesn't have significant impact on the overall plasma behavior. However, when the grain size or density is such that these separations become comparable i.e. $a \ll a_d < \lambda_D$ and the charge contained in the dust component becomes comparable to that in the ion–electron population (i.e. $|H| \geq 0$), the grains can be considered as non-isolated. Now, they participate collectively and begin to influence the plasma behaviour in significant ways.

Once dust particles interact collectively with the surrounding charged species, they not only alter conventional plasma wave modes—such as ion-acoustic waves (IAW), electrostatic ion cyclotron waves (EIC), and lower-hybrid waves (LHW) but also support entirely new modes, including dust-acoustic waves (DAW) and dust ion-acoustic waves (DIAW). In addition, the presence of charged dust can modify or drive various instabilities, including ion-streaming, Kelvin-Helmholtz (KH), and Rayleigh-Taylor (RT) instabilities [4]. A proper understanding of this collective behavior requires first understanding the fundamental properties of dust particles, their production mechanisms, and the processes through which they acquire charge.

1.2 Characteristics and Phenomena in Dusty Plasma

1.2.1 Quasi neutrality

In the absence of external forces, a dusty plasma remains neutral on a macroscopical scale, just like the ordinary plasma. Thus, under equilibrium conditions, the system satisfies the expression of neutrality of charge

$$en_{0i} - en_{0e} + Q_d n_{0d} \approx 0 , \qquad (1.1)$$

where n_{0i}, n_{0e} and n_{0e} are the no. density of ion, electron, and dust in equilibrium state, e is the elementary charge on electron, and $Q_d = \pm Z_d e$ represents the charge on a dust grain (here, Z_d is charge state $\sim$ 10^3-10^4). However, in many astrophysical and laboratory plasmas situations, heavy charging of dust grains can reduce the electron population, sometimes depleting it almost entirely.

1.2.2 Debye Screening length

One of the characteristic properties of a plasma is its ability to screen an electric potential by forming a Debye sphere, a process known as Debye shielding. The radius of this Debye sphere, called the Debye length, represents the distance upto which the electric field of a charged particle can influence other charges in the plasma. In a dusty plasma, a positive potential becomes surrounded by electrons and negatively charged dust grains, while a negative potential is screened by ions and any positively charged grains. In the case of perfect shielding in cold plasma the surrounding charge cloud remains unperturbed. However, at some finite temperatures charged particles near the boundary of the cloud acquire enough thermal energy to escape, allowing a potential of the magnitude $k_B T / e$ to leak into the plasma. This leads to incomplete shielding and a finite residual electric field. The approximate thickness of this shielding region, or sheath, is also characterized by the Debye length. The expression for the Debye length is given as [4],

$$\lambda_D = \frac{\lambda_{eD}\lambda_{iD}}{\sqrt{\lambda_{eD}^2 + \lambda_{iD}^2}}, \tag{1.2}$$

where $\lambda_{eD} = \left(T_e / 4\pi n_{0e} e^2\right)^{1/2}$ and $\lambda_{iD} = \left(T_i / 4\pi n_{0i} e^2\right)^{1/2}$ are electron and ion Debye lengths, respectively.

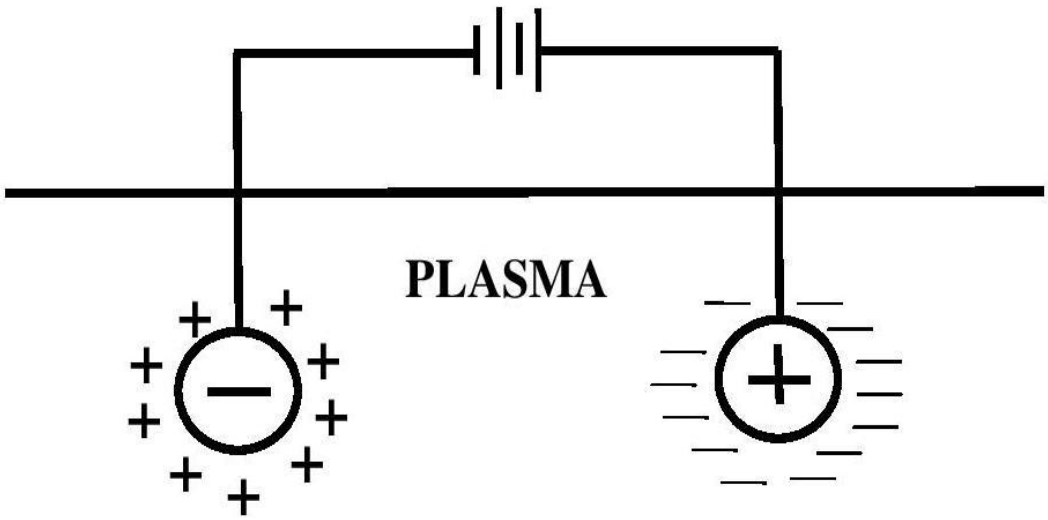

Fig. 1.1 Debye Screening [5]

1.2.3 Characteristic frequencies

When plasma particles are displaced from their equilibrium positions, charge separation occurs, leading to the formation of an electric field that acts to restore overall charge neutrality by driving the particles back toward equilibrium. Due to their finite inertia, the particles overshoot their equilibrium positions and are subsequently acted upon by an electric field of opposite polarity. This repeated overshooting results in sustained oscillatory motion about the equilibrium state.

The characteristic frequency of these oscillations differs for different plasma species, as it depends on the mass and charge of the respective species. For instance, electrons oscillate relative to ions with the electron plasma frequency $f_{ep} = \left(4\pi n_{0e} e^2 / m_e\right)^{1/2}$, ions oscillate relative to charged dust grains with the ion plasma frequency $f_{ip} = \left(4\pi n_{0i} e^2 / m_i\right)^{1/2}$, and dust grains undergo oscillations about their equilibrium positions with the dust plasma frequency $f_{dp} = \left(4\pi n_{0d} Z_d^2 e^2 / m_d\right)^{1/2}$.

1.2.4 Coulomb Coupling Parameter

The Coulomb coupling parameter is an important quantity used to distinguish between weakly and strongly coupled plasmas. It is defined as the ratio of the average electrostatic potential energy to the average thermal kinetic energy of neighbouring particles.

$$\Gamma = \frac{Q_d^2}{a_d T_d} exp\left(-\frac{a_d}{\lambda_D}\right), \tag{1.3}$$

where $|Q_d| = +Z_d e$ is the charge on dust grains, Z_d is the dust charge state, $a_d = \left(4\pi n_{0d}/3\right)^{-1/3}$ is intergrain spacing, n_{0d} is dust density, $\kappa = a_d/\lambda_D$ is the screening constant. The exponential term represents the screening of the dust particle upto the Debye length λ_D.

Dusty plasma configuration having $\Gamma \ll 1$ is considered weakly coupled, whereas a system with $\Gamma \gg 1$falls into the strongly coupled regime. In most laboratory situations, dust grains tend to be strongly coupled because they carry large charges and the system typically operates at low temperatures[4]. Additionally, neutral collisions allow the dust grains to cool efficiently to near room temperature. The coupling parameter Γ determines the physical state of the dusty plasma whether it will behave like a gas, a liquid, or a solid. For $\Gamma \ll 1$, the dust component is in a gaseous state; for $1<\Gamma<170$, it exhibits liquid-like behavior; and at $\Gamma = 170$, the system reaches the coulomb crystallization threshold beyond which plasma starts making crystals, or solid-like structures [6]. However, in certain dusty plasma experiments (e.g., DPX), dust has been observed to remain in a fluid state even for values as high as $\Gamma = 300$ [7].

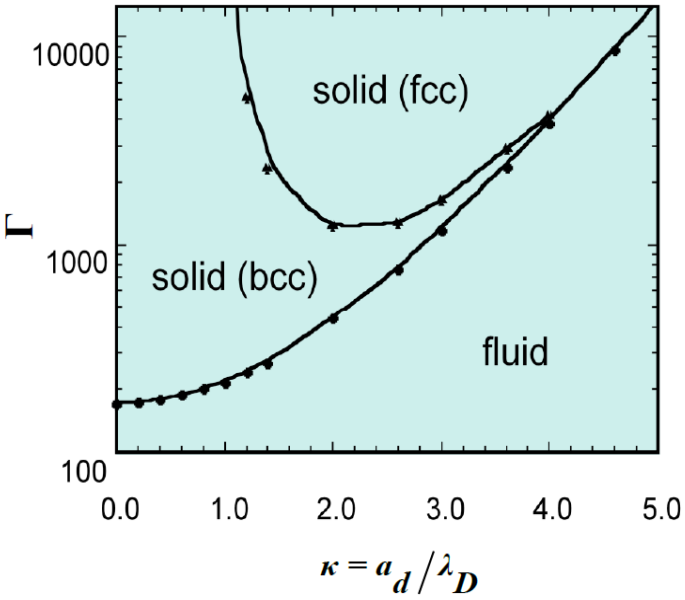

Fig. 1.2 Phase transition diagram for Yukawa system [8]

Strongly coupled dusty plasma systems are often referred to as Yukawa systems [8] because their behavior can be described using the Yukawa interaction potential $\phi = \frac{1}{r} exp\left(-\frac{r}{\lambda_D}\right)$.

Hamaguchi et al. [8] studied the phase transition temperatures corresponding to both fluid-solid and solid-solid phase boundaries, examining their dependence on the screening parameter κ. The triple point of a Yukawa system is illustrated in Fig. 1.2, it illustrates how increasing the coupling strength and the screening parameter drives the dusty plasma toward a more ordered, lattice-like state.

1.3 Dusty Plasma in Space

1.3.1 Ring System of Planets

The ring systems of the outer giant planets namely Jupiter, Saturn, Uranus, and Neptune consist primarily of micron sized dust particles. A brief overview is presented below to aid in understanding the origin and characteristics of dust particles in planetary rings

1.3.1.1 Jupiter's Ring System

Jupiter's ring system was initially identified by the Voyager 1 spacecraft using a specially targeted image designed to reveal very faint ring features. A more comprehensive set of observations was later obtained by Voyager 2. It is now established that Jupiter's ring system comprises of three main components: main ring, halo, and the gossamer ring. The main ring is approximately 7000 km wide and exhibits a sharp outer boundary located about 129,000 km from the planet's center. This region includes the orbital paths of the small satellites Adrastea and Metis, which are believed to be the primary sources of the dust particles that constitute most of the ring material.

1.3.1.2 Saturn's Ring System

Saturn's rings have intrigued astronomers since their initial discovery by Galileo in 1610 using one of the earliest telescopes. The complexity of this system became even more apparent following extensive imaging by the Voyager 1 and Voyager 2 missions in 1980 and 1981. The rings are designated by letter names based on their order of discovery, with the principal rings C, B, and A arranged outward from the planet. The Cassini Division, the largest gap in the ring system, separates the B and A rings. In addition, several lighter rings have been identified, including the D ring, which is extremely light and lies closest to Saturn; the narrow F ring just outside the A ring; and the more distant and faint G and E rings.

The particles composing Saturn's rings are predominantly icy in nature and range in size from microns to several meters. One of the most striking features observed by both Voyager missions was the presence of nearly radial structures known as spokes. These spokes, first reported by Smith et al. [9,10], provided strong motivation for detailed studies of dust–plasma interactions within planetary magnetospheres. The spokes are restricted upto the central B ring, extending from approximately 1.52 to 1.95 times Saturn's radius (R_S), with inner and outer boundaries near 1.72 R_S and the outer edge of the B ring, respectively. Typically exhibiting a wedge-like shape, these spokes are believed to consist of electrostatically levitated micron- and submicron-sized dust grains. Their radial elongation is attributed to the rapid radial transport of dense plasma clouds spanning several thousand kilometers in extent.

1.3.2 Earth Atmosphere

One of the most important regions of Earth's environment in which charged dust grains are found is the polar summer mesopause, located at altitudes between approximately 80 and 90 km [11,12]. A remarkable phenomenon associated with this region is the formation of noctilucent clouds (NLCs)**.** These clouds were first reported in 1885 by Backhouse [13] and were immediately recognized as being distinct from ordinary tropospheric clouds. Subsequent rocket experiments conducted during the International Geophysical Year (1957–1958) revealed an unusual feature of the polar mesopause: temperatures during summer were found to be significantly lower than those in winter. This unexpected result supported the idea that NLCs are composed of ice particles formed under extremely cold conditions, sometimes at temperatures below 100 K.

In addition to NLCs, other notable phenomena occur in the polar mesopause region, including polar mesospheric summer echoes (PMSE) and intense radar backscatter observed over a wide frequency range from 50 MHz to 1.3 GHz. At altitudes where PMSE are detected, layers of reduced electron density and enhanced positive ion density are commonly observed. These features have been discussed in detail in several review studies [11,14]. More recent theoretical models suggest that heavy ion clusters or charged dust particles may play a crucial role in these mesospheric phenomena, particularly when their total charge density becomes comparable to that of electrons or ions [12]. Such high charge densities may arise either from a small number of large dust particles carrying substantial charge or from dust grains that become positively charged through photoemission. In contrast, when photoelectron emission is weak and dust charging occurs primarily through the collection of plasma particles, the grains tend to carry only a small number of elementary charges and are usually negatively charged [12]. Typical plasma parameters associated with NLC environments include $n_e \sim 10^3 \text{cm}^{-3}$, $T_e \sim 150K$, $n_d \sim 10\ \text{cm}^{-3}$, dust grain radii a of about 0.1 μm, $n_n \sim 10^{14} cm^{-3}$ with $\kappa \approx 0.2$.

An important source of dust in Earth's upper atmosphere is particularly man-made pollution in the form of terrestrial aerosols. Studies have shown that nearly 90% of these particles consist of aluminium oxide (Al_2O_3) spheroids, having size between 0.1 μm to 10 μm. These particles primarily originate from rocket and space shuttle exhausts, highlighting the growing influence of anthropogenic activity on dusty plasma environments in near-Earth space (Bernhardt et al. 1995) [15].

1.3.3 Comets

These are small, fragile, and irregularly shaped celestial bodies that consist of a mixture of frozen gases and non-volatile solid dust particles. They move along an elliptical orbit that periodically carry them near Sun at perihelion before sending them far out into interplanetary space. Although cometary structures vary widely and are highly dynamic, all comets form a diffuse envelope of material known as the ***coma***, which grows larger and brighter as the comet approaches the Sun. At the center of the coma lies a compact and bright nucleus, typically less than 10 km in diameter. Together, the nucleus and the coma form what is referred to as the ***head*** of the comet. As a comet moves inward toward the Sun, it generates striking tails of glowing material that can stretch millions of kilometres away from the Sun. When the comet is located far from the Sun, its nucleus remains extremely cold and its constituents remain frozen. Once the comet enters within a few astronomical units (AU) of the Sun, solar heating of the nucleus surface initiates the sublimation of volatile substances.. These evaporating gases drag small solid particles away from the nucleus, forming a dense coma composed of gas and dust.

In the frozen state, the comet is visible only through reflected sunlight from its nucleus. As the coma develops, dust particles reflect additional sunlight, while gas molecules absorb ultraviolet radiation and re-emit it through fluorescence. At distances of roughly 5 AU from the Sun, this fluorescent emission generally becomes stronger than reflected light. Ultraviolet absorption also drives chemical reactions that release hydrogen atoms, which escape the comet's weak gravitational field and form an extended hydrogen envelope. Although this envelope cannot be observed from Earth due to atmospheric absorption, it has been detected by spacecraft.

Solar radiation pressure and the solar wind act on cometary material with different efficiencies depending on particle size and mass. Heavier dust particles are accelerated more slowly, producing broad, curved dust tails. In contrast, the much lighter ionized gas is rapidly accelerated by the solar wind, forming a narrow, nearly straight plasma tail pointing directly away from the Sun. Observations of comet Hale–Bopp, for example, clearly reveal two distinct tails: a thin blue plasma tail composed of ionized gases and a broader white tail consisting of macroscopic dust particles.

Space missions such as **Vega** and **Giotto** have greatly enhanced our understanding of cometary dust, revealing the presence of a large population of very small grains (VSGs) and providing valuable insights into dust–plasma interactions in cometary environments. These grains have been observed to follow a power-law size distribution, expressed as $n(r_d) \propto r_d^{-s}$, where the exponent s varies between approximately 3.3 for the Vega 2 mission and about 4.1 for the Giotto observations.

1.4 Dusty Plasma in Lab

The discussion on presence of dust particles in space plasma situations in previous section provides a strong foundation for understanding dusty plasmas under laboratory conditions. However, laboratory dusty plasmas differ from their space and astrophysical counterparts in two important ways. First, laboratory discharges are confined by physical boundaries whose geometry, material properties, temperature, and electrical conductivity strongly influence the generation, charging, and transport of dust grains. Second, the external electrical circuits used to sustain laboratory plasmas impose boundary conditions that vary in both space and time, thereby affecting the overall plasma dynamics.

In the following discussion, we outline the mechanisms by which dust is produced and sustained in laboratory plasma devices, with particular emphasis on direct current (DC) and radio-frequency (RF) discharges, plasma processing reactors, fusion plasma systems, and dust generated from solid-fuel combustion products.

1.4.1 DC and RF discharges

Although dust particles are present in direct current (DC) discharges, they are generally observed in much larger concentrations under radio-frequency (RF) excitation for the same working gases. This naturally raises the question of how dust particles are formed in such plasmas. Dust can originate either from gas-phase plasma chemistry for example, in discharges containing carbon monoxide or silane or from the sputtering of electrode materials such as metals or graphite. Experimental observations show that dust formation occurs more readily in electronegative gas mixtures or in plasmas containing substrates like silicon or carbon. Through sputtering, both silicon and carbon produce electronegative free radicals, and in order to maintain ambipolarity, the resulting dust particles acquire a negative charge.

RF discharges are particularly effective at trapping negative ions as well as macroscopic, negatively charged dust particles. This is primarily because the electrodes develop a negative DC self-bias which is a consequence of higher mobility of electrons than the positive ions. In addition, ambipolar electric fields arising in the radial direction again a consequence of mobility differences further confine negative ions and dust grains within the plasma. The physical characteristics of dust particles formed in DC or RF discharges, such as their growth, charge, spatial distribution, and temperature, depend on a variety of physical and chemical processes. These factors can be broadly categorized as follows [16]:

(i) **Growth:** influenced by radical and ion fluxes, bonding processes, temperature, desorption mechanisms, surface charging, and sputtering effects.

(ii) **Charge:** determined by the floating potential, electron and ion collection, electron affinity, work function, electrostriction, field and thermionic emission, and photoelectric charging processes.

(iii) **Position:** governed by the balance between electrostatic and gravitational forces, collisional drag due to ions and neutrals, collective polarizability effects, and particle mass.

(iv) **Temperature:** controlled by surface radical recombination, electron–ion recombination at the particle surface, and surface quenching of energetic plasma species.

1.4.2 Plasma Processing Reactors

The widespread use of low-pressure plasma processing reactors, combined with the ready availability of laser light–scattering diagnostics, has revealed that many such discharges generate and confine substantial quantities of macroscopic dust particles. Scanning electron microscopy (SEM) studies of these dust grains, performed using low-energy probes, show that the particles often exhibit narrow size distributions and morphologies resembling microscopic cauliflower-like structures, as illustrated in Fig. 1.3. Low-voltage SEM techniques are particularly important for resolving the surface features of materials with low atomic numbers, as they minimize charging and enhance image clarity.

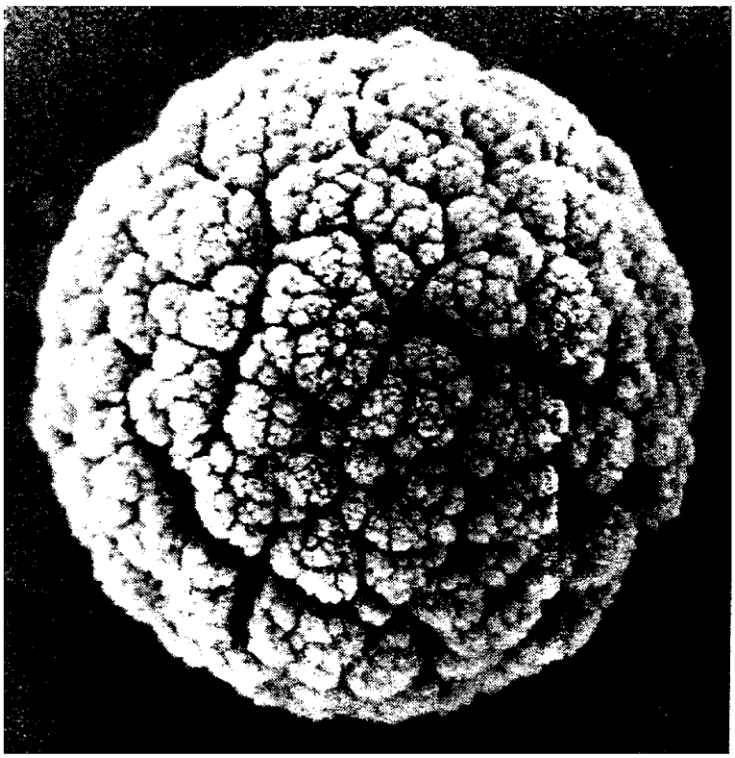

Fig. 1.3 Low-voltage, high-resolution SEM image showing a representative dust grain (~650 nm in diameter) formed in a helium plasma operated at 1 Torr and 15 kHz with graphite electrodes [16].

In addition, the use of low-voltage and low-current electron probes allows uncoated dust samples to be examined without causing beam-induced damage. Transmission electron microscopy (TEM) images of entire particles as well as thin cross-sections reveal radial, columnar microstructures, an absence of well-defined surface texture, and a lack of crystallinity on length scales of the order of 200 Å. The observed fractal morphology and surface characteristics resembles those of sputtered thin films deposited at surface temperatures below half of the melting temperature of the material. Such morphological features provide valuable insight into the nature of the particle and radical fluxes from which these homogeneously nucleated dust grains are formed.

1.4.3 Fusion plasma devices

The existence of dust particles in fusion devices has been recognized for many years, but their potential impact on plasma performance and reactor operation has only recently attracted significant attention [17–19]. In fusion systems such as tokamaks and stellarators, the plasma is inevitably contaminated by impurities that are heavier than the hydrogen isotopes used as fusion fuel. These impurities, often present in the form of dust particles, are produced through several mechanisms, including surface desorption, electrical arcing, sputtering, evaporation, and sublimation of plasma-facing components subjected to intense thermal loads.

In devices with graphite-based wall materials, the erosion processes release not only individual carbon atoms but also a substantial number of carbon clusters (C_1, C_2, C_3, …, C_n). Another important source of dust arises from the peeling or fragmentation of thin material layers that are either redeposited during plasma operation or intentionally applied for wall conditioning. Conditioning films, typically a few hundred nanometres thick, can break into fine flakes, while redeposited layers formed during tokamak operation may reach thicknesses of several hundred micrometres. These layers often exhibit a stratified structure due to repeated plasma discharges and become mechanically unstable once their thickness exceeds a few micrometres.

In fusion devices operating with deuterium–tritium (DT) fuel, additional dust-producing processes may occur. These include the generation of helium-3 from tritium decay, helium-4 formation due to neutron-induced spallation reactions in low-Z wall materials, and the release of dust particles caused by embrittlement of near-surface regions from energetic alpha particles. Dust formation is also likely during helium glow-discharge cleaning and during thin-film deposition processes used for wall conditioning, such as carbonization, boronization, and siliconization. After the termination of a fusion plasma discharge, most dust particles settle toward the bottom of the vessel. However, lighter particles can be reintroduced into the plasma either through magnetic forces or by electrostatic charging when they come into contact with the plasma edge. As a result, such particles may become levitated and remain suspended near the reactor walls.

1.5 Production Techniques of dusty plasma

Micron-sized dust grains, tend to settle at the bottom of a plasma due to their large mass, under the influence of gravity so external electrostatic or electromagnetic fields are employed to levitate and confine them [20]. In most laboratory plasma experiments, however, this limitation is not significant in most case because the relaxation time of microparticles is much longer than their charging time. As a result, dusty plasmas can often be produced simply by introducing dust grains directly into an existing plasma.

Over the years, several experimental techniques have been developed to produce dusty plasmas, depending on their specific application. These include dispersing dust particles into a plasma column using a Q-machine [21,22], growing dust within plasmas generated from chemically reactive gases such as silane (SiH_4) and oxygen (O_2) [23], or suspending negatively charged silica (SiO_2) particles of approximately 40 μm diameter in an argon glow discharge. More recently, magnetized dusty plasma experiment (MDPX) [7] was developed to analyse the behavior of fully magnetized dusty plasmas, with particular application to astrophysical and fusion plasma conditions. In the following sections, a brief overview of some selected laboratory techniques used to study dusty plasmas is presented.

1.5.1 Q-machine

A dusty plasma device (DPD) is based on a single-ended Q-machine that has been adapted to inject and distribute dust particles throughout the plasma column [21].The schematic diagram of a typical Q-machine is shown in Fig. 1.4. In this setup, a fully ionized potassium plasma column with a diameter of approximately 4 cm and a length of about 80 cm is produced by surface ionization of potassium atoms. Surface ionization takes place when an atom with a low ionization energy interacts with a metal surface that has a high work function.

These K atoms are emitted from an atomic beam oven onto a heated tantalum plate having a temperature around 2500 K. Radial confinement of the plasma column is achieved using a axial magnetic field of the order of $B_S \leq 4000$ gauss. The plasma density in the device ranges from 10^5-10^{10} cm^{-3}, with electrons and K^+ ions having nearly equal temperatures of about 0.2 eV. The pressure for neutrals is maintained at a low level (~10^{-6} Torr) to ensure that the mean free paths for electron-neutral and ion-neutral collisions exceed the physical dimensions of the Q-machine.

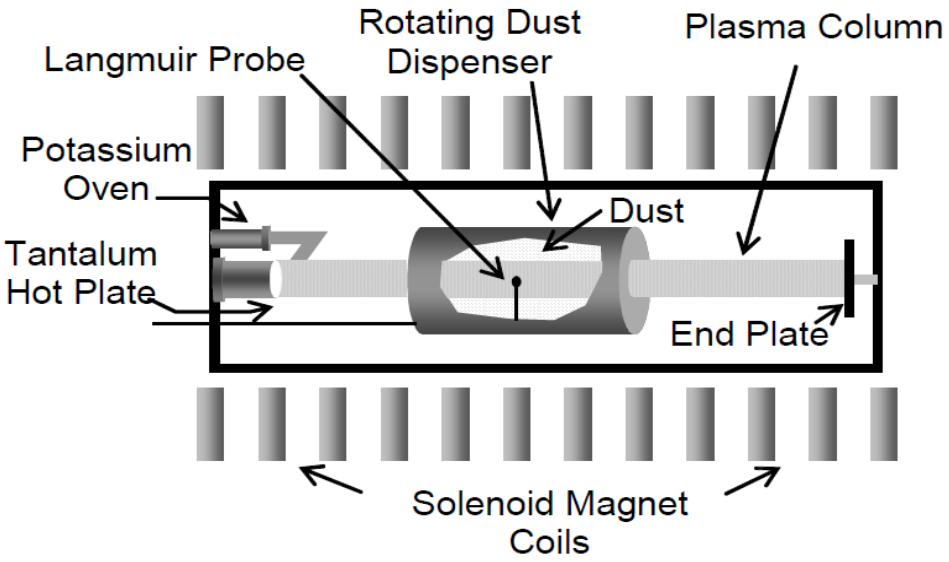

Fig. 1.4 Schematic of a Q-machine [22]

A section of the plasma column is encircled by a rotating dust dispenser comprising a rotating metal cylinder and a stationary screen. Dust particles are initially loaded at the bottom of the cylinder, from where they are transported upward during rotation and subsequently fall onto the screen. Stiff metal bristles mounted inside the cylinder scrape the outer surface of the screen, allowing uniform dispersal of dust grains into the plasma column. Dust particles that settle at the bottom are collected and recycled, which enables the continuous circulation and ensures a stable dust density within the plasma.

The dust commonly used in these experiments are alumina (Al_2O_3) and hydrated aluminum silicate (kaolin, $Al_2Si_2O_7 \cdot nH_2O$), which are available in various sizes and shapes. The dust samples are analysed using an electron microscope. The primary diagnostic instrument is a movable Langmuir probe, positioned perpendicular to the magnetic field and capable of

traversing along the axis of the plasma column to measure electron current and charge on floating dust grains. Q-machine setups thus provide an effective platform for investigating wave phenomena and instabilities in dusty plasmas.

1.5.2 RF discharge

In 1994, Chu and I [23] confined an RF plasma within a chamber of cylindrical symmetry and investigated the formation of dust crystals at low RF power. The schematic diagram of the device is shown in Fig. 1.5. The setup comprises a hollow outer electrode which is capacitively coupled to a 14 MHz RF power supply operating at approximately 30 W, It has a grounded central electrode with a ring-shaped groove at its top to confine dust particles. A glass window is provided at the top of the chamber for observation. Dust particles illuminated by a laser are monitored with the help of a CCD video camera.

A diffusion pump is used for the evacuation of the system. Silane (SiH_4) and oxygen (O_2) gases are introduced into the chamber with a background argon pressure of about 10 mTorr. The partial pressure of these reactive gases is maintained below 10 mTorr. An axial magnetic field in the range of 50–100 G is applied to enhance dust production efficiency. Both the size and number density of particles increase with the increase in flow rates and pressures of the reactive gases. Once dust particles are formed, the flow of reactive gases and the magnetic field are switched off [4]. Now the particles are trapped in the toroidal groove. Under the influence of gravity, the size of dust grains increases with decreasing height, with the vertical extent of the dust cloud limited to approximately 3 mm. Increasing the RF power results in the melting of the Coulomb crystal structure.

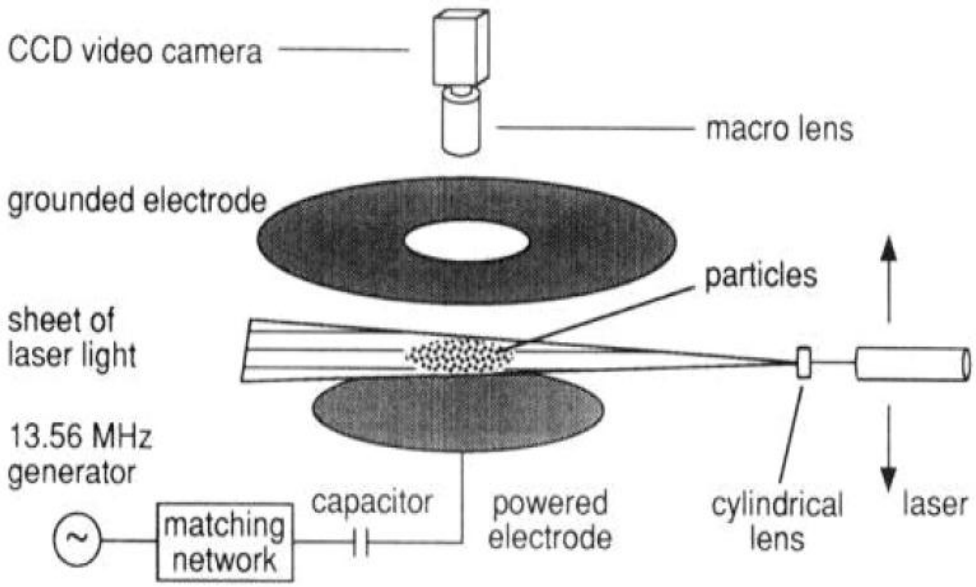

Fig. 1.5 RF Plasma setup which forms dust crystal at low RF power [23]

Plasma processing reactors commonly utilize RF discharge systems for the treatment of silicon wafers. In such environments, plasma-enhanced chemical reactions often result in the formation of unwanted negatively charged dust particles, primarily composed of SiO_2, which accumulate near the bottom of the plasma [24]. In addition to RF-based systems, various DC

glow discharge devices [25] have been developed to generate and confine micron-sized dust particles, enabling the observation of ordered dust structures and facilitating studies of dust acoustic wave (DAW) dispersion characteristics [26,27].

Furthermore, simple "salt-shaker" type [22] dust dispensers have been employed to introduce dust particles in a controlled manner. These setups allow measurements of the charge on individual dust grains, [28], investigation of dust-induced modifications to plasma wave propagation [29–31] and examination of ion and neutral drag forces acting on the dust particles [32].

1.6 Dust Charging Processes

In 1941, Spitzer was the first to describe the mechanisms responsible for dust grain charging in the interstellar medium [33]. Dust charging generally occurs through three primary processes [4]:

(i) interactions between dust grains and gaseous plasma constituents

(ii)interactions with energetic particles such as electrons and ions, and (iii) interactions between dust particles and photons.

When immersed in a plasma, dust grains acquire charge through the collection of electrons and ions, photoelectron emission induced by ultraviolet radiation, thermionic emission, secondary electron emission, and ion sputtering [34]. In this scenario, dust grains behave similarly to probes and attain a floating potential. So that, under equilibrium conditions, the net current on the grain surface arising from electrons (I_e), ions (I_i), secondary emission (I_{SE}), and photoemission I_{PE} vanishes,

$$\sum I = I_e + I_i + I_{SE} + I_{PE} \approx 0. \tag{1.4}$$

In laboratory plasmas, where photoemission and secondary electron emission currents are negligible, dust grains acquire a negative potential relative to the plasma due to the higher mobility of electrons compared to ions $\phi_S \left(= V_S - V_p\right)$. Dust charging continues until a balance between the electron current and ion current is achieved. Here, V_S denotes the grain surface potential and V_p the plasma potential.

However, the impact of energetic electrons or ions on the grain surface can lead to emission of secondary electrons, which makes the magnitude of grain potential positive . Similarly, photoemission of electrons from the dust surface also contributes to positive charging of the grains. Incorporating all of the charging mechanisms discussed above into a single description is highly challenging. Consequently, we focus on laboratory situations, where we have two limiting situations: (i) isolated and (ii) non-isolated dust grains.

1.6.1 Isolated dust grains

In low-temperature laboratory plasmas, dust grain charging is dominated by the collection of electrons and ions, while contributions from photoemission and secondary electron emission

are generally negligible. Because electrons move much faster than ions, dust grains initially accumulate negative charge through enhanced electron collection. As the grain potential becomes increasingly negative, it repels incoming electrons and simultaneously attracts positive ions, thereby increasing the ion current until a balance is reached between the electron and ion currents.

For isolated spherical dust grains of radius much smaller than the plasma Debye length $a \ll \lambda_D$ and with an inter-grain separation much larger than the Debye length $a_d \gg \lambda_D$, the grains attain a floating potential at which the net current to the surface vanishes. If V_S denotes the grain surface potential and I_e and I_i represent the magnitudes of the electron and ion currents to the dust grain, the equilibrium condition

$$\left(I_i - I_e\right)_{V=V_S} = 0 \tag{1.5}$$

must be satisfied. Under the assumptions of orbit–motion–limited (OML) theory [35–37], the electron

and ion currents in a Maxwellian plasma are given by

$$I_e = -en_{0e}\sqrt{\frac{k_B T_e}{2\pi m_e}}\exp\left(\frac{e\phi_S}{k_B T_e}\right)4\pi a^2 \tag{1.6}$$

and

$$I_i = en_{0i}\sqrt{\frac{k_B T_I}{2\pi m_I}}\left(1-\frac{e\phi_S}{k_B T_i}\right)4\pi a^2 . \tag{1.7}$$

Where n_{0e} & n_{0i} are the equilibrium electron and ion number densities, T_e & T_i are the electron and ion temperatures, and m_e & m_i denote the corresponding particle masses. These expressions remain valid provided the particle streaming velocities are smaller than their respective thermal velocities.

Balancing the electron and ion currents yields the floating potential given by

$$\exp\left(\frac{e\phi_S}{k_B T_e}\right) = \sqrt{\frac{m_e T_i}{m_i T_e}}\left(1-\frac{e\phi_S}{k_B T_i}\right). \tag{1.8}$$

For a hydrogen plasma, this relation takes a particular form $\phi_S\left(=-2.5k_B T_e/e\right)$, while for a singly ionized argon plasma $\phi_S\left(=-4.0k_B T_e/e\right)$ it differs due to the larger ion mass. The charge on the dust grain is $Q_d = C\phi_S$ where $C\left(=4\pi\varepsilon_0 a\right)$ is the grain capacitance. Figure 1.6 illustrates the normalized dust surface potential as a function of the electron-to-ion temperature ratio, as

reported by Merlino [22], showing that dust grains acquire a more negative potential in argon plasmas. Consequently, plasmas with heavier ions lead to enhanced electron attachment and increased negative charging of dust grains.

If secondary electron emission becomes significant, an additional current term must be included in the surface potential calculations, as described by Chow et al. [38]. However, the energy thresholds required to sustain secondary emission exceeding approximately 10 eV for electrons and 1 keV for ions impacting the dust surface are rarely met in typical laboratory plasmas. As a result, secondary emission currents can usually be neglected in such systems.

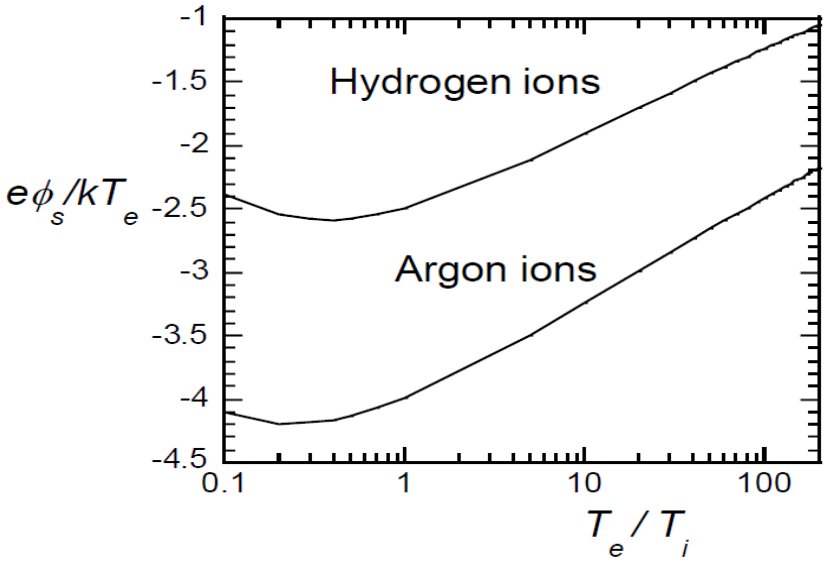

Fig. 1.6 The normalized dust surface potential relative to plasma as a function of electron to ion temperature ratio for Hydrogen and Argon ion plasmas [22]

In addition, dust charging due to the photoelectric emissions from the grain surface depends on several factors, namely: (i) the wavelength of the incident radiation, (ii) the material properties of the dust grains, and (iii) the surface area of dust particles. This mechanism becomes particularly significant when dust particles are exposed to ultraviolet radiation. Since the work functions of certain metals such as Ag, Cu, Al, Ca, and Cs are less than approximately 5 eV, photoelectron emission from these materials occurs readily.

Photoemission is therefore a dominant charging process in many astrophysical and near-Earth plasma environments, which are generally less dense, compared to laboratory plasmas, where higher densities suppress its influence. This mechanism typically results in positively charged dust grains. The photoemission current is given as [39]

$$I_{PE} = e\, J_P Q_A Y_{PE} \exp\left(-\frac{e\phi_S}{k_B T}\right)\pi a^2, \tag{1.9}$$

where J_P denotes the photon flux, Q_A is the photon absorption efficiency, Y_{PE} represents the photoemission yield, and T is the average temperature of the emitted photoelectrons.

In addition to photoemission, several other dust charging processes have been identified, including thermionic emission, field emission, radioactive emission, and impact ionization. The relevance of these mechanisms depends on the specific plasma environment and application under consideration.

1.6.2 Non-isolated dust grains

In the case of densely packed, non-isolated dust grains where the average inter-grain spacing is smaller than the plasma Debye length $a_d \le \lambda_D$ increasing the dust number density reduces the number of electrons available per grain. As a result, the magnitude of the dust surface potential relative to the plasma potential $\phi_S \left(= V_S - V_p\right)$ becomes smaller than that for isolated grains, leading to a reduction in the average dust charge. Under these conditions, the mean dust charge is determined by the use of charge neutrality condition [43] $en_{0i} = en_{0e} - Z_d en_{0d}$. The expressions for the electron and ion currents collected by negatively charged dust grains remain the same as those given in Eqs. (1.6) and (1.7).

Balancing the electron and ion currents under these circumstances yields the relation [40] given as

$$1 - Z_d \frac{n_{0d}}{n_{0i}} = \sqrt{\frac{m_e T_i}{m_i T_e}} \left(1 - \frac{e\phi_S}{k_B T_i}\right) \exp\left(-\frac{e\phi_S}{k_B T_e}\right). \tag{1.10}$$

For isolated grains, the relevant parameter satisfies $Z_d\, n_{0d}/n_{0i} \ll 1$, so the relative dust surface potential and the dust charge state Z_d depend only on the grain radius. In contrast, for non-isolated dust grains, where $Z_d\, n_{0d}/n_{0i} \sim 1$, both the dust potential and charge depend not only on grain size but also on dust density. When $T_i = T_e = T$ condition is applied, we get

$$\sqrt{\frac{m_i}{m_e}} \left(1 + \frac{4\pi\varepsilon_0}{e} P \frac{e\phi_S}{k_B T}\right) \exp\left(\frac{e\phi_S}{k_B T}\right) + \frac{e\phi_S}{k_B T} - 1 = 0, \tag{1.11}$$

where $P\left(= \frac{ak_B T}{e} \frac{n_{0d}}{n_{0i}}\right)$ is known as the Havnes parameter.

This expression describes how the dust surface potential and consequently the dust density varies with the Havnes parameter. The solution of this expression for a potassium K+ plasma gives a universal curve of normalized grain potential $\frac{e\phi_S}{k_B T}$ as a function of $\log P$, as shown in Fig. 1.7.

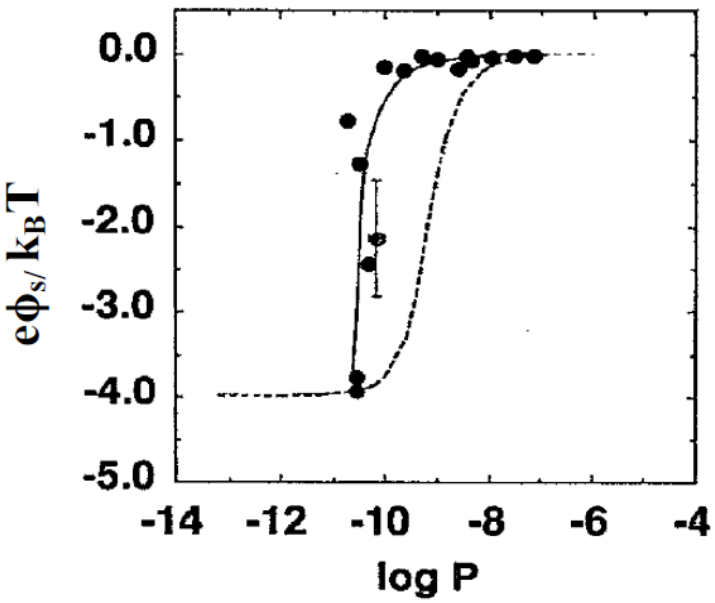

Fig. 1.7 The variation of relative grain potential $\frac{e\phi_S}{k_B T}$ vs. $\log P$ (The dashed line shows theoretical curve obtained from Eqn. (1.11) [35]

It clearly demonstrates that increasing dust density leads to reduced inter-grain spacing and a corresponding decrease in the average dust grain charge or surface potential. As the plasma density becomes large compared to the dust density (i.e., for small values of P), the grain potential approaches the isolated-grain potential $\phi_S \left(= -4.0 k_B T_e / e\right)$. Furthermore, by analysing the variation of the Havnes parameter P with dust radius a, the critical value of n_{0d}/n_{0i} beyond which the dust charge begins to decrease can be identified. This analysis shows that larger grains accumulate more charge than smaller ones, a result that is particularly important for understanding the transition between strongly and weakly coupled dusty plasma regimes, since the Coulomb coupling parameter increases strongly with dust grain charge.

1.7 Dust charge fluctuations

It is evident that any perturbation in the plasma currents can give rise to fluctuations in the dust grain charge, which in turn can lead to collective effects in the system [34]. The resulting dust charge fluctuations are expressed as

$$\frac{d}{dt} Q_{1d} = \frac{I_{1e}}{I_{0e}} + \frac{I_{1e}}{I_{0i}}, \tag{1.12}$$

where $Q_{1d} \left(= Q_d - Q_{0d}\right)$ represents the perturbed dust charge and I_{1e} & I_{1i} denotes the perturbed plasma currents. To observe collective behavior, the dust size is assumed to be much smaller than both the wavelength of the perturbations and the plasma Debye length. The evolution of dust charge fluctuations and their associated dynamics is governed by

$$\frac{dQ_{1d}}{dt}+\eta Q_{1d}=-\left|I_{0e}\right|\left(\frac{n_{1i}}{n_{0i}}-\frac{n_{1e}}{n_{0e}}\right), \tag{1.13}$$

where n_{1e} & n_{1i} are the perturbed electron and ion densities, respectively, and $\eta=\frac{\left|I_{0e}\right|e}{C_g}\left[\frac{1}{T_e}+\frac{1}{T_i-e\phi_{s0}}\right]$ is the dust charging rate. Here $C_g=\left[a\left(1+a/\lambda_{eD}\right)\right]$ denotes the dust grain capacitance, ϕ_{s0} is the equilibrium floating potential of the dust grains, and λ_{eD} is the electron Debye length. Equation (1.13) shows that dust charge fluctuations are driven by perturbations in the electron and ion densities and decay at a characteristic rate η. Physically, this decay occurs because any deviation of the grain potential from its equilibrium floating value induces plasma currents that act to restore the equilibrium state [35].

1.8 Dynamics of Dusty Plasma

Charged dust grains immersed in a plasma are subject to several forces that collectively determine their motion. These include electromagnetic forces, gravitational effects, ion and neutral drag forces, thermophoretic forces, and radiation pressure, among others. The motion of a dust grain with mass m_d and velocity v_d is therefore governed by a fundamental dynamical equation that accounts for the combined action of these forces, given as

$$m_d\frac{dv_d}{dt}=F_{EL}+F_G+F_D+F_T+F_P \tag{1.14}$$

Here, F_{EL} represents the electromagnetic force arising from the combined action of electric and magnetic fields. The gravitational force F_G accounts for gravitational attraction, either between dust grains themselves when they are sufficiently massive, or between a dust particle and a larger body such as a planet or satellite. The drag force F_D originates from momentum transfer due to collisions with plasma species or neutral particles and arises from the relative motion between the dust grain and the surrounding plasma or neutral gas. The thermophoretic force F_T is produced by temperature gradients in the neutral gas, while F_P denotes the radiation pressure force exerted on the dust grain.

1.8.1 Electromagnetic force

The electromagnetic force acting on a dust particle having charge q_d is given by the sum of two forces electric force and Lorentz force

$$F_{EL}=q_d\vec{E}+\frac{1}{c}\vec{u}_d\times\vec{B} \tag{1.15}$$

Where E is the electric Field and B is the magnetic field and $\vec{u}_d$ id the velocity of dust particle.

1.8.2 Gravitational Force

The gravitational force F_G acting on a dust grain generally arises from the combined contribution of three components. The first is the gravitational attraction exerted by a nearby planet, given by,

$$F_{Gp} = \frac{GM_P m_d}{r^2} \tag{1.16}$$

where G=6.672×10^{-8} dyn cm^{2}g^{-2} is the gravitational constant, m_d is the dust grain mass, M_P is the planetary mass, and r is the distance between the dust grain and the planet's center of mass. The second contribution arises from mutual gravitational attraction between dust grains themselves. This force is represented as:

$$F_{Gd} = \frac{Gm_d M_d}{r^2} \tag{1.17}$$

where m_d is the mass of first dust particle and M_d is the mass of a neighbouring dust grain and r is the separation between their centers of mass. The third component is the gravitational force due to a nearby satellite, which may be relevant in certain spatial configurations. This force is given by

$$F_{Gs} = \frac{Gm_d M_s}{r^2} \tag{1.18}$$

where M_s denotes the satellite mass and r is the distance from the dust grain to the satellite's center of mass. Accordingly, the total gravitational force acting on a dust grain can be written as

$$F_G = F_{Gp} + F_{Gd} + F_{Gs} \tag{1.19}$$

This formulation is valid under the assumption of spherical symmetry of the gravitational field; it is not applicable when significant deviations from spherical symmetry are present.

1.8.3 Drag Force

The drag force represents the rate at which momentum is exchanged between dust grains and the surrounding plasma. This transfer occurs either from the dust particles to the plasma species or from the plasma species(primarily ions and neutral atoms) to the dust grains. Collisions involving electrons are generally negligible because of their much smaller mass. Consequently, two main types of drag forces arise in a dusty plasma: the **ion drag force**, resulting from momentum transfer during interactions between positively charged ions and dust grains, and the **neutral drag force**, which originates from collisions between dust grains and neutral particles. These two drag mechanisms play a crucial role in governing dust grain dynamics and are described below.

The ion drag force has been examined extensively in the literature (e.g., Nitter, 1996; Boeuf and Punset, 1999) [41,42]. Momentum transfer from ions to a dust grain can occur through three primary mechanisms: direct ion collection via physical impacts with the grain, long-range electrostatic interactions through Coulomb scattering, and collective effects associated with ion fluid flow that modify the structure of the Debye sheath surrounding the dust particle.

The contribution arising from direct ion collection is referred to as the collection drag force F_{di}^{coll}, while the contribution due to Coulomb scattering is termed the Coulomb drag force F_{di}^{coul}. The force associated with ion flow–induced distortion of the sheath is known as the ion flow drag force F_{di}^{flow}. Accordingly, the total ion drag force acting on a dust grain can be written as

$$F_{di} = F_{di}^{coll} + F_{di}^{coul} + F_{di}^{flow} \tag{1.20}$$

The ion flow drag force F_{di}^{flow} is comparatively difficult to evaluate and generally contributes only weakly to the total ion drag force. Following earlier studies [43], this term is therefore neglected. The remaining components, namely the collection and Coulomb drag forces, can be evaluated as follows.

Consider a dusty plasma consisting of stationary dust grains immersed in a background of positive ions. The collection and Coulomb components of the ion drag force $F_{di}^{coll,coul}$ may be expressed as

$$F_{di}^{coll,coul} = n_i m_i \sigma^{coll,coul} V_{it} v_i \tag{1.21}$$

Where $\sigma^{coll}(\sigma^{coul})$ are the momentum transfer cross sections associated with ion collection and Coulomb scattering, respectively. Here, $V_{it} = \left(v_i + \frac{8k_b T_i}{\pi m_i} \right)^{1/2}$ represents the effective ion speed, incorporating both the directed ion velocity and the ion thermal speed.

1.8.4 Neutral Drag Force

The neutral drag force acting on dust grains originates from collisions with neutral gas particles, through which momentum is transferred from the neutral background to the dust component. When the neutral gas molecules follow a Maxwellian velocity distribution, in the regime when the relative speed $|v_d - v_n|$ is small the neutral drag force can be expressed as given by the Epstein expression[42,44].

$$F_{dn} = -\frac{8}{3}\sqrt{2\pi} r_d^{\,2} n_n m_n V_{Tn} (v_d - v_n) \tag{1.22}$$

Here r_d is the dust grain radius, V_{Tn} is the thermal speed of neutral, v_d is the speed of dust and v_n is speed of neutrals.

1.8.5 Thermophoretic Force

If we have a dust grain immersed in a neutral gas exhibiting a temperature gradient ∇T_n. Gas molecules originating from the hotter side of the grain possess higher thermal velocities than those from the cooler side. As a result, the momentum transferred to the dust particle from the hotter region exceeds that from the colder region. This imbalance leads to a net momentum transfer from the neutral gas to the dust grain. The force arising from this process is known as the **thermophoretic force** F_T.

The magnitude of the thermophoretic force is directly proportional to the neutral gas temperature gradient, and its direction coincides with the heat flux, i.e., it acts opposite to the direction of the temperature gradient. Talbot et al. (1980) [45] analytically derived an expression for this force by assuming that the non-uniform velocity distribution of the unperturbed neutral gas in the vicinity of the dust grain can be described using the Chapman–

Enskog formalism, and that the dust particle is sufficiently small to perturb this distribution. A physical interpretation of the thermophoretic force was later provided by Daugherty and Graves (1995) [46] in the context of particulate transport in glow discharge plasmas.
For a neutral gas with a non-uniform, unperturbed Chapman–Enskog velocity distribution, the thermophoretic force acting on a dust grain is given by (Talbot et al., 1980) Daugherty and Graves 1995 [45,46]

$$F_T = -\frac{8\sqrt{2\pi}}{15}\frac{r_d^2}{V_{Tn}}\left(1+\frac{5\pi}{32}(1-\alpha_{ac})\right)k_n^{con}\nabla T_n \tag{1.23}$$

Here k_n^{con} is thermal conductivity of neutral gas and α_{ac} is the accommodation coefficient.

1.8.6 Radiation Pressure Force

Dust grains, particularly in space environments, are continuously exposed to electromagnetic radiation emitted by various natural sources. As a result, an irradiated dust particle absorbs or scatters a portion of the incident radiation energy E_R, along with the associated momentum $P_R = \frac{E_R}{c}$. The transfer of this momentum to the dust grain gives rise to the radiation pressure force. To estimate this force, electromagnetic radiation may be treated as a stream of photons, each carrying an energy $E_R^{(1)} = \hbar\omega_R$ and a corresponding momentum $P_R^{(1)} = \frac{E_R^{(1)}}{c}$, where ω_R denotes the angular frequency of the radiation. The radiation intensity is characterized by the photon energy flux, defined as the energy transported per unit area per unit time, and is given by $I_o = N_{ph}\hbar\omega_R c$, where N_{ph} is the photon number density. The radiation pressure force acting on a spherical dust grain of radius r_d can then be written as [4]

$$F_R = \frac{\pi r_d^2}{c} I_o \hat{e}_r \tag{1.24}$$

where $\hat{e}_r$ is a unit vector directed along the incident radiation wave vector. If the radiation source is sufficiently distant to be approximated as a point source, the radiation pressure force acts along the line connecting the source to the dust grain.

1.8.7 Dust Polarisation force

The interaction between thermal plasma species (electrons and ions) and strongly charged dust particles gives rise to what is known as the *polarization force*. The origin and physical significance of this force acting on a charged dust grain were first discussed in detail by Hamaguchi and Farouki [47]. Mathematically, the polarization force F_p experienced by a dust particle can be expressed as [48,49]

$$F_p = -\frac{q_d^2\nabla\lambda_D}{2\lambda_D^2} \tag{1.25}$$

Where q_d is the charge on dust and $\lambda_D = \lambda_{eD}\lambda_{id} / (\lambda_{iD}^2 + \lambda_{eD}^2)^{1/2}$ is the linearized Debye radius.

and $\lambda_{iD} = (T_i / 4\pi e^2 n_i)^{1/2}$, $\lambda_{eD} = (T_e / 4\pi e^2 n_e)^{1/2}$ are the ion and electron Debye length.

In typical laboratory dusty plasma conditions satisfying $n_e T_i \ll n_i T_e$, the total force acting on a charged dust particle arises from the combined contributions of the electrostatic force $q\vec{E} = -q\nabla\phi$ and the polarization force given in Eq. (1.25). The resulting net force on the dust grain can therefore be written as [48]

$$F = -q_d \nabla\phi (1 - P) \tag{1.26}$$

where the polarization parameter **P** is defined as $P = (1/4)(|q_d|e / \lambda_d T_i) \times (1 - T_i / T_e)$.

1.9 Model Description for Dusty Plasma Medium

The conditions required for strong coupling are readily satisfied in dusty plasma systems, which makes their theoretical description particularly challenging. In this section, we briefly review the principal approaches that have been developed to model dusty plasma media under different coupling regimes.

1.9.1 Quasilocalized Charge Approximation (QLCA) Approach

As discussed earlier, dusty plasmas can exist in gaseous, liquid, or solid-like states depending on the value of the Coulomb coupling parameter Γ. Weakly coupled dusty plasmas ($\Gamma \ll 1$) behave similarly to conventional fluid plasmas and can often be described using a Vlasov-type formalism. In contrast, strongly coupled dusty plasmas ($\Gamma \gg 1$) exhibit solid-like behavior, where collective excitations resemble phonon modes in crystalline lattices rather than fluid waves.

The quasilocalized charge approximation (QLCA) is based on the assumption that dust particles become temporarily localized due to strong inter-particle correlations, within a time scale determined by the relaxation time. These localization sites evolve slowly and rearrange over longer time scales, justifying the term *quasilocalized*. A detailed formulation of the QLCA framework can be found in the work of Kalman et al. [50] and references therein.

In the QLCA picture, particles are assumed to be trapped in fluctuating potential wells that are randomly distributed throughout the system but remain spatially correlated. Dust grains oscillate within these transient potential wells, leading to the excitation of collective phonon-like modes. Over time, the potential wells dissolve and re-form in new configurations, allowing the particles to diffuse away from their temporary equilibrium positions [50,51] .

An important assumption of the QLCA approach is that the amplitudes of particle oscillations both intrinsic and externally driven remain smaller than the average inter-particle spacing. This condition corresponds to the harmonic approximation used in phonon theory and restricts the applicability of QLCA to linear response analyses in strongly coupled plasmas. By construction, the QLCA framework is not suitable for weakly coupled regimes and is most reliable for higher values of the coupling parameter ($\Gamma \gtrsim 10$), near the onset of localization. The

approach has been successful in describing both longitudinal and transverse collective modes in Coulomb and Yukawa systems [52].

1.9.2 Molecular Dynamics (MD) Simulation Approach

In the molecular dynamics (MD) approach, the exact trajectories of individual particles are computed by solving their equations of motion under a specified interaction potential. Dusty plasmas typically consist of electrons, ions, and dust grains interacting through long-range Coulomb forces. However, directly simulating all three species is computationally expensive due to the large disparity in masses and time scales.

It is generally observed that, compared to the massive dust grains, electrons and ions behave effectively as inertia-less species and primarily provide electrostatic shielding for dust–dust interactions. By treating electrons and ions as a neutralizing background, the dusty plasma can be reduced to a one-component system in which dust particles interact via a screened Yukawa potential,

$$U(r) = \frac{Q_d^2}{r} exp\left(-\frac{a_d}{\lambda_D}\right), \tag{1.27}$$

This simplification makes MD simulations feasible for realistic dust densities. Molecular dynamics techniques have been widely used to investigate dust acoustic waves, shock propagation, melting of plasma crystals, elastic properties, and transport coefficients such as viscosity in strongly coupled dusty plasmas treated as Yukawa systems[53–55] . Typically, these simulations involve a few thousand dust particles and are computationally efficient. Beyond small-scale simulations, MD methods have also been applied to study fluid instabilities and other collective phenomena in dusty plasmas modelled as Yukawa fluids [56,57].

1.9.3 Particle-in-Cell (PIC) Simulation Approach

In the particle-in-cell (PIC) method, the plasma is represented by a reduced number of computational particles, known as super-particles, each carrying proportionally larger charge and mass than real plasma particles while preserving the correct charge-to-mass ratio. This technique enables simulations of plasmas containing a large number of particles. In principle, PIC simulations can be used to model dusty plasmas by explicitly including electrons, ions, and dust grains. However, the characteristic time scales associated with these species differ significantly, ranging from the electron plasma period (f_{ep}^{-1}) to the much longer dust plasma period (f_{dp}^{-1}). Resolving all these time scales simultaneously requires substantial computational resources, making full PIC simulations of dusty plasmas impractical in many cases.

To overcome this limitation, hybrid PIC approaches are often adopted. In such models, electrons are treated as a negatively charged fluid, while ions and dust grains are modeled as discrete particles. This strategy allows for a more accurate description of ion and dust dynamics while keeping the computational cost manageable.

1.9.4 Generalized Hydrodynamic (GHD) Approach

The generalized hydrodynamic (GHD) approach [58] assumes that collective modes in dusty plasmas arise from continuum fluid behavior, while solid-like elastic effects emerge due to strong inter-particle correlations. These elastic properties are incorporated phenomenologically by coupling viscous fluid dynamics with elastic response, thereby treating the dusty plasma as a viscoelastic fluid.

In this framework, both fluid-like and solid-like characteristics are embedded into the governing equations through viscoelastic coefficients. The GHD model provides a unified description that bridges weakly and strongly coupled regimes and has proven particularly effective in explaining longitudinal and transverse wave propagation in strongly coupled dusty plasmas.

1.10 Waves and Instabilities in Strongly coupled dusty plasma

Dusty plasmas encountered in laboratory and space environments such as those associated with white dwarfs, supernovae, and plasmas generated through laser compression of matter generally contain dust grains in strongly coupled liquid or crystalline states, as discussed earlier. In contrast, weakly coupled and uncorrelated dusty plasmas arise when a substantial influx of energy is supplied to the dust subsystem, leading to an increase in dust temperature and a corresponding reduction in the strong correlation parameter Γ. Such heating may result from spatial or temporal variations in dust charge or from dust wave instabilities excited within the plasma [59]. As a consequence, the dispersion characteristics of strongly coupled dusty plasmas differ markedly from those of ideal weakly coupled systems.

Wave propagation in strongly correlated dusty plasmas has been investigated using several theoretical frameworks, including the quasi-localized charge approximation (QLCA) , the generalized hydrodynamic (GH) model , and multi-component kinetic theory. In addition, molecular dynamics (MD) simulation techniques have been utilised to examine dispersion properties over a wide range of the Coulomb coupling parameter Γ, spanning gaseous, strongly coupled liquid, and crystalline regimes [53,60]. The results from MD simulations show good agreement with predictions from these theoretical models.

The generalized hydrodynamic model provides a simple physical interpretation of viscoelastic effects arising from strong correlations among dust grains [58]. This phenomenological approach remains applicable across a broad range of coupling strengths $1 \le \Gamma \ll 200$, from weakly coupled gas-like states to strongly coupled liquid phases. The linearized GH equation for dust grains is expressed as

$$\left(1+\tau_m \frac{\partial}{\partial t}\right)\left[m_d n_{0d} \frac{\partial}{\partial t}\delta\vec{u_d}+\nabla\delta P+Z_d e n_{0d}\delta\vec{E}\right]=\eta\nabla.\nabla\delta u_d+\left(\xi+\frac{\eta}{3}\right)\nabla\left(\nabla.\vec{u_d}\right), \tag{1.28}$$

Where δu_d denotes the perturbed dust velocity, δP is the pressure, η and ζ are the shear and bulk viscosity coefficients, respectively, and τ_m represents the relaxation time. The compressibility and relaxation time of the dust fluid are given by Eqn. (1.29) and (1.30), respectively,

$$\mu_d = 1 + \frac{1}{3}u(\Gamma) + \frac{1}{9}\frac{\partial u(\Gamma)}{\partial \Gamma}, \tag{1.29}$$

and

$$\tau_m = \left(\xi + \frac{4}{3}\eta\right) \Big/ \left(n_{0d}T_d\left(1 - \gamma_d\mu_d + {}^{4u(\Gamma)}\!/_{15}\right)\right). \tag{1.30}$$

where the parameter $u(\Gamma)$ quantifies the excess internal energy. Within the appropriate coupling regime $1 \le \Gamma \le 200$, Slattery et al. [61] gave a relation for $u(\Gamma) = -0.89\Gamma + 0.95\Gamma^{1/4} + 0.19\Gamma^{-1/4} - 0.82$., while expressions for the transport coefficients were provided by Ichimaru et al. [62].

In the strongly correlated regime of dusty plasmas, two fundamental wave modes are commonly observed: (i) longitudinal modes and (ii) transverse (shear) modes. These modes can be analyzed in two limiting cases—the hydrodynamic regime $f\tau_m \ll 1$ and the strongly coupled regime $f\tau_m \gg 1$ each exhibiting distinct dispersion characteristics.

1.10.1 Longitudinal Waves

In longitudinal wave modes, the dust component provides the inertia, whereas electrons and ions contribute primarily through thermal effects. These low-frequency longitudinal modes resemble dust acoustic waves, but are modified by strong correlations among the dust grains. Using the generalized hydrodynamic (GH) model, Kaw and Sen [58] derived the dispersion relation in the hydrodynamic regime $f\tau_m \ll 1$ as

$$f\left(f + i\left(\nu_d + \eta^* k^2\right)\right) \simeq k^2\left[v_{td}^2\gamma_d\mu_d + \frac{C_d^2}{\left(1 + k^2\lambda_{eD}^2 + k^2\lambda_{iD}^2\right)}\right], \tag{1.31}$$

where ν_d denotes the dust-neutral collision frequency and $\eta^* = \dfrac{\left(\xi + \frac{4}{3}\eta\right)}{m_d n_{0d} f_{dp} a_d^2}$. Here a_d represents the average inter-grain spacing. In this regime, the longitudinal modes behave similarly to dust acoustic waves, with their phase velocity modified by the compressibility and shear viscosity of the strongly correlated dust medium. The phase velocity initially increases with the wave number k, but decreases at larger k values, as illustrated in Fig. 1.8. These modified dust acoustic waves experience viscous damping in addition to collisional damping, with the damping rate being proportional to the viscosity coefficient i.e. $\eta^* k^2$.

In the strongly coupled regime $f\tau_m \gg 1$, the dispersion relation takes the form

$$f\left(f+i\nu_d\right)\simeq k^2\left[v_{td}^2\gamma_d\mu_d+\frac{C_d^2}{\left(1+k^2\lambda_{eD}^2+k^2\lambda_{iD}^2\right)}+\frac{\eta^*}{\tau_m}\right]. \tag{1.32}$$

which again corresponds to a modified dust acoustic mode. Longitudinal waves in strongly coupled dusty plasmas are also susceptible to ion-dust streaming instabilities, which may account for discrepancies between theoretical predictions and experimental observations of dust acoustic -type longitudinal modes.

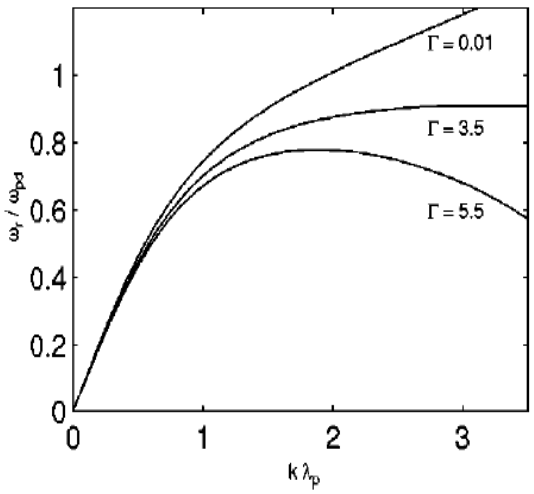

FIG. 1.8 Dispersion Characteristic of longitudinal for different values of Γ [58]

1.10.2 Transverse wave

According to the GH model, strong correlations among dust grains impart an effective rigidity to the dusty plasma, enabling it to support transverse, or shear, wave modes with nonzero frequency i.e. $\vec{k}\bullet\overrightarrow{\delta u_d}=0$, or $\vec{k}\times\overrightarrow{\delta u_d}\neq 0$. The dispersion relation for transverse modes is obtained by eliminating the longitudinal component from the GH momentum equation. Kaw and Sen [58] derived the corresponding dispersion relation as

$$f=-i\frac{\eta^*k^2}{\left(1-i\tau_m f\right)}, \tag{1.33}$$

In the hydrodynamic limit, this relation yields a purely damped mode $f=-i\eta^*k^2$, whereas in the strongly coupled regime it predicts a propagating elastic shear wave $f^2=\frac{\eta^*k^2}{\tau_m}$. Neutral collisions play a significant role in influencing the behavior of these transverse modes.

Experimental evidence for transverse shear waves in strongly coupled dusty plasma liquids has been reported by Pramanik et al. [63] and Kaw [64]. However, observing transverse modes in plasma crystals-commonly referred to as dust lattice waves-requires a different experimental approach. At high values of the coupling parameter Γ, it becomes necessary to incorporate the effects of the screening parameter κ, since viscoelastic coefficients depend on the degree of charge screening. Increasing the screening reduces the effective coupling strength. Nevertheless, results obtained using the one-component plasma (OCP) approximation within the GH framework remain reasonably valid for $\kappa \leq 1$ [65].

1.11 Instabilities in dusty plasma

Most laboratory and space dusty plasmas exist far from thermodynamic equilibrium. Such non-equilibrium conditions give rise to collective modes whose amplitudes may either grow exponentially or be damped due to collisional processes or collisionless mechanisms such as Landau damping and dust charge fluctuations. Dusty plasmas can become unstable when sources of free energy are present in the system. External field–driven flows, pressure gradients, dust charge variations, and propagating electron or ion beams can couple with the normal modes of the plasma and drive them unstable.

In addition to these mechanisms, classical hydrodynamic instabilities including Kelvin-Helmholtz, Rayleigh Taylor, and parametric instabilities also occur in dusty plasmas. These instabilities have attracted considerable interest because of their relevance to phenomena in Earth's ionosphere, the magnetopause, fluid dynamics, and the solar wind. Studying plasma instabilities is essential for understanding the mechanisms responsible for the growth or damping of wave amplitudes, as well as the formation of voids and other nonlinear structures observed in both space and laboratory plasmas [4].

The dispersion relation for such systems generally consists of two components: a real part and an imaginary part. In the weakly damped regime $\left|f_i\right| \ll f_r$, the wave frequency and instability growth rate can be determined from the real and imaginary parts of the dispersion relation, respectively, using the relations $\mathrm{Re}\ \varepsilon\left(f_r,k\right)=0$ and $f_i=-\dfrac{\mathrm{Im}\ \varepsilon\left(f,k\right)}{\partial\,\mathrm{Re}\ \varepsilon\left(f,k\right)}\Big|_{f=f_r}$ [66].

1.11.1 Current Driven Instability

A primary mechanism responsible for the instability of various electrostatic wave modes is the presence of an equilibrium drift of electrons relative to ions in the plasma [31],[67] , and [26]. This process, commonly referred to as a *current-driven instability*, is well established for both IAWs and EICWs. In such cases, the instability arises when resonant energy exchange between electrons and the wave overcomes collision less Landau damping.

In conventional electron–ion plasmas, Landau damping significantly suppresses the ion acoustic waves. However, the inclusion of negative charge on dust grains reduces both Landau damping and the associated spatial damping, thereby enhancing the growth rates of current-driven instabilities. Moreover, the presence of dust lowers the critical electron drift velocity required to trigger these instabilities and also diminishes ion cyclotron damping effects.

1.11.2 Ion–Dust Streaming Instability

In ion–dust streaming instability, dust-related wave modes couple with ion currents that are driven by externally applied static electric and magnetic fields. These ion–dust streaming instabilities associated with dust acoustic waves (DAWs) are analogous to the current-driven instabilities observed in dust ion–acoustic waves (DIAWs). Such instabilities have been experimentally observed in RF discharge plasmas [68] and have been investigated theoretically by Rosenberg [39], and others [69–71]. The presence of a streaming ion flux significantly alters the dispersion characteristics of DAWs.

1.11.3 Velocity Shear Instability

The Kelvin Helmholtz (KHI) instability is fundamentally a velocity-shear–driven instability that occurs in both neutral fluids and magnetized plasmas. In dusty (complex) plasmas, it plays an important role in explaining a variety of astrophysical phenomena, such as the stability of the interface between the solar wind and Earth's magnetosphere, interactions between adjacent solar wind streams with different flow velocities, and the dynamo generation of cosmic magnetic fields, where naturally occurring sheared dust flows are common. The hydromagnetic turbulence generated by the K–H instability serves as a significant source of anomalous viscosity and enhanced viscous drag in many space and astrophysical contexts. The velocity shear instability discussed here is the parallel velocity shear instability (PVSI), which arises in non-uniform magnetized plasmas. It is a fluid-type instability that occurs when ions flow along the direction of the applied magnetic field with a velocity that varies across the plasma, specifically in the direction perpendicular to the magnetic field where a density gradient exists. This instability is commonly identified as the Kelvin–Helmholtz instability (KHI) [72].

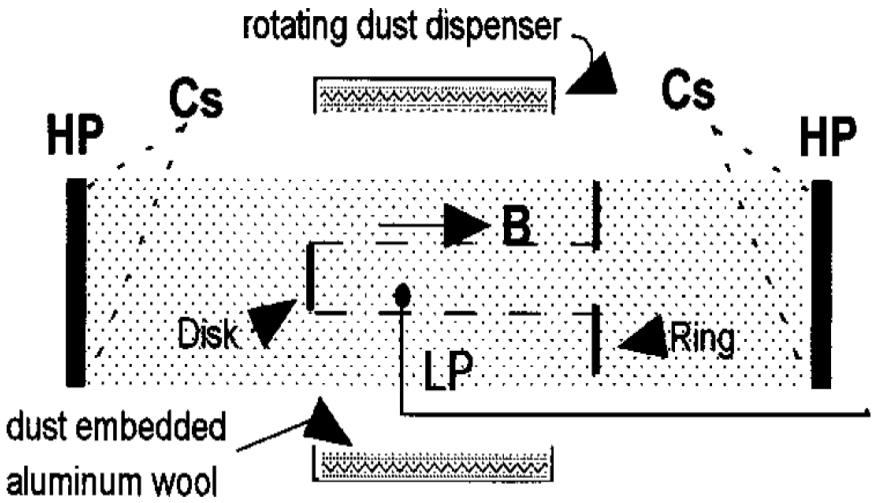

Fig. 1.9 Schematic diagram of the setup used in producing plasma having radial shear in with an ion flow parallel to magnetic field incorporating a drum capable of rotation for dispersing dust grains in to plasma [73]

PVSI was first observed by D'Angelo [74] in conventional electron–ion plasmas. The introduction of negatively charged dust grains modifies the growth rate of PVSI for low-frequency electrostatic waves [75] [73]. The instability growth rate increases with enhanced velocity shear in the ion flow, drawing energy from the mean ion drift. Experimentally, this

instability can be generated in dusty plasmas using a disk-and-ring electrode configuration [73], as illustrated in Fig. 1.9.

1.11.4 Rayleigh Taylor Instability (RTI)

13

The Rayleigh Taylor instability (RTI) in classical hydrodynamics arises at the interface between two fluids when a heavier fluid of density ρ_h overlies a lighter fluid of density ρ_l ($\rho_h > \rho_l$) in the presence of gravitational acceleration [76,77]. This instability has attracted considerable attention in astrophysical plasma contexts, including Type Ia supernovae, white dwarfs, the interiors of massive planets, high-density matter, and compact stars [78–82]. It is also relevant to laboratory plasma configurations such as Z-pinches [83], dense plasma focus devices [84], and phenomena involving zonal flows and streamers [85]. In dense plasmas, the presence of a density gradient supported by a magnetic field against gravity can render the system unstable. The hydrodynamic RTI plays a crucial role in inertial confinement fusion (ICF), where it significantly affects target implosion dynamics . Numerous studies have examined the RTI in the context of ICF and have evaluated its growth rates under various conditions [86–88]. Astrophysical observations, such as those of the Crab Nebula, reveal filamentary structures attributed to RTI developing at the interface between the pulsar wind and the surrounding supernova ejecta [89]. More recently, Hillier [90] demonstrated that magnetic Rayleigh-Taylor instability plays a central role in many astrophysical systems. In addition, RTI instability has been extensively investigated in emerging research areas including laboratory and astrophysical dusty plasmas [56,91,92] as well as in degenerate quantum plasmas. Several physical factors-such as magnetic field strength, density gradients, thermal conductivity, and finite Larmor radius (FLR) effects are known to influence the growth rate of the RTI in perturbed plasma systems.

1.12 Objectives and Thesis Layout

The primary objective of the present research is to investigate wave phenomena and plasma instabilities in magnetized dusty plasmas, considering both weakly and strongly coupled regimes of dust–dust interactions. The work focuses on understanding how dust grain dynamics influence the dispersion characteristics, stability, and propagation of various electrostatic modes in plasmas containing either weakly or strongly coupled dust components.

To achieve these objectives, theoretical models have been developed to analyze the excitation mechanisms of waves and instabilities in dusty plasmas. Using these models, mode frequencies and growth rates have been systematically evaluated over a range of experimentally relevant parameters. The theoretical predictions are compared with available experimental observations, and their implications for laboratory, space, and astrophysical dusty plasma environments are discussed.

A significant portion of the analysis incorporates the effects of Strong coupling, Dust charge fluctuations recognizing the importance of dust dynamics in realistic plasma conditions. Furthermore, since most dusty plasma experiments are conducted in bounded systems, the influence of finite geometry and boundary effects and magnetic field on wave propagation and instability development is explicitly taken into account.

The present research work is guided by the following major objectives:

1. Modelling Current driven low frequency electrostatic waves in a magnetized strongly

coupled dusty plasma.

2. Ion beam driven RTI in strongly coupled magnetized dusty plasma.
3. Effect of dust polarisation on Ion beam driven KHI in strongly coupled magnetized dusty plasma.
4. Effect of counter streaming ion beams on transverse shear waves in a strongly coupled dusty plasma.
5. Quantum and polarization effects on Dust Acoustic wave (DAW) in a streaming complex plasma.

1.13 Thesis Layout

The entire research work is organized into five chapters, which are outlined as follows:

Chapter 1: It deals with the introduction part to dusty plasmas, their occurrence in space and laboratory, production and charging mechanism. Additionally, dynamics of dust grains and various models for the description of dust particle have been discussed. Furthermore, dispersion characteristics of various wave modes and effect of dust on various instability have been discussed.

Chapter 2: provides a detailed theoretical analysis of low-frequency electrostatic wave modes in a strongly coupled, collisional, magnetized dusty plasma confined within a cylindrical geometry. The analysis focuses on how dust–dust correlations, collisions, magnetic field effects, and plasma geometry collectively influence the dispersion and stability characteristics of these modes.

A generalized hydrodynamic (GHD) framework is used to incorporate viscoelastic effects arising from strong coupling among dust grains. The chapter highlights how strong coupling effects, collisions, and magnetic field strength alter the stability thresholds and propagation properties of low-frequency modes

Chapter 3: gives a theoretical investigation of the beam-driven RTI in a strongly coupled, magnetized dusty plasma. The analysis is carried out within the framework of the generalized hydrodynamic (GHD) model, which incorporates viscoelastic effects arising from strong inter-grain correlations. The study specifically addresses how ion beam injection modifies the stability of a stratified dusty plasma in the presence of gravity, magnetic field, and finite plasma inhomogeneity.

Overall, this chapter demonstrates that strong coupling and magnetic field effects play a crucial stabilizing role in beam-driven RTI, while beam parameters act as a dominant destabilizing mechanism. The findings are particularly relevant for understanding and controlling RTI in dust-contaminated fusion plasmas**,** laser-driven systems, and astrophysical dusty environments, where strong coupling and external driving sources coexist.

Chapter 4: investigates the beam-driven Kelvin–Helmholtz instability (KHI) in a magnetized dusty plasma, with particular emphasis on the role of dust polarization effects. The study is motivated by the presence of velocity shear and energetic particle beams in both laboratory and space plasmas, where dust grains can significantly modify plasma response through polarization forces arising from charge separation in nonuniform electric fields. A theoretical model is developed using a multi-fluid framework that includes electrons, ions, beam ions, and

dust grains. The effects of dust polarization are incorporated through the polarization force acting on the dust component, which arises due to spatial gradients in the plasma electric field and modifies the dust momentum balance. The plasma is assumed to be inhomogeneous with a velocity shear aligned along the magnetic field, providing the free energy source required for the excitation of Kelvin–Helmholtz modes. Linear perturbation analysis is employed to derive the dispersion relation for low-frequency electrostatic modes in the presence of ion beam flow and dust polarization.

This chapter demonstrates that dust polarization is a critical mechanism in controlling beam-driven shear instabilities in dusty plasmas. The findings are relevant to laboratory dusty plasma experiments, fusion edge plasmas contaminated by dust, and astrophysical environments such as cometary tails and planetary magnetospheres, where velocity shear, energetic particle streams, and dust coexist.

Chapter 5: This chapter presents a concise summary of the major outcomes of the present research. The key scientific contributions related to waves and instabilities in dusty plasmas are highlighted. The broader scientific and social impact of the findings is discussed. Possible directions for future research are also identified.

References

[1] Alfvén H 1970 Plasma physics, space research and the origin of the solar system.

[2] Jones B and Faraday M 2010 The Life and Letters of Faraday (Cambridge University Press).

[3] Crookes W 1879 On radiant matter J. Frankl. Inst. **108** 305–16.

[4] Shukla P K and Mamun A 2015 Introduction to dusty plasma physics (CRC press).

[5] Chen F F 1984 Introduction to plasma physics and controlled fusion vol 1 (Springer).

[6] Ichimaru S 1982 Strongly coupled plasmas: high-density classical plasmas and degenerate electron liquids Rev. Mod. Phys. **54** 1017.

[7] Thomas Jr E, Konopka U, Artis D, Lynch B, Leblanc S, Adams S, Merlino R and Rosenberg M 2015 The magnetized dusty plasma experiment (MDPX) J. Plasma Phys. **81** 345810206.

[8] Hamaguchi S, Farouki R and Dubin D 1997 Triple point of Yukawa systems Phys. Rev. E **56** 4671.

[9] Smith B A, Soderblom L, Beebe R, Boyce J, Briggs G, Bunker A, Collins S A, Hansen C J, Johnson T V and Mitchell J L 1981 Encounter with Saturn: Voyager 1 imaging science results Science **212** 163–91.

[10] Smith B A, Soderblom L, Batson R, Bridges P, Inge J, Masursky H, Shoemaker E, Beebe R, Boyce J and Briggs G 1982 A new look at the Saturn system: The Voyager 2 images Science **215** 504–37.

[11] Cho J Y and Kelley M C 1993 Polar mesosphere summer radar echoes: Observations and current theories Rev. Geophys. **31** 243–65.

[12] Havnes O, Trøim J, Blix T, Mortensen W, Næsheim L, Thrane E and Tønnesen T 1996 First detection of charged dust particles in the Earth's mesosphere J. Geophys. Res. Space Phys. **101** 10839–47.

[13] Backhouse T 1885 The luminous cirrus cloud of June and July Meteorol Mag **20** 133–133.

[14] Thomas G E 1991 Mesospheric clouds and the physics of the mesopause region Rev. Geophys. **29** 553–75.

[15] Bernhardt P, Ganguli G, Kelley M and Swartz W 1995 Enhanced radar backscatter from space shuttle exhaust in the ionosphere J. Geophys. Res. Space Phys. **100** 23811–8.

[16] Garscadden A, Ganguly B, Haaland P and Williams J 1994 Overview of growth and behaviour of clusters and particles in plasmas Plasma Sources Sci. Technol. **3** 239.

[17] Tsytovich V N 1997 Dust plasma crystals, drops, and clouds Phys.-Uspekhi **40** 53.

[18] Winter J 1998 Dust in fusion devices-experimental evidence, possible sources and consequences Plasma Phys. Control. Fusion **40** 1201.

[19] Winter J 2000 Dust: A new challenge in nuclear fusion research? Phys. Plasmas **7** 3862–6.

[20] Boufendi L and Bouchoule A 1994 Particle nucleation and growth in a low-pressure argon-silane discharge Plasma Sources Sci. Technol. **3** 262.

[21] Xu W, Song B, Merlino R L and D'Angelo N 1992 A dusty plasma device for producing extended, steady state, magnetized, dusty plasma columns Rev. Sci. Instrum. **63** 5266–9.

[22] Merlino R L 2006 Dusty plasmas and applications in space and industry Plasma Phys. Appl. **81** 73–110.

[23] Chu J H and I L 1994 Direct observation of Coulomb crystals and liquids in strongly coupled rf dusty plasmas Phys. Rev. Lett. **72** 4009–12.

[24] Merlino R L and Goree J A 2004 Dusty plasmas in the laboratory, industry, and space Phys. Today **57** 32–8.

[25] Fortov V E, Nefedov A P, Torchinsky V M, Molotkov V I, Petrov O F, Samarian A A, Lipaev A M and Khrapak A G 1997 Crystalline structures of strongly coupled dusty plasmas in dc glow discharge strata Phys. Lett. A **229** 317–22.

[26] Thompson C, Barkan A, D'angelo N and Merlino R 1997 Dust acoustic waves in a direct current glow discharge Phys. Plasmas **4** 2331–5.

[27] Rao N, Shukla P and Yu M Y 1990 Dust-acoustic waves in dusty plasmas Planet. Space Sci. **38** 543–6.

[28] Walch B, Horányi M and Robertson S 1995 Charging of dust grains in plasma with energetic electrons Phys. Rev. Lett. **75** 838.

[29] Nakamura Y and Bailung H 1999 A dusty double plasma device Rev. Sci. Instrum. **70** 2345–8.

[30] d'Angelo N 1990 Low-frequency electrostatic waves in dusty plasmas Planet. Space Sci. **38** 1143–6.

[31] Merlino R L, Barkan A, Thompson C and D'Angelo N 1998 Laboratory studies of waves and instabilities in dusty plasmas Phys. Plasmas **5** 1607–14.

[32] Hirt M, Block D and Piel A 2004 Measurement of the ion drag force on free falling microspheres in a plasma Phys. Plasmas **11** 5690–6.

[33] Spitzer Jr L 2008 Physical processes in the interstellar medium (John Wiley & Sons).

[34] Barkan A, D'Angelo N and Merlino R L 1994 Charging of Dust Grains in a Plasma Phys. Rev. Lett. **73** 3093–6.

[35] Whipple E C, Northrop T G and Mendis D A 1985 The electrostatics of a dusty plasma J. Geophys. Res. Space Phys. **90** 7405–13.

[36] Jana M R, Sen A and Kaw P K 1993 Collective effects due to charge-fluctuation dynamics in a dusty plasma Phys. Rev. E **48** 3930–3.

[37] Barnes M S, Keller J H, Forster J C, O'Neill J A and Coultas D K 1992 Transport of dust particles in glow-discharge plasmas Phys. Rev. Lett. **68** 313–6.

[38] Chow V W, Mendis D A and Rosenberg M 1993 Role of grain size and particle velocity distribution in secondary electron emission in space plasmas J. Geophys. Res. Space Phys. **98** 19065–76.

[39] Rosenberg M 1996 Ion-dust streaming instability in processing plasmas J. Vac. Sci. Technol. Vac. Surf. Films **14** 631–3.

[40] Havnes O, Goertz C K, Morfill G E, Grün E and Ip W 1987 Dust charges, cloud potential, and instabilities in a dust cloud embedded in a plasma J. Geophys. Res. Space Phys. **92** 2281–7.

[41] Nitter T 1996 Levitation of dust in rf and dc glow discharges Plasma Sources Sci. Technol. **5** 93.

[42] Boeuf J and Punset C 1999 Physics and modelling of dusty plasmas Bouchoule John Wiley Sons.

[43] Northrop T and Birmingham T 1990 Plasma drag on a dust grain due to Coulomb collisions Planet. Space Sci. **38** 319–26.

[44] Perrin J, Molinas-Mata P and Belenguer P 1994 Ion drag and plasma-induced thermophoresis on particles in radiofrequency glow discharges J. Phys. Appl. Phys. **27** 2499.

[45] Talbot L, Cheng R K, Schefer R W and Willis D R 1980 Thermophoresis of particles in a heated boundary layer J. Fluid Mech. **101** 737–58.

[46] Daugherty J and Graves D 1995 Derivation and experimental verification of a particulate transport model for a glow discharge J. Appl. Phys. **78** 2279–87.

[47] Hamaguchi S and Farouki R T 1994 Polarization force on a charged particulate in a nonuniform plasma Phys. Rev. E **49** 4430–41.

[48] Khrapak S A, Ivlev A V, Yaroshenko V V and Morfill G E 2009 Influence of a Polarization Force on Dust Acoustic Waves Phys. Rev. Lett. **102** 245004.

[49] Ashrafi K S, Mamun A A and Shukla P K 2014 Polarization force for different dusty plasma situations J. Plasma Phys. **80** 1–7.

[50] Kalman G, Golden K, Donkó Z and Hartmann P 2005 The quasilocalized charge approximation Journal of Physics: Conference Series vol 11 (IOP Publishing) p 254.

[51] Golden K I and Kalman G J 2000 Quasilocalized charge approximation in strongly coupled plasma physics Phys. Plasmas **7** 14–32.

[52] Rosenberg M and Kalman G 1997 Dust acoustic waves in strongly coupled dusty plasmas Phys. Rev. E **56** 7166–73.

[53] Ohta H and Hamaguchi S 2000 Wave Dispersion Relations in Yukawa Fluids Phys. Rev. Lett. **84** 6026–9.

[54] Samsonov D, Goree J, Thomas H and Morfill G 2000 Mach cone shocks in a two-dimensional Yukawa solid using a complex plasma Phys. Rev. E **61** 5557.

[55] Liu B and Goree J 2005 Shear viscosity of two-dimensional Yukawa systems in the liquid state Phys. Rev. Lett. **94** 185002.

[56] Wani R, Mir A, Batool F and Tiwari S 2022 Rayleigh–Taylor instability in strongly coupled plasma Sci. Rep. **12** 11557.

[57] J. A and Ganesh R 2011 Coherent Vortices in Strongly Coupled Liquids Phys. Rev. Lett. **106** 135001.

[58] Kaw P K and Sen A 1998 Low frequency modes in strongly coupled dusty plasmas Phys. Plasmas **5** 3552–9.

[59] Fortov V E and Morfill G E 2009 Complex and Dusty Plasmas (CRC Press).

[60] Winske D, Murillo M S and Rosenberg M 1999 Numerical simulation of dust-acoustic waves Phys. Rev. E **59** 2263–72.

[61] Slattery W L, Doolen G D and DeWitt H E 1982 N dependence in the classical one-component plasma Monte Carlo calculations Phys. Rev. A **26** 2255–8.

[62] Ichimaru S, Iyetomi H and Tanaka S 1987 Statistical physics of dense plasmas: Thermodynamics, transport coefficients and dynamic correlations Phys. Rep. **149** 91–205.

[63] Pramanik J, Prasad G, Sen A and Kaw P K 2002 Experimental Observations of Transverse Shear Waves in Strongly Coupled Dusty Plasmas Phys. Rev. Lett. **88** 175001.

[64] Kaw P K 2001 Collective modes in a strongly coupled dusty plasma Phys. Plasmas **8** 1870–8.

[65] Farouki R T and Hamaguchi S 1994 Thermodynamics of strongly-coupled Yukawa systems near the one-component-plasma limit. II. Molecular dynamics simulations J. Chem. Phys. **101** 9885–93.

[66] Krall N A, Trivelpiece A W and Gross R A 1973 Principles of Plasma Physics Am. J. Phys. **41** 1380–1.

[67] Barkan A, D'Angelo N and Merlino R L 1996 Experiments on ion-acoustic waves in dusty plasmas Planet. Space Sci. **44** 239–42.

[68] Barkan A, Merlino R L and D'Angelo N 1995 Laboratory observation of the dust-acoustic wave mode Phys. Plasmas **2** 3563–5.

[69] Shukla P K and Mamun A A 2001 Low-frequency electrostatic waves in a bounded dusty magnetoplasma J. Plasma Phys. **65** 97–105.

[70] Kaw P and Singh R 1997 Collisional Instabilities in a Dusty Plasma with Recombination and Ion-Drift Effects Phys. Rev. Lett. **79** 423–6.

[71] Merlino R L 2009 Dust-acoustic waves driven by an ion-dust streaming instability in laboratory discharge dusty plasma experiments Phys. Plasmas **16** 124501.

[72] Chandrasekhar S 1961 Hydrodynamic and hydromagnetic stability.

[73] Luo Q Z, D'Angelo N and Merlino R L 2001 The Kelvin–Helmholtz instability in a plasma with negatively charged dust Phys. Plasmas **8** 31–5.

[74] D'Angelo N 1965 Kelvin—Helmholtz Instability in a Fully Ionized Plasma in a Magnetic Field Phys. Fluids **8** 1748–50.

[75] D'Angelo N and Song B 1990 The Kelvin-Helmholtz instability in dusty plasmas Planet. Space Sci. **38** 1577–9.

[76] Rayleigh 1882 Investigation of the Character of the Equilibrium of an Incompressible Heavy Fluid of Variable Density Proc. Lond. Math. Soc. **s1-14** 170–7.

[77] Taylor G I 1950 The instability of liquid surfaces when accelerated in a direction perpendicular to their planes. I Proc. R. Soc. Lond. Ser. Math. Phys. Sci. **201** 192–6.

[78] Kuranz C C, Park H-S, Huntington C M, Miles A R, Remington B A, Plewa T, Trantham M R, Robey H F, Shvarts D, Shimony A, Raman K, MacLaren S, Wan W C, Doss F W, Kline J, Flippo K A, Malamud G, Handy T A, Prisbrey S, Krauland C M, Klein S R, Harding E C, Wallace R, Grosskopf M J, Marion D C, Kalantar D, Giraldez E and Drake R P 2018 How high energy fluxes may affect Rayleigh–Taylor instability growth in young supernova remnants Nat. Commun. **9** 1564.

[79] Wang C-Y 2011 Rayleigh-Taylor instabilities in Type Ia supernova remnants undergoing cosmic ray particle acceleration - low adiabatic index solutions: R-T instabilities in SNRs Ia undergoing CR Mon. Not. R. Astron. Soc. **415** 83–92.

[80] Blondin J M and Ellison D C 2001 Rayleigh-Taylor Instabilities in Young Supernova Remnants Undergoing Efficient Particle Acceleration Astrophys. J. **560** 244–53.

[81] Cabot W H and Cook A W 2006 Reynolds number effects on Rayleigh–Taylor instability with possible implications for type Ia supernovae Nat. Phys. **2** 562–8.

[82] Shapiro S L and Teukolsky S A 2024 Black Holes, White Dwarfs and Neutron Stars: The Physics of Compact Objects (Wiley).

[83] Matzen M K 1997 Z pinches as intense x-ray sources for high-energy density physics applications Phys. Plasmas **4** 1519–27.

[84] Haines M G 1983 Ion beam formation in an m = 0 unstable Z pinch Nucl. Instrum. Methods Phys. Res. **207** 179–85.

[85] Das A, Sen A, Mahajan S and Kaw P 2001 Zonal and streamer structures in magnetic-curvature-driven Rayleigh–Taylor instability Phys. Plasmas **8** 5104–12.

[86] Betti R, Goncharov V N, McCrory R L and Verdon C P 1998 Growth rates of the ablative Rayleigh–Taylor instability in inertial confinement fusion Phys. Plasmas **5** 1446–54.

[87] Freeman J R, Clauser M J and Thompson S L 1977 Rayleigh-Taylor instabilities in inertial-confinement fusion targets Nucl. Fusion **17** 223–30.

[88] Sanz J 1994 Self-consistent Analytical Model of the Rayleigh-Taylor Instability in Inertial Confinement Fusion Phys. Rev. Lett. **73** 2700–3.

[89] Jun B 1998 Interaction of a Pulsar Wind with the Expanding Supernova Remnant Astrophys. J. **499** 282–93.

[90] Hillier A S 2016 On the nature of the magnetic Rayleigh–Taylor instability in astrophysical plasma: the case of uniform magnetic field strength Mon. Not. R. Astron. Soc. **462** 2256–65.

[91] Pacha K, Heinrich J, Kim S-H and Merlino R 2012 Observation of the Taylor instability in a dusty plasma Phys. Plasmas **19.**

[92] Avinash K and Sen A 2015 Rayleigh-Taylor instability in dusty plasma experiment Phys. Plasmas **22.**

Chapter 2

Cylindrical Geometry Effects on Low Frequency Wave Modes In a Strongly Coupled Dusty Plasma

2.1 Introduction

Dust is an omnipresent component in various laboratory and space plasma situations like fusion devices, plasma processing of materials, comet tails, planetary rings, solar wind, the earth's ionosphere, etc.**[1–5]**. These particles are undesirable during semiconductor wafer manufacture and fusion reactor design **[6,7]** whereas dust agglomeration is an essential process in the evolution of protoplanetary disks, and in the formation of planetesimals and comets **[8]**.

The micrometre-sized dust particles tend to accumulate a high negative charge due to the high mobility of electrons. The variation of dust charge, mass and size affects the dust particle dynamics and hence, the collective behavior of plasma **[9–13]**.The vital characteristic of dusty plasma is its ability to have a strong correlation among dust grains. The dust grains are correlated via the screened Coulomb potential, which is a function of the Coulomb coupling parameter Γ. The Coulomb coupling parameter Γ quantifies the strength of correlation among the dust particles. It is given by the ratio of the electrostatic interaction energy to the dust thermal energy

$$\Gamma = \frac{Z_d^2 e^2}{r_d T_d} \exp\left(-r_d/\lambda_d\right),$$

where $Z_d e$ denotes the dust charge, e denotes the electron charge, r_d is the inter-grain spacing given by $= \left(\frac{4\pi n_{0d}}{3}\right)^{-1/3}$, and T_d is the dust temperature, in the energy units $\mathrm{T_d} = K_B T$, λ_d denotes Debye length which accounts for the screening of the interaction. For $\Gamma \ll 1$ i.e., when the thermal kinetic energy dominates the electrostatic potential energy, the dust grains are said to be weakly correlated (WC) and when the Coulomb potential energy exceeds the mean kinetic energy, the dust grains become strongly correlated. In the limit $1 \leq \Gamma \leq \Gamma_c$ ($\Gamma_c = 171 \pm 3$) given by the Monte Carlo simulations plasma behaves like a fluid and above this critical value, it exhibits Wigner crystallization**[14–18]**. This ability of strongly coupled complex plasma to co-exist in the fluid and crystalline state in the $1 \leq \Gamma \leq \Gamma_c$ regime gives rise to the viscoelastic modes.

Since the strong correlation dust particles act as a viscous fluid. This introduces new dispersive corrections in the longitudinal mode along with the possibility of a novel shear mode. Kaw and Sen **[19]** utilized the generalized hydrodynamic model (GHD) to study the existence of transverse shear waves in strongly coupled dusty plasma **[20]**. These waves were observed experimentally in the three-dimensional dusty plasma in a strong coupling regime by Pramanik et al.**[21]**.

Xie and Chen **[22]** studied the effect of a strong correlation between dust in the presence of a magnetic field and the absence of collisions and drifts of plasma particles. They found a compressional mode like an ion dust hybrid wave with a unique transverse mode similar to the

torsional vibration mode. Banerjee et al. **[23]** studied the dispersion characteristics of the strongly correlated magnetized laboratory dusty plasma in the absence of dust-neutral collisions using the GHD model. It has been studied how strong coupling affects current-driven wave modes in collisional magnetized complex plasma for an infinite geometry **[24]**.

As laboratory and fusion plasma devices exist in a confined geometry, the study of boundary effects on the dispersion characteristics of low-frequency modes is of marked importance. The boundary effect (or finite geometry effect) is significant when the mode wavelength is comparable to the size of the plasma. Additionally, finite Larmor radius effects are also important in the case of finite geometry problems **[25]** .It has been observed that the drifting plasma particles and the quantized radial wave vector tend to modify the wave mode's dispersion properties for a cylindrical plasma geometry **[26]**.

To observe the significance of boundary effects on strongly coupled plasma, we propose a theoretical model for analyzing the drift-driven electrostatic modes in a magnetized strongly correlated collisional dusty plasma cylinder. The effect of dust-dust collision has also been considered in the proposed model. In the proceeding section, the Generalized Hydrodynamic (GH) model has been applied in the long wavelength region (where dust dynamics is vital) to derive the dispersion relation for the compressional and transverse mode in the hydrodynamic limit. In section III, results and discussion are presented followed by the conclusion in section IV.

2.2 Theoretical Model

We have assumed a strongly correlated collisional dusty plasma confined in the cylindrical geometry consisting of electrons, ions and dust grains. The dust grain radius a is lesser compared to the inter-grain distance r_d, and the electron and ion Debye radii λ_e and λ_i. An axial magnetic field B_0 is considered for the magnetic confinement of the plasma cylinder. The unperturbed densities of species (electrons, ions, and dust grains) are given by n_{0e} n_{0i} and n_{0d} . The charge and mass of species are (Q_e, m_e) (Q_i, m_i) and (Q_d, m_d). v_{ed}, v_{id} and v_{dd} are the drift velocities of the species along the magnetic field. The neutral collisional frequencies of species are ν_e, ν_d, and ν_i. The electrostatic perturbation is given by $\sim e^{-i(ft-\boldsymbol{k.r})}$. The Generalized hydrodynamic momentum equation **[19]** for dust fluid in the limit $1 \leq \Gamma \leq \boldsymbol{\Gamma_c}$ is given as

$$\left(1+\tau_m\left(\frac{\partial}{\partial t}+u\cdot\nabla\right)\right)\left[\, m_d n_{0d}\frac{\partial}{\partial t}\delta\boldsymbol{u_d}+\nabla\delta P+Z_d e n_{0d}\delta\boldsymbol{E}+m_d n_{0d}\nu_d\delta\boldsymbol{u_d}+\frac{1}{c}Z_d e n_{0d}\delta\boldsymbol{u_d}\times\boldsymbol{B}_0\,\right]$$

$$=\eta\nabla\cdot\nabla\delta u_d+\left(\zeta+\frac{\eta}{3}\right)\nabla\left(\nabla\cdot\delta\boldsymbol{u_d}\right). \qquad (2.1)$$

Here δP is pressure, c is the velocity of light, u_d is the dust velocity, η and ζ are the viscoelastic coefficients and τ_m is the relaxation time for the dust particle.

The compressibility of dust (μ_d) **[27]** is given as

$$\mu_d=\frac{\left(\partial_n P_d\right)_T}{T_d}=1+\frac{1}{3}u(\Gamma)+\frac{1}{9}\frac{\partial u(\Gamma)}{\partial\Gamma}. \qquad (2.2)$$

The quantity u (Γ) gives the excess internal energy which is represented in the strongly correlated regime through the analytical expression given by Slattery et al. **[28]**.

$$u\left(\Gamma\right) = -0.89\Gamma + 0.95\Gamma^{1/4} + 0.19\Gamma^{-1/4} - 0.82 \quad for\, 1 \le \Gamma \le 200 \tag{2.3}$$

The dependence of viscoelastic coefficients η and ζ on Γ is given by the Monte Carlo simulations **[28,29]**

$$\eta' = \frac{\left(\zeta + \frac{4}{3}\eta\right)}{m_d n_{0d} f_{dp} r_d^2} \approx 0.02\,\Gamma^{1/2}, \tag{2.4}$$

and

$$\tau_m^* = f_{dp}\tau_m \approx 0.375\,\Gamma^{1/2}, \tag{2.5}$$

where

$$\tau_m = \left(\zeta + \frac{4}{3}\eta\right) \Big/ n_{0d} T_d \left(1 - \gamma_d \mu_d + 4u\left(\Gamma\right)/15\right). \tag{2.6}$$

Here, γ_d is the adiabaticity, and f_{dp} is the dust plasma frequency. The following subsection aims to obtain the dispersion relation for the low-frequency modes by applying the set of Generalized Hydrodynamic equations.

2.2.1 Dust Compressional Mode

The compressional low-frequency modes are perpendicular to the undisturbed magnetic field and parallel to the electrostatic perturbation and the wave vector. These modes are supported by the inertia of massive dust particles. The continuity equation for the dust fluid is given by

$$\frac{\partial}{\partial t}\delta n_d + \nabla \cdot \left(n_d \delta \boldsymbol{u_d}\right) = 0. \tag{2.7}$$

As these waves are accompanied by density fluctuations, the perturbed density of dust particles is found by implementing Eq. (2.2) and Eq. (2.7) into the dust equation of motion given by Eq. (2.1)

The perturbed density of dust particles is readily obtained as

$$\delta n_d = \frac{-Z_d e n_{0d} \nabla_\perp^2 \phi}{m_d \left(f - k_z \mathrm{v}_{dd}\right) A}, \tag{2.8}$$

where

$$A = \left[\frac{k^2 \gamma_d \mu_d \mathrm{v}_{dt}^2}{\left(f - k_z \mathrm{v}_{dd}\right)} - \left(f - k_z \mathrm{v}_{dd} + i\nu_d\right) + \frac{k^2\left(\zeta + \frac{4}{3}\eta\right)}{\left(1 - i\tau_m f\right) i m_d n_{0d}} + \frac{f_{dc}^2}{\left(\frac{i\eta k^2}{\left(1 - i\tau_m f\right) m_d n_{0d}} + \left(f - k_z \mathrm{v}_{dd} + i\nu_d\right)\right)}\right]. \tag{2.9}$$

Here, $\mathrm{v}_{dt} = \left(\sqrt{T_d / m_d}\right)$ and $f_{dc} = \left[-\left(Z_d e\right) B / m_d c\right]$ are the dust thermal velocity and the dust cyclotron frequency respectively. Further the viscoelastic coefficients η, ζ, and τ_m have been omitted, taking into consideration the fact that only the dust particles are in a strongly coupled state while the electrons and ions are in the weakly coupled state. On substituting $\gamma_d = \mu_d = 1$ for the low compressibility limit, and

$f << k_z \mathrm{v}_{ed}$, $\nu_e << k\mathrm{v}_{et}$ and $f^2 << f_{ic}^2 << f_{ec}^2$, $k_z \mathrm{v}_{dd} << f << k_z \mathrm{v}_{id}$, the subsequent equations have been obtained. The perturbed number densities of the ion and electrons may be obtained as

$$\delta n_r = \frac{\mp e n_{0k} \nabla_\perp^2 \phi}{m_j [k^2 \mathrm{v}_{rt}^2 + f_{rc}^2 - (f - k_z \mathrm{v}_{rd} + i\nu_r)(f - k_z \mathrm{v}_{rd})]}, \tag{2.10}$$

where $r = i$ or e, and $\mathrm{v}_{rt} = \left(\sqrt{\frac{T_r}{m_r}} \right)$ are the thermal velocities of species and $f_{rc} = \pm \left(\frac{eB_0}{m_r c} \right)$ are the cyclotron frequencies of species. Substituting the values of perturbed densities of species from Eq. (2.8) and Eq. (2.10) in Poisson's equation

$$\nabla^2 \phi = 4\pi (\delta n_e e + z_d e \delta n_d - e \delta n_i). \tag{2.11}$$

For axially and azimuthally symmetric case, Eq. (2.11) takes the form which is a Bessel's equation of order zero.

$$\frac{\partial^2 \phi}{\partial r^2} + \frac{1}{r} \frac{\partial \phi}{\partial r} + q^2 \phi = \frac{f_{dp}^2 k_\perp^2 \phi}{(f - k_z \mathrm{v}_{dd}) A}, \tag{2.12}$$

where

$$q^2 = -k_z^2 - L k_\perp^2 \phi \tag{2.13}$$

and

$$\mathrm{L} = \left[\frac{f_{ep}^2}{\left[k_\perp^2 \mathrm{v}_{et}^2 + f_{ec}^2 - (f - k_z \mathrm{v}_{ed} + i\nu_e)(f - k_z \mathrm{v}_{ed}) \right]} + \frac{f_{ip}^2}{\left[k_\perp^2 \mathrm{v}_{it}^2 + f_{ic}^2 - (f - k_z \mathrm{v}_{id} + i\nu_i)(f - k_z \mathrm{v}_{id}) \right]} \right]. \tag{2.14}$$

Here,

$$f_{rp} = \left(\frac{4\pi (Q_r)^2 n_{0r}}{m_r} \right)^{1/2} \tag{2.15}$$

is the characteristic plasma frequency of oscillation, when they are disturbed from the equilibrium position. Where (Q_r, n_{0r}, m_r) are the charge density, number density and mass of the plasma species. Here $r = d, i \text{ and } e$ corresponds to the dust particles, ions, and electrons respectively. In the absence of R.H.S. of the Eq. (2.12) ϕ is given by

$$\phi = U J_0(q_x r), \tag{2.16}$$

where U is a constant and $J_0(q_x r)$ is the Bessel function of order zero and argument $q_x r$. On the surface of the plasma waveguide, we should have $J_0(q_x r) = 0$ **[30]**. Here $q_x r = \delta_n$, where δ_n gives the zeroes of the Bessel's function. Some of which are given as $\delta_1 = 2.404$, $\delta_2 = 5.5$, $\delta_3 = 8.7$, $\delta_4 = 11.8$ **[31].** When the effect of dust dynamics is considered (i.e., R.H.S. of the Eq. (2.12) $\neq 0$), wave function ϕ can be given by a combination of orthogonal wave functions:

$$\phi = \sum_m A_m J_0(q_y r), \tag{2.17}$$

where the effective radial wave vector $q_x = 2.404 / r_0$ is quantized. Simplifying Bessel's equation for the dominant mode x = y, in the limit $f \ll k_z \mathrm{v}_{ed}$, $\nu_e \ll k_\perp^2 v_{et}^2 < f_{ec}^2$, the dispersion relation for the compressional mode is obtained as

$$1+\frac{1}{\Omega_e^2}+\frac{f_{ip}^2}{\left[\Omega_i^2 f_{ip}^2-iv_i\left(f-k_z \mathrm{v}_{id}\right)\right]}-\frac{f_{dp}^2 I}{\left(f-k_z \mathrm{v}_{dd}\right)A}=0, \tag{2.18}$$

where

$$I=\frac{\int_0^{r_0} rJ_0(q_x r)J_0(q_y r)dr}{\int_0^{r} rJ_0(q_x r)J_0(q_y r)dr},$$

$$\Omega_e^2=k_\perp^2\lambda_{eD}^2+V_{eA}^2, \qquad \text{and} \qquad \Omega_i^2=\left(k_\perp^2\lambda_{iD}^2+V_{iA}^2-k_z^2\mathrm{v}_{id}^2\Big/f_{ip}^2\right). \tag{2.19}$$

Here, $\lambda_{id}=\frac{\mathrm{v}_{it}}{f_{ip}}$, $\lambda_{ed}=\frac{\mathrm{v}_{et}}{f_{ep}}$, $V_{eA}=\frac{f_{ec}}{f_{ep}}$ and $V_{iA}=\frac{f_{ic}}{f_{ip}}$.

When the dust drift and magnetic field are neglected then Eq.(2.18) will yield the same dispersion relation for compressional mode as obtained by Kaw and Sen [Ref.**[19]** page 3556, Eq. (28)]. In the hydrodynamic limit $\left(f\tau_m<<1\right)$, Eq. (2.18) gives the dispersion relation for the compressional dust modes. Taking $f=f_r+i\gamma$ and $f_r\gg\gamma$ yields the real frequency as

$$f_r^c=k_z \mathrm{v}_{dd}+f_{dp}\left[\frac{P}{Q}I+q_m^2\lambda_d^2\gamma_d\mu_d+\left(-\frac{\eta_2^* q_m^2 r_d^2}{4}+\frac{v_d}{4f_{dp}}\right)^2+\frac{f_{dc}^2}{f_{dp}^2}\right]^{1/2}, \tag{2.20}$$

where

$P=f_{ip}^4\Omega_i^2(1+\Omega_i^2)+v_i(f-k_z \mathrm{v}_{id})^2$

and

$Q=\left[\left(1+\Omega_i^2\right)f_{ip}^2\right]^2+v_i^2(f-k_z v_{id})^2$.

The growth rate of the dust compressional mode is given as

$$\frac{\gamma^c}{f_{dp}}=\left[-\frac{v_d}{2f_{dp}}+\frac{n_2^* q_m^2 r_d^2}{2}\right]. \tag{2.21}$$

Equations (2.20) and (2.21) represent the frequency and growth rate of the compressional mode. In the absence of collision, Eq.(2.21) is similar to Xie and Chen [Ref.**[22]** page 3521 Eq.(18)].

2.2.2 Transverse Mode

The presence of the transverse mode is supported by the rigidity provided by the strong correlations among dust particles. Taking the curl on both sides of Eq. (2.1) to get the transverse component, we get

$$\left(f+iv_d+i\eta_1\right)\boldsymbol{k}\times\boldsymbol{u_d}+i\frac{Z_d e}{m_d}\left(\boldsymbol{k}\times\delta\boldsymbol{E}\right)+i\frac{Z_d e}{m_d c}\left(\boldsymbol{k}\cdot\boldsymbol{B}\right)\delta\boldsymbol{u_d}=0, \tag{2.22}$$

where $\eta_1=\frac{\eta k^2}{m_d n_{0d} f_{dp} r_d^2(1-i\tau_m f)}$.

Equation (2.22) could be used to derive the perturbed velocity of dust fluid transverse to **B**

$$\delta u_{d\perp}=\frac{Z_d e/m_d}{i[f_{dc}^2-(f+iv_d+i\eta_1)^2]}\times\left[(f+iv_d+i\eta_1)\delta\boldsymbol{E}+f_{dc}\frac{(\nabla\times\delta\boldsymbol{E}_z)}{k_z}\right]. \tag{2.23}$$

Using Eq. (2.23) in the dust fluid continuity equation, we get the perturbed density of plasma species as

$$\delta n_r = \frac{(f + i\eta_1 + i\nu_r) Q_r n_{0r} / m_r}{(f - k_z \mathrm{v}_{rd})[f_{rc}^2 - (f + i\eta_1 + i\nu_r)^2]} \nabla_\perp^2 \phi . \tag{2.24}$$

where r= d, e or i for dust, electron and ions respectively

The term η_1, in numerator and denominator can be ignored for obtaining the perturbed density of electrons and ions.

Using the perturbed densities in Poisson's equation and applying the axial and azimuthal symmetry for simplicity, we get Bessel's equation

$$\frac{\partial^2 \phi}{\partial r^2} + \frac{1}{r}\frac{\partial \phi}{\partial r} + N^2 \phi = -\frac{f_{dp}^2 k_\perp^2 \phi (f + i\eta_1' + i\nu_d)}{(f - k_z v_{dd})\left[(f + i\eta_1' + i\nu_d)^2 - f_{dc}^2\right]}, \tag{2.25}$$

where

$$N^2 = -k_z^2 + \frac{k_\perp^2 f_{ip}^2 (f + i\nu_i)}{(f - k_z \mathrm{v}_{id})\left[(f + i\nu_i)^2 - f_{ic}^2\right]} + \frac{k_\perp^2 f_{ep}^2 (f + i\nu_e)}{(f - k_z \mathrm{v}_{ed})\left[(f + i\nu_e)^2 - f_{ec}^2\right]} . \tag{2.26}$$

Now simplifying Eq. (2.25) as was done earlier, the solution of Bessel's equation to obtain the dispersion relation for the transverse shear mode, we get

$$1 - \frac{k_\perp^2}{k^2}\frac{f_{ip}^2 (f + i\nu_i)}{(f - k_z \mathrm{v}_{id})\left[(f + i\nu_i)^2 - f_{ic}^2\right]} - \frac{k_\perp^2}{k^2}\frac{f_{ep}^2 (f + i\nu_e)}{(f - k_z \mathrm{v}_{ed})\left[(f + i\nu_e)^2 - f_{ec}^2\right]}$$

$$= f_{dp}^2 \frac{k_\perp^2 I (f + i\eta_1 + \nu_d)}{k^2 (f - k_z \mathrm{v}_{dd})\left[(f + i\eta_1 + i\nu_d)^2 - f_{dc}^2\right]} . \tag{2.27}$$

Neglecting the effect of drift, collision, bounded geometry and magnetic field, the dispersion relation is similar to Kaw and Sen [Ref.**[19]**, page 3556, Eq. (22)]. If magnetized plasma is considered, then It matches well with [Ref.**[22]** page 3522, Eq. (33)]. Simplifying Eq. (2.27) in the hydrodynamic limit $(f\tau_m << 1)$ under the assumptions $\frac{k_\perp^2}{k^2} << 1,\ f_{ec}^2 + \nu_e^2 >> 1,\ \mathrm{v}_{ed} >> 1$, $f << f_{ic}, \nu_i$ & f_{ec}, ν_e and $f << \eta_1 << f_{dc}$,

We get,

$$(f - k_z \mathrm{v}_{dd})\left[f + i(\nu_d + \eta_1')\right] = f_{dp}^2 M , \tag{2.28}$$

where $M = \dfrac{k_\perp^2 I}{k^2\left[1 - i\dfrac{k_\perp^2 f_{ip}^2 \nu_i}{k^2 k_z \mathrm{v}_{id}(f_{ic}^2 + \nu_i^2)}\right]}$.

Equation (2.28) can be rewritten as $\varepsilon_r(f,k) + i\varepsilon_i(f,k) = 0$ for obtaining the frequency and the growth rate of the shear mode

$$\frac{f_r^t}{f_{dp}} = \frac{k_z \mathrm{v}_{dd}}{2 f_{dp}} \pm \sqrt{\frac{k_z \mathrm{v}_{dd}}{2 f_{dp}} + \eta^* \tau_m^* k^2 r_d^2 + M_r} \tag{2.29}$$

and

$$\gamma^t = -\frac{\nu_d}{2} + \frac{\nu_d k_z v_{dd}}{2 f_r} - \frac{\eta k^2}{2 m_d n_{0d}} + f_{dp}^2 M_i . \quad (2.30)$$

Here M_r and M_i are the real and imaginary parts of M.
Equations (2.29) and (2.30) represent the frequency and growth rate of the transverse mode. In the absence of dust drift and collision of ions and neutrals, the transverse mode is analogous to the dust-ion Alfven waves given by Xie and Chen **[22]**.

2.3 Results and Discussion

The effect of a finite geometry in the drift-driven magnetized strongly correlated Argon dusty plasma on the low-frequency modes has been analyzed in the hydrodynamic regime $\left(f\tau_m \ll 1\right)$. The slightly modified parameters have been used for the strongly correlated magnetized dusty plasma system **[32]**. The density of various species is given as $n_{0i} \approx 10^8 cm^{-3}$, $\frac{n_{d0}}{n_{0i}} = 5\times10^{-4}$ and $n_{0e} = 0.5 \times n_{0i}$ .The dust charge state is given by $Z_d \approx 10^3$, the electron temperature as $T_e \simeq 1.0\ eV$ and $T_i \sim T_d = 0.14\ eV$ are the ion and dust temperature respectively. $a = 5\times10^{-4}\ cm$ is the size (radius) of the dust grains, and their mass is 10^{12} times the proton mass m_p. An axial magnetic field B_0 = 4000 G is taken, $\nu_i \left(= 0.5 f_{ic}\right)$ and $\nu_d = \left(0.2 f_{dp}\right)$ are the collisional frequencies of ions and dust, respectively. The drift velocities of the ions and dust particles are $\mathrm{v}_{id} = 0.5 \times \mathrm{v}_{it}$ and $\mathrm{v}_{dd} = 1.0\ \mathrm{v}_{dt}$ respectively. The effective quantized radial wave vector $k_\perp \approx q_n = 2.404 / r_0 = 0.8\ cm$. The parameters taken in this study are in the range of strongly correlated dusty one-component plasma limit $\lambda_d > r_d \gg \lambda_{dd}$. Here r_d is the inter-grain spacing and λ_{dd} is the dust Debye length.
For the dust to be magnetised, small size of the dust particles should be complemented with the use of a high magnetic field. Moreover, the dust Larmor radius ρ_d $(= \mathrm{v}_{dt} / f_{dc})$ should be much smaller than the plasma tube diameter $2r_0$ and $f_{dc} \gg \nu_d$. This is because magnetizing the complex plasma is technically challenging **[32–34]** due to the low charge-to-mass ratio of dust particles. The cyclotron frequency ratio to the neutral momentum exchange frequency $(f_{rc} / \nu_{rn} \geq 1)$ should be greater than one, such that the particle performs full rotation (on average) of the Larmor orbit before collision **[35]**. To avoid Coulomb crystallization of dust grains, high dust temperature has been considered to retain the fluid characteristic of plasma.
We have employed MATLAB (version 2020a Natick, Massachusetts: The MathWorks Inc.) **[36]** for the solution of the equations and random values of the Coulomb coupling parameter have been considered in the $1 \leq \Gamma \leq \Gamma_C$ limit.

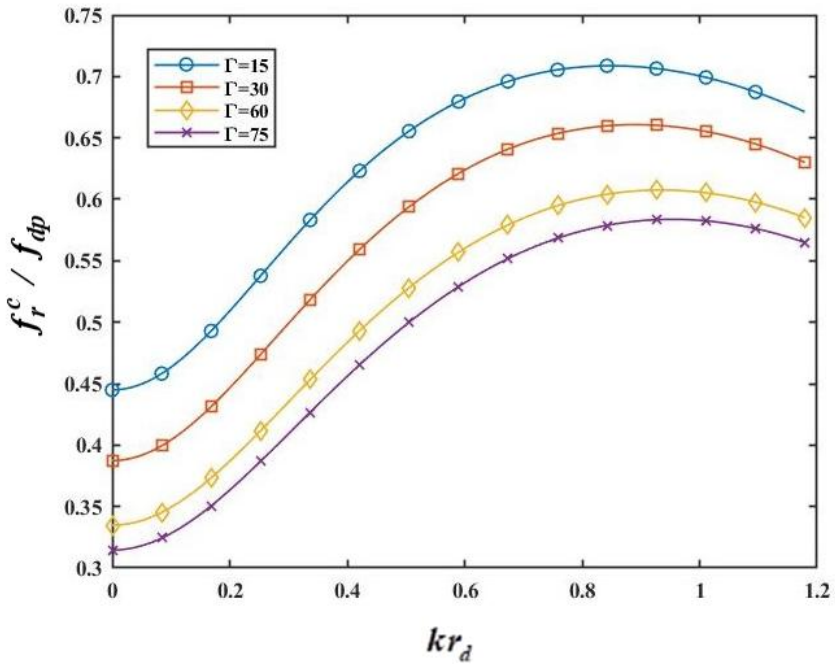

Fig. 2.1 Variation of Normalized real frequency (f_r^c / f_{dp}) of compressional mode with normalized wave vector (kr_d) for various coupling parameter Γ and for $v_d = 0.6 f_{dp}$, $v_i = 0.5 f_{ic}$, $v_{dd} = v_{dt}$, $v_{id} = 0.5 v_{it}$, k_z=2.0 cm^{-1} and B_0= 4000 G

The variation of normalized real frequency (f_r^c / f_{dp}) of compressional mode with normalized wave vector (kr_d) for various Coulomb coupling parameter Γ values has been shown In Fig. 2.1, It has been observed that in the long wavelength region ($kr_d \leq 1$) the mode frequency rises with an increase in wave vector but anomalous dispersion $\left(\frac{\partial f}{\partial k} < 0\right)$ is observed in the short wavelength region which has been confirmed experimentally **[37]**. It is in fair agreement with the previous studies of Xie and Chen **[22]** which show a decrement in mode frequency for the strong coupling parameter Γ, this may be because the viscosity of dust fluid is enhanced by strong correlation, which leads to dampening of the wave.

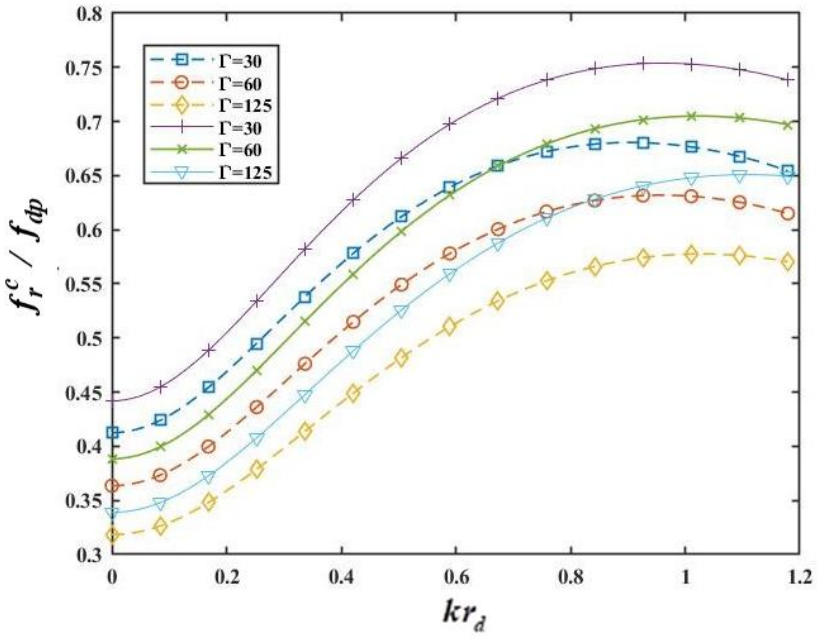

Fig. 2.2. Variation of Normalized real frequency (f_r^c / f_{dp}) of compressional modes with normalized wave vector (kr_d)(i) solid lines for infinite geometry with Γ= (a) 30, (b) 60, (c) 125 (ii) dashed lines for finite geometry with Γ= (a) 30, (b) 60, (c) 125, and for $v_d = 0.6 f_{dp}$, $v_i = 0.5 f_{ic}$, $v_{dd} = v_{dt}$ $v_{id} = 0.5 v_{it}$, $k_z = 2.0\ cm^{-1}$ and $B_0 = 4000$ G.

Fig. 2.2 depicts the variation of normalized mode frequency with normalized wave vector for different geometries and different values of the strong coupling parameter Γ=30, 60 and 125 which are below the Γ_c . It is clear from the figure that mode frequency for finite geometry is less than that of infinite geometry, for a particular value of coupling parameter. The reduction in mode frequency is more for the short wavelength region. The wave frequency is reduced nearly by 10 percent from that of infinite geometry in the long wavelength region ($kr_d < 1$). This may be due to the reduction in the interaction region for a finite geometry.

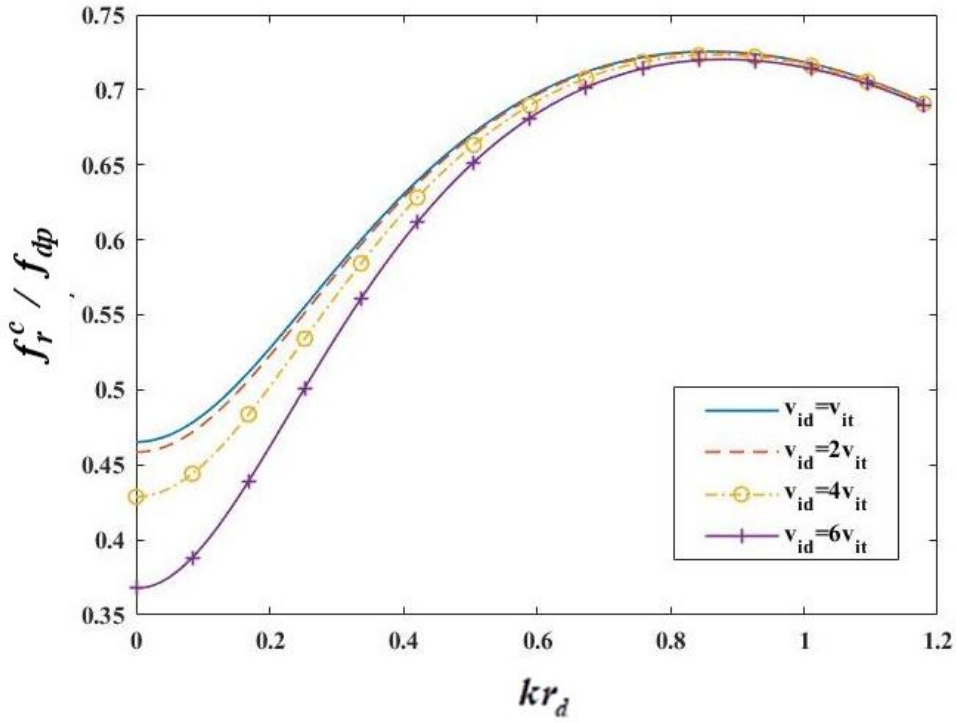

Fig. 2.3 Variation of Normalized real frequency (f_r^c / f_{dp}) of compressional modes with normalized wave vector (kr_d) for different ion drift speeds (i) $v_{id} = v_{it}$ (ii) $v_{id} = 2v_{it}$ (iii) $v_{id} = 4v_{it}$ (iv) $v_{id} = 6v_{it}$, and for $v_d = 0.6 f_{dp}$, $v_i = 0.5 f_{ic}$, $v_{dd} = v_{dt}$, $v_{id} = 0.5 v_{it}$, $k_z = 2.0\ cm^{-1}$ and B_0= 4000 G.

Fig. 2.3 depicts the variation of normalized mode frequency of compressional mode for different ion drift velocities with the normalized wave vector. It has been observed that the mode frequency decreases with the increase in the ion drift velocity in the long wavelength region ($kr_d \leq 1$). This is in line with the observation of Kaw and Singh **[38]** and for the short wavelength region, it is independent of the drift of the ions. This behavior agrees well with the experimental observation of Molotkov et. al. **[39]** where the increase in the drift motion of ions as compared to their thermal speed, suppresses the dust acoustic instability.

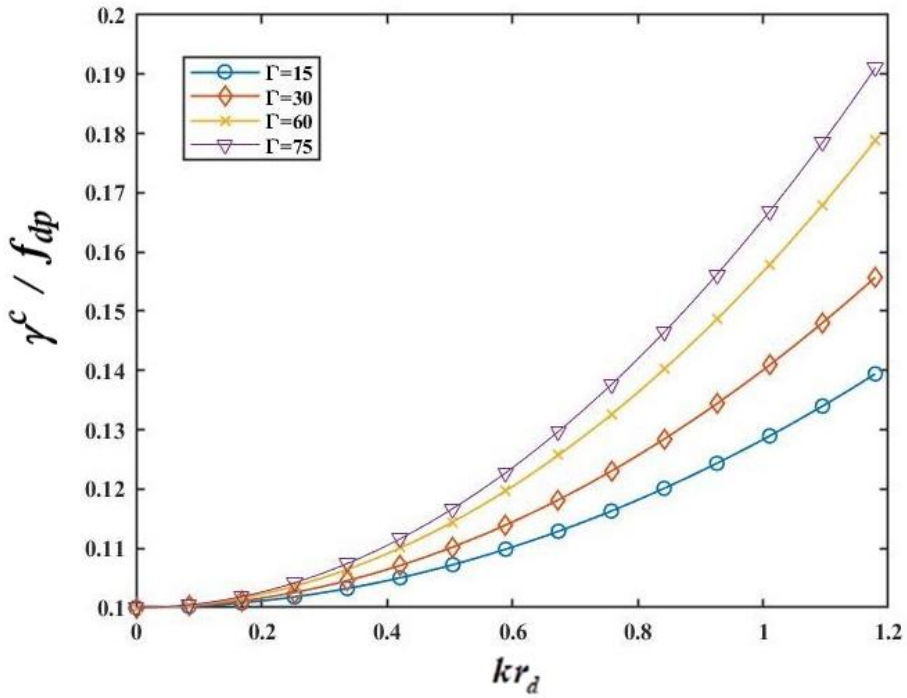

Fig. 2.4 The normalized growth rate (γ^c / f_{dp}) of compressional mode with normalized wave vector (kr_d) for various Coulomb coupling parameter (i) Γ=15 (ii) Γ=30 (iii) Γ=60 (iv) Γ=75 , and for $v_d = 0.6 f_{dp}$, $v_i = 0.5 f_{ic}$, $\mathrm{v}_{dd} = \mathrm{v}_{dt}$, $\mathrm{v}_{id} = 0.5\mathrm{v}_{it}$, $k_z = 2.0\ cm^{-1}$ and $\mathrm{B}_0 = 4000$ G.

Fig. 2.4 depicts the variation of the normalized growth rate (γ^c / f_{dp}) of compressional modes versus normalized wave vector for different values of Coulomb coupling parameter Γ. The growth rate rises with the increasing wave vector but diminishes with the increase in strong coupling parameter Γ. This may be associated with the enhanced viscosity of system, which on increase in strong correlation among dust provides inertia to the massive dust particles.

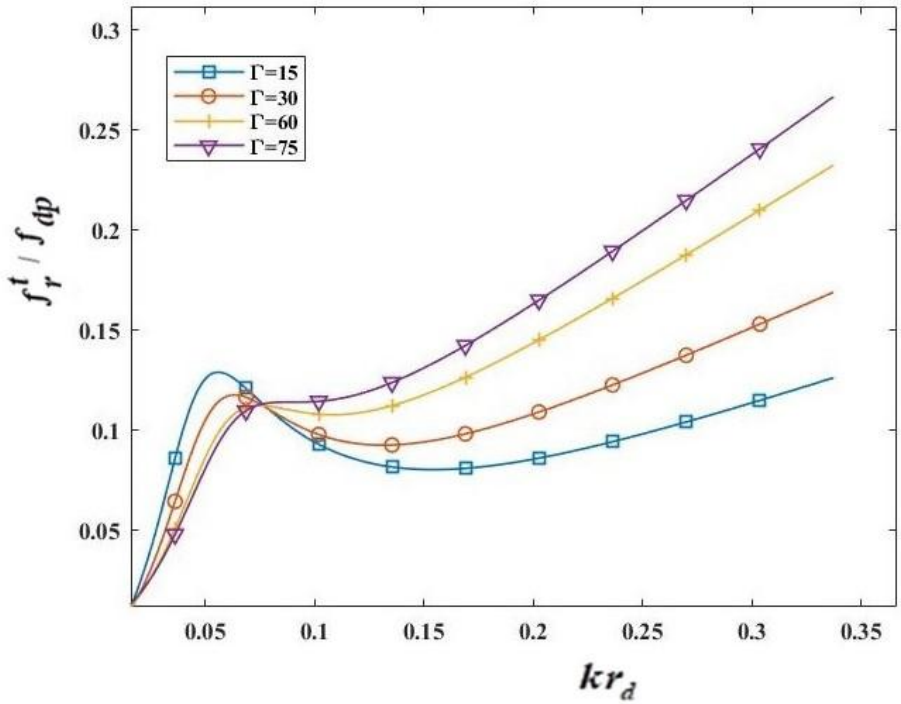

Fig. 2.5 The dependence of the normalized mode frequency $\left(f_r^t / f_{dp}\right)$ on the normalized wave vector (kr_d) of transverse mode for different values of Coulomb coupling parameter Γ (i)Γ=15 (ii) Γ=30 (iii) Γ=60 (iv) Γ=75, and for $v_d = 0.6 f_{dp}$ $v_i = 0.5 f_{ic}$, $v_{dd} = 0.5 v_{dt}$, $v_{id} = 0.5 v_{it}$, $k_\perp = 0.8\ cm^{-1}$, $k_z = 0 - 25\ cm^{-1}$ and B_0= 4000 G.

To analyze the transverse mode, we have shown the dependence of the normalized mode frequency $\left(f_r^t / f_{dp}\right)$ on the normalized wave vector (kr_d) for different values of strong coupling parameter Γ in Fig. 2.5 The mode frequency increases with increasing wave vector with increase in strong coupling parameter showing a slight decrement between k_z (0.05-0.1). This behaviour is similar to Dust modified Alfven modes **[40]** and well in agreement with the results of streaming and collisional instabilities in the absence of magnetic field and strong coupling **[41]** [refer page 4413 Fig. 3 and Fig.4]. This is in accordance with the fact that strong coupling supports the transverse shear mode by providing solid like rigidity and is well in agreement with the observations of Kharpak et. al. **[42]** .

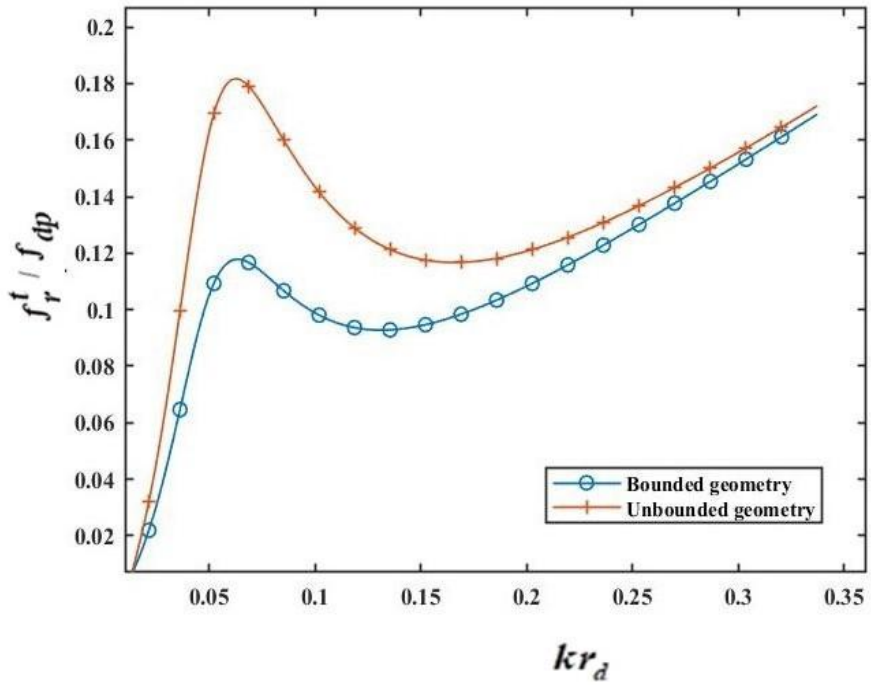

Fig. 2.6 The dependence of the normalized mode frequency $\left(f_r^t / f_{dp}\right)$ on the normalized wave vector(kr_d)of transverse mode for Coulomb coupling parameter Γ=30 (i) unbounded geometry(ii)bounded geometry, and $v_d = 0.6 f_{dp}$, $v_i = 0.5 f_{ic}$, $\mathrm{v}_{dd} = 0.5\ \mathrm{v}_{dt}$, $\mathrm{v}_{id} = 0.5\ \mathrm{v}_{it}$, $k_\perp = 0.8\ cm^{-1}$, $k_z = 0 - 25\ cm^{-1}$ and $\mathrm{B}_0 = 4000$ G.

It has been observed that the cylindrical geometry leads to an effective quantized wave number. The effect of different geometries on the mode frequency for the transverse mode in strong coupling regime has been studied (cf. Fig. 2.6). It is seen that the mode frequency is nearly halved in the case of finite geometry at $kr_d \simeq 0.05$ in the long wavelength region. This difference in frequency is significant in the long wavelength region up to k<0.1. The corresponding increment in mode frequency for bounded plasmas is less as compared to the infinite geometry in the long wavelength region.

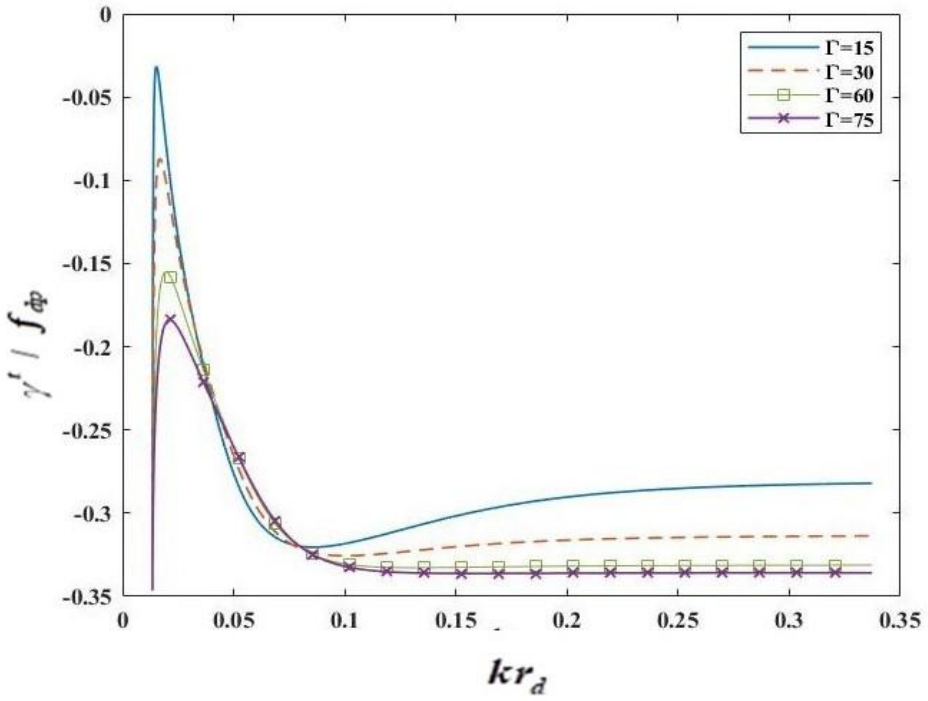

Fig. 2.7 Variation of normalized growth rate(γ^t / f_{dp}) of transverse mode with normalized wave vector (kr_d) for various values of Coulomb coupling parameter (i) Γ=15 (ii) Γ=30 (iii) Γ=60 (iv) Γ=75 and $v_d = 0.6 f_{dp}, v_i = 0.5 f_{ic}$, $v_{dd} = 0.5\ v_{dt}$, $v_{di} = 0.5\ v_{ti}$, $k_\perp = 0.8\ cm^{-1}$, $k_z = 0 - 20\ cm^{-1}$ and $B_0 = 4000$ G.

The normalized growth rate of transverse modes with normalized wavenumber for different values of Coulomb coupling parameter Γ has been plotted in Fig. 2.7 A negative growth rate has been observed which shows modes are purely damped. This result is well in agreement with the previous results **[19]** . However, the small positive growth rate may be observed for a weakly collisional regime for small values of strong coupling parameter Γ, this behaviour is similar to Alfven waves **[40]** . The growth rate shows a decrease with the increase in the Coulomb coupling parameter Γ as a result of viscous damping.

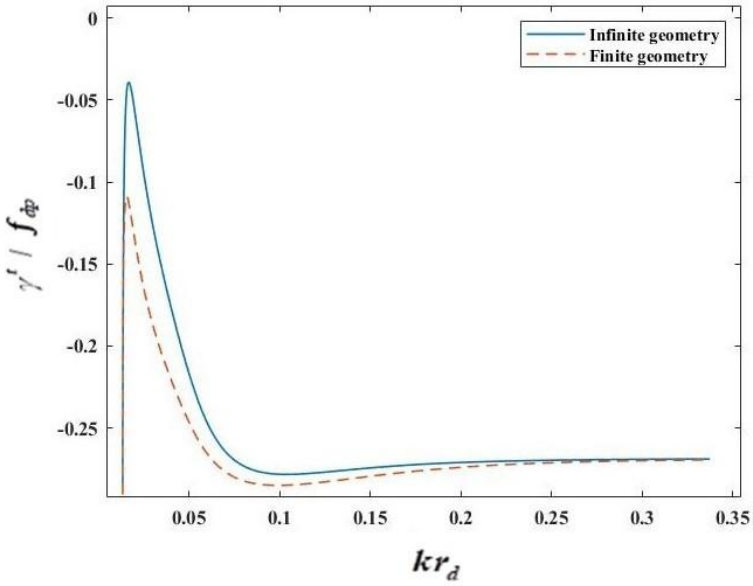

Fig. 2.8 Variation of normalized growth rate(γ^t / f_{dp}) of transverse mode for different plasma geometries with normalized wave vector (kr_d) for Γ=30 (i)for the infinite geometry(ii)for finite geometry and $v_d = 0.6 f_{dp}$, $v_i = 0.5 f_{ic}$, $v_{dd} = 0.5 v_{dt}$, $v_{di} = 0.5\ v_{it}$, $k_\perp = 0.8\ cm^{-1}$ $k_z = 2\ cm^{-1}$ and $B_0 = 4000$ G.

The comparison of normalized growth rate of transverse mode for finite and infinite cases, as a function of normalized wave vector is depicted in Fig. 2.8 The growth rate for the finite geometry is lesser than that of infinite geometry for a minuscule region in long wavelength regime (k<0.1) while it remains unaffected in short wavelength region. However, the mode is damped for both finite and infinite geometries.

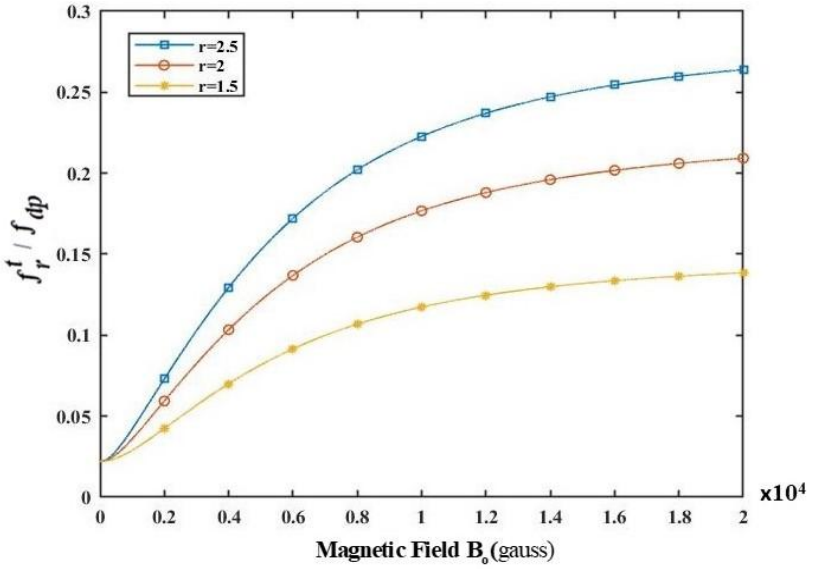

Fig.2.9 The normalized frequency of transverse mode vs magnetic field for different values of r, the radial distance from the axis of plasma cylinder for Coulomb coupling parameter Γ=30 (i)r = 2.5 (ii) r = 2 (iii)r =1.5, and for $k_z = 2\ cm^{-1}$ $v_d = 0.6 f_{dp}$, $v_i = 0.5 f_{ic}$, $v_{dd} = 0.5\ v_{dt}$, $v_{di} = 0.5 v_{it}$ and $k_\perp = 0.8\ cm^{-1}$

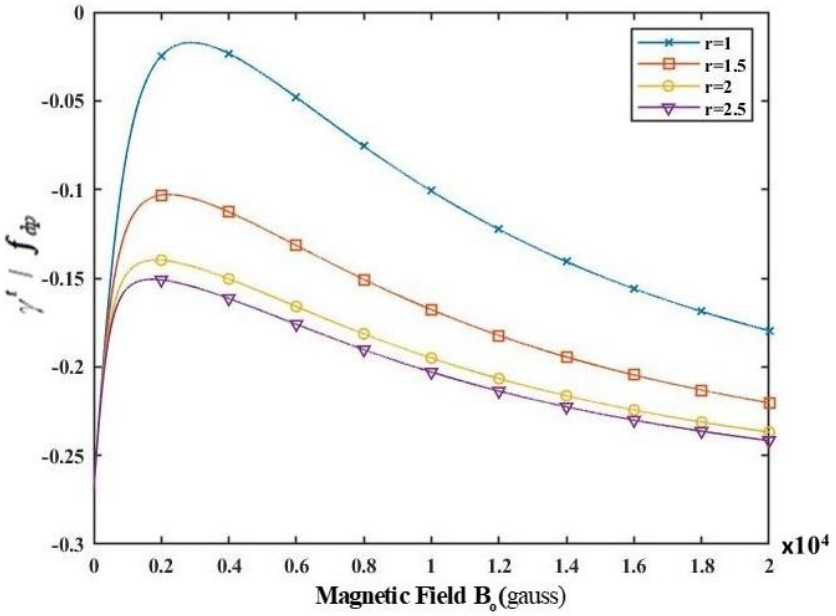

Fig. 2.10 The normalized growth rate of transverse mode vs magnetic field for different values of r, the radial distance from the axis of plasma cylinder for Coulomb coupling parameter Γ=30;(i) r=1, (ii) r=1.5, (iii) r=2, (iv) r=2.5, and for $k_z = 2\ cm^{-1}, v_d = 0.6 f_{dp}$, $v_i = 0.5 f_{ic}$ $v_{dd} = 0.5 v_{dt}$, $v_{id} = 0.5 v_{it}$ and $k_\perp = 0.8\ cm^{-1}$.

We have subsequently analyzed the effect of the magnetic field on the frequency (cf. Fig. 2.9) and growth rate (cf. Fig. 2.10) of transverse mode for different values of radial distance r and observed that in the long wavelength region, the mode frequency increases with increasing magnetic field. At a particular magnetic field strength mode frequency is more for the larger values of radial distance from the axis of plasma cylinder. The magnetic field provides tensile strength to the plasma fluid, making it more crystalline and hence giving solid-like elasticity for transverse mode propagation. The finite Larmor radius effect is significant when the wavelength of the wave is less than or comparable to the gyroradius (i.e., the ratio of electron gyroradius to perpendicular wavelength).
The growth rate increases with the magnetic field and stabilizes for the higher value of the magnetic field, this may be due to the fact that the low-frequency modes are difficult sustain at a very high magnetic field.

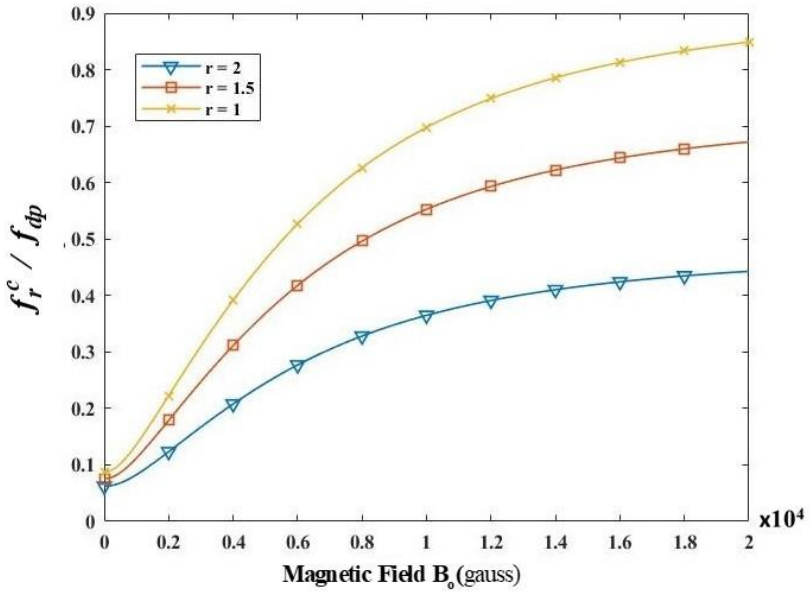

Fig. 2.11 The normalized frequency of compressional mode vs magnetic field for different values of r, the radial distance from the axis of plasma cylinder for Coulomb coupling parameter Γ=30 (i) r=1, (ii) r=1.5, (iii) r=2, and for $k_z = 2\ cm^{-1}, v_d = 0.6 f_{dp}$, $v_i = 0.5 f_{ic}$, $v_{dd} = 0.5 v_{dt}$, $v_{id} = 0.5 v_{it}$ and $k_\perp = 0.8\ cm^{-1}$.

It is also observed that the frequency of compressional mode also grows with increasing magnetic field strength. Moreover, as the radial distance from the axis of the plasma cylinder increases mode frequency shows decrement (cf. Fig.2.11). If the radius of confinement is doubled, the frequency nearly is reduced to half as magnetic field strength B_0 increases from 1 T to 4 T. It shows an increase in mode frequency with the increase in axial confinement of plasma which means that to observe the effect of magnetized dust on low frequency modes in the strongly coupled plasma, the plasma confinement radius should be small enough. At higher values of the magnetic field frequency saturates, which is in accordance with the experimental observation of the dust acoustic waves in magnetized plasma **[34,43]** . Moreover, the growth rate of compressional mode is found to be unaffected with the change in magnetic field in a strongly correlated collisional dusty plasma.

2.4 Conclusion

In this paper, we have analyzed the excitation of low frequency electrostatic modes in the hydrodynamic regime $(f\tau_m << 1)$ by virtue of the drift produced for ions and dust particles for a plasma cylinder. We have obtained a set of equations for the growth rate and frequency of modes which applies to the cylindrical geometry. It can be reiterated that the plasma geometry affects the dispersion characteristics of both the wave modes. Anomalous dispersion is observed for the compressional modes in the higher wavenumber limit. Transverse modes are purely damped modes whose behaviour is similar to dust-modified Alfven ion modes in a magnetized plasma cylinder **[22]**. It has been observed that the frequency of both modes enhances with an increase in magnetic field strength. The growth rate of low-frequency transverse modes is reduced by increasing the field strength while the growth rate of

compressional modes remains unaffected. These waves were found to be predominant in the low-collisional and long wavelength regions of the strongly coupled laboratory plasmas. In the operating regime of fusion devices these waves are insignificant and undesirable **[44]**. The study of strongly coupled dust grains in addition to the magnetic field is important in the case of the outer layer of neutron stars **[45]**.

Our model may find an application where the plasma is magnetically confined along the axis of plasma cylinder **[26,46–50]** . The model may be validated by studying the excitation of low frequency waves in magnetized dusty plasma having strongly correlated dust grains in the MDPX [32] provided that the plasma radius is small enough to have an optimum magnetic field strength below 0.2 T. In fusion devices, where a large magnetic field is required, the low frequency oscillations are nearly damped for all the magnetic field strengths provided the regime, $\left(f\tau_m << 1\right)$ is maintained during the plasma confinement.

References

[1] Pustylnik M Y, Pikalev A A, Zobnin A V, Semenov I L, Thomas H M and Petrov O F 2021 Physical aspects of dust–plasma interactions *Contrib. Plasma Phys.* 61 e202100126.

[2] Merlino R 2021 Dusty plasmas: from Saturn's rings to semiconductor processing devices *Adv. Phys. X* 6 1873859.

[3] Shukla P K and Mamun A A 2002 Introduction to Dusty Plasma Physics *Plasma Phys. Control. Fusion* 44 395–395.

[4] Melzer A, Goree J, Hippler R, Kersten H, Schmidt M and Schoenbach K 2008 Fundamentals of dusty plasmas *Low Temp. Plasmas* 1 129.

[5] Donnelly V M and Kornblit A 2013 Plasma etching: Yesterday, today, and tomorrow *J. Vac. Sci. Technol. Vac. Surf. Films* 31 050825.

[6] Winter J 2000 Dust: A new challenge in nuclear fusion research? *Phys. Plasmas* 7 3862–6.

[7] Rubel M, Widdowson A, Grzonka J, Fortuna-Zalesna E, Moon S, Petersson P, Ashikawa N, Asakura N, Hamaguchi D, Hatano Y, Isobe K, Masuzaki S, Kurotaki H, Oya Y, Oyaidzu M and Tokitani M 2018 Dust generation in tokamaks: Overview of beryllium and tungsten dust characterisation in JET with the ITER-like wall *Fusion Eng. Des.* 136 579–86.

[8] Blum J 2018 Dust Evolution in Protoplanetary Discs and the Formation of Planetesimals: What Have We Learned from Laboratory Experiments? *Space Sci. Rev.* 214 52.

[9] Islam M K, Nakashima Y, Yatsu K and Salimullah M 2003 On low-frequency dust-modes in a collisional and streaming dusty plasma with dust charge fluctuation *Phys. Plasmas* 10 591–5.

[10] Jana M R, Sen A and Kaw P K 1993 Collective effects due to charge-fluctuation dynamics in a dusty plasma *Phys. Rev. E* 48 3930–3.

[11] Rao N, Shukla P and Yu M Y 1990 Dust-acoustic waves in dusty plasmas *Planet. Space Sci.* 38 543–6.

[12] Rosenberg M 1993 Ion- and dust-acoustic instabilities in dusty plasmas *Planet. Space Sci.* 41 229–33.

[13] Rosenberg M 1996 Ion-dust streaming instability in processing plasmas *J. Vac. Sci. Technol. Vac. Surf. Films* 14 631–3.

[14] Chu J H, Du J-B and I L 1994 Coulomb solids and low-frequency fluctuations in RF dusty plasmas *J. Phys. Appl. Phys.* 27 296–300.

[15] Pieper J B, Goree J and Quinn R A 1996 Experimental studies of two-dimensional and three-dimensional structure in a crystallized dusty plasma *J. Vac. Sci. Technol. Vac. Surf. Films* 14 519–24.

[16] Nunomura S, Goree J, Hu S, Wang X and Bhattacharjee A 2002 Dispersion relations of longitudinal and transverse waves in two-dimensional screened Coulomb crystals *Phys. Rev. E* 65 066402.

[17] Ichimaru S 1982 Strongly coupled plasmas: high-density classical plasmas and degenerate electron liquids *Rev. Mod. Phys.* 54 1017–59.

[18] Chu J H and I L 1994 Direct observation of Coulomb crystals and liquids in strongly coupled rf dusty plasmas *Phys. Rev. Lett.* 72 4009–12.

[19] Kaw P K and Sen A 1998 Low frequency modes in strongly coupled dusty plasmas *Phys. Plasmas* 5 3552–9.

[20] Kaw P K 2001 Collective modes in a strongly coupled dusty plasma *Phys. Plasmas* 8 1870–8.

[21] Pramanik J, Prasad G, Sen A and Kaw P K 2002 Experimental Observations of Transverse Shear Waves in Strongly Coupled Dusty Plasmas *Phys. Rev. Lett.* 88 175001.

[22] Xie B-S and Chen Y-P 2004 Low frequency modes in strongly coupled magnetized dusty plasmas *Phys. Plasmas* 11 3519–24.
[23] Banerjee D, Mylavarapu J S and Chakrabarti N 2010 Viscoelastic modes in a strongly coupled, cold, magnetized dusty plasma *Phys. Plasmas* 17 113708.
[24] Segwal K R and Sharma S C 2019 A Nonlocal Theory of Current-Driven Low-Frequency Modes in a Magnetized Strongly Coupled Collisional Dusty Plasma *IEEE Trans. Plasma Sci.* 47 3087–99.
[25] Liu C S and Tripathi V K 1986 Parametric instabilities in a magnetized plasma *Phys. Rep.* 130 143–216.
[26] Tynan G R, Holland C, Yu J H, James A, Nishijima D, Shimada M and Taheri N 2006 Observation of turbulent-driven shear flow in a cylindrical laboratory plasma device *Plasma Phys. Control. Fusion* 48 S51–73.
[27] Ichimaru S, Iyetomi H and Tanaka S 1987 Statistical physics of dense plasmas: Thermodynamics, transport coefficients and dynamic correlations *Phys. Rep.* 149 91–205.
[28] Slattery W L, Doolen G D and DeWitt H E 1980 Improved equation of state for the classical one-component plasma *Phys. Rev. A* 21 2087–95.
[29] Slattery W L, Doolen G D and DeWitt H E 1982 N dependence in the classical one-component plasma Monte Carlo calculations *Phys. Rev. A* 26 2255–8.
[30] Sünder D 1986 Principles of Plasma Electrodynamics. By A. F. Alexandrov, L. S. Bogdankevich, A. A. Rukhadze. Springer-Verlag. Berlin, Heidelberg, New York, Tokio. 1984. Springer Series in Electrophysics, Volume 9; edited by G. Ecker (Ruhr-Universität Bochum) *Beitr. Aus Plasmaphys.* 26 142–142.
[31] Abramowitz M, Stegun I A and Romer R H 1988 *Handbook of Mathematical Functions with Formulas, Graphs, and Mathematical Tables Am. J. Phys.* 56 958–958.
[32] Thomas E, Konopka U, Artis D, Lynch B, Leblanc S, Adams S, Merlino R L and Rosenberg M 2015 The magnetized dusty plasma experiment (MDPX) *J. Plasma Phys.* 81 345810206.
[33] Thomas E, DuBois A M, Lynch B, Adams S, Fisher R, Artis D, LeBlanc S, Konopka U, Merlino R L and Rosenberg M 2014 Preliminary characteristics of magnetic field and plasma performance in the Magnetized Dusty Plasma Experiment (MDPX) *J. Plasma Phys.* 80 803–8.
[34] Choudhary M, Bergert R, Mitic S and Thoma M H 2020 Influence of external magnetic field on dust acoustic waves in a capacitive RF discharge *Contrib. Plasma Phys.* 60 e201900115.
[35] Piel A 2010 *Plasma Physics: An Introduction to Laboratory, Space, and Fusion Plasmas* (Berlin, Heidelberg: Springer Berlin Heidelberg).
[36] Shampine L F and Reichelt M W 1997 The MATLAB ODE Suite *SIAM J. Sci. Comput.* 18 1–22.
[37] Bandyopadhyay P, Prasad G, Sen A and Kaw P K 2007 Experimental observation of strong coupling effects on the dispersion of dust acoustic waves in a plasma *Phys. Lett. A* 368 491–4.
[38] Kaw P and Singh R 1997 Collisional Instabilities in a Dusty Plasma with Recombination and Ion-Drift Effects *Phys. Rev. Lett.* 79 423–6.
[39] Molotkov V, Nefedov A, Torchinskii V, Fortov V and Khrapak A 1999 Dust acoustic waves in a dc glow-discharge plasma *J. Exp. Theor. Phys.* 89 477–80.
[40] De Juli M C, Schneider R S, Ziebell L F and Jatenco-Pereira V 2005 Effects of dust-charge fluctuation on the damping of Alfvén waves in dusty plasmas *Phys. Plasmas* 12 052109.
[41] Mamun A A and Shukla P K 2000 Streaming instabilities in a collisional dusty plasma *Phys. Plasmas* 7 4412–7.

[42] Khrapak S A, Khrapak A G, Kryuchkov N P and Yurchenko S O 2019 Onset of transverse (shear) waves in strongly-coupled Yukawa fluids *J. Chem. Phys.* 150 104503.
[43] Thomas E, Konopka U, Merlino R L and Rosenberg M 2016 Initial measurements of two- and three-dimensional ordering, waves, and plasma filamentation in the Magnetized Dusty Plasma Experiment *Phys. Plasmas* 23 055701.
[44] Krasheninnikov S I, Smirnov R D and Rudakov D L 2011 Dust in magnetic fusion devices *Plasma Phys. Control. Fusion* 53 083001.
[45] Potekhin A Y 2010 The physics of neutron stars *Phys.-Uspekhi* 53 1235–56.
[46] Rapozo C 1987 RF heating by cylindrical plasma waveguide modes *Rev. Bras. Física* 17 1–14.
[47] Buzarbaruah N, Dutta N J, Borgohain D, Mohanty S R and Bailung H 2017 Study on discharge plasma in a cylindrical inertial electrostatic confinement fusion device *Phys. Lett. A* 381 2391–6.
[48] Amberg M, Geerk J, Keller M and Fischer A 2004 Design, characterisation and operation of an inverted cylindrical magnetron for metal deposition *Plasma Devices Oper.* 12 175–86.
[49] Badziak J, Pisarczyk T, Chodukowski T, Kasperczuk A, Parys P, Rosiński M, Wołowski J, Krousky E, Krasa J, Mašek K, Pfeifer M, Skala J, Ullschmied J, Velyhan A, Dhareshwar L J, Gupta N K, Rhee Y-J, Torrisi L and Pisarczyk P 2009 Formation of a supersonic laser-driven plasma jet in a cylindrical channel *Phys. Plasmas* 16 114506.
[50] Windisch T, Grulke O, Naulin V and Klinger T 2011 Intermittent transport events in a cylindrical plasma device: experiment and simulation *Plasma Phys. Control. Fusion* 53 085001.

Chapter 3

Rayleigh Taylor Instability in Strongly Coupled Magnetised Dusty Plasma Cylinder

3.1 Introduction

Rayleigh Taylor instability (RTI) grows at the interface when a denser fluid is accelerated into a lighter fluid in the presence of gravity **[1,2]**. RTI is a prominent instability in various astrophysical scenarios, white dwarfs, fusion research **[3–5]**, and laboratory dusty plasma situations in inertial confinement fusion (ICF), Tokomaks **[6]**, Laser accelerated plasmas **[7]** and supernova explosions **[8,9]**. Rayleigh-Taylor instability (RTI) with large variation in density dominates in high-speed systems such as supersonic aviation (ramjet engines) **[10]** and high energy systems like inertial confinement fusion devices **[11,12]** to harness energy from fusion. When the coulombic repulsion energy exceeds the dust thermal energy, the plasma goes in strong coupling regime, then the collective behaviour of dust fluid dominates, giving rise to modified phenomenon. For strong coupling regime, the Coulomb coupling parameter $\Gamma = \frac{Z_d^2 e^2}{r_d T_d} \exp\left(-r_d/\lambda_d\right) \gg 1$, where $Z_d e$ is the charge on dust grain, r_d is the inter-grain spacing given by $\left(\frac{4\pi n_{0d}}{3}\right)^{-1/3}$, T_d and λ_d are the dust temperature and dust Debye length, $\kappa = \left(r_d/\lambda_d\right)$ is the screening parameter which quantifies the Yukawa nature of the fluid. In the range $1 \leq \Gamma \leq \Gamma_c$, where $\Gamma_c = 171 \pm 3$ as determined by Monte Carlo simulations, plasma exhibits fluid-like behaviour. When Γ exceeds this critical value Γ_c, the system begins to undergo Coulomb crystallization **[13–15]**. Within this regime, the plasma's ability to exhibit characteristics of both fluid and solid phases leads to the emergence of viscoelastic modes.

Researchers have utilised the Generalised Hydrodynamic (GHD) Model to analyse the RTI in strongly coupled dusty plasma **[16,17]**.

In addition to the Generalized Hydrodynamic (GH) model employed in the present study, several other theoretical frameworks have been developed to describe strongly coupled and screened dusty plasmas. The Quasi-Localized Charge Approximation (QLCA) **[18]** provides a microscopic basis for describing collective excitations by explicitly accounting for particle correlations and localization effects. The thermodynamic approach **[19]** relates the compressibility and sound velocity to the equation of state of Yukawa fluids, thereby taking the screening effects. More recent works, including the nonlinear QLCA formulation **[20]**, the κ-dependent modulational instability model **[21]** and the Simple Fluid Approach (SFE) have demonstrated improved agreement with molecular dynamics simulations across a wide range of coupling and screening parameters.

The GHD model remains an important macroscopic description suitable for analysing large-scale hydrodynamic instabilities such as the Rayleigh–Taylor instability (RTI). However, in its conventional form, it treats the compressibility and viscoelastic coefficients as independent of

the screening parameter (κ), and therefore cannot fully capture the effects of strong screening or microstructural correlations emphasized in the above models.

4 The viscoelasticity of the strongly coupled medium, due to strong interparticle correlations, leads to a suppression of the Rayleigh Taylor Instability. This has significant implications for inertial confinement fusion experiments, where the higher dust densities can result in strongly coupled plasma conditions. The effect of magnetic field, radiation pressure, rotation and quantum effect have been studied by various researchers **[22–26]**. Rozina et al. **[22]**, investigated the effect of radiation on Rayleigh-Taylor instability in an adiabatic-radiative rare plasma and analysed that the radiative cooling and heating modify the growth rate of RTI. Magnetic field has shown a significant role in potentially damping the instability in magnetized plasmas **[27]**.

It is important to note that effects analogues to strong magnetic fields can also be produced in laboratory dusty plasmas through rotation. When the neutral gas or confinement electrode is set into rotation, the Coriolis force in place of Lorentz force acts on the charged dust grains. The transfer of angular momentum from rotating gas coloumn to the dust cloud is responsible for this effect. This has been experimentally demonstrated by Kählert et al. **[28]** and further investigated using the Quasi-Localized Charge Approximation (QLCA) by Kumar and Sharma **[20]**.

Radiation pressure, another key factor, can modify the growth rate and even introduce new instabilities **[29]**. The effects of rotation, particularly relevant in astrophysical contexts, also modify the behaviour of RTI **[30]**. Additionally, in dense plasmas, quantum effects can significantly alter the instability's dynamics **[25]** for instance, the interplay of viscosity and elasticity in cylindrical geometries has been investigated **[31]**, and the stabilization of RTI in quantum magnetized plasmas has also been examined **[32]**. MD simulation have been performed on the strongly coupled dusty plasma to analyse the effect of strong coupling on RTI **[33]**. In all, the radiation pressure, density and velocity affect the dispersion behaviour of RTI which plays a crucial role in fusion plasmas devices.

This manuscript focuses on beam-driven RTI within a strongly coupled dusty plasma having non-local effects. We investigated the combined influence of beam parameters, strong coupling, and magnetic field on the instability's growth rate in a non-local dusty plasma because of the confined nature of ICF devices. Understanding the interplay of these factors is crucial for applications like ICF, where controlling the stability of high-energy-density plasmas is paramount.

3.2 Theoretical Model

We have considered a strongly correlated inhomogeneous plasma with density gradient $\vec{\nabla} n \,||\, \hat{x}$, gravitational field $-g\hat{x}$ and a transverse magnetic field $B_0\hat{z}$ ions and dust are taken to be cold $T_i \approx T_d$.

The equilibrium state values of various parameters for the considered plasma system are given in Table 3.1 below.

Table 3.1. State Variables for different plasma species

	Density	Velocity	Temp.	Mass	Charge
Electron	n_{0e}	0	T_e	m_e	$-e$
Ion	n_{0i}	v_{0i}	T_i	m_i	$+e$
Beam	n_{0b}	$v_{0b}\hat{z}$	0	m_b	$+e$
Dust	n_{0d}	0	T_d	m_d	$Z_d e$

Initial drift velocity of electrons, ions and dust particles without the perturbation is obtained from the steady state equations solution for each species

No perturbation is applied upto this stage

The $\vec{g}\times\vec{B}_o$ drift for various species is given as

$$v_{0e}=\frac{m_e c}{-e}\frac{g(-\hat{x})\times B_o(\hat{z})}{B_o^2}=-\frac{g}{f_{ec}}\hat{y} \tag{3.1}$$

Here $\frac{eB_o}{m_e c}=f_{ec}$ is the cyclotron frequency of electron

Similarly, for dust particles and ions

$$v_{0d}=-\frac{g}{f_{dc}}\hat{y} \text{ and } \mathrm{v}_{0i}=+\frac{g}{f_{ic}}\hat{y}\ , \tag{3.2}$$

where f_{dc} and f_{ic} are the dust and ion cyclotron frequency.

Since the electrons and ions are moving in opposite direction, opposite charges accumulate on the perturbed boundary of plasma. Consequently. electric field is produced which gives rise to the $\bar{E}\times\bar{B}$ drift for electrons and ions being equal in magnitude but opposite in direction.

The steady state (equilibrium) equation for electron is given by

$$m_e\frac{dv}{dt}=-e\bar{E}-\frac{e\bar{v}\times\bar{B}_o}{c}-\frac{\nabla p}{n_o}=m_e g-\bar{v}\times\frac{e\bar{B}_o m_e}{m_e c}-\frac{\nabla p}{n_o}\ , \tag{3.3}$$

where $p=n_o T_e$ is the pressure term

$$\Rightarrow\frac{d\vec{v}}{dt}=-\vec{g}-\vec{v}\times\vec{f}_{ec}-\frac{\nabla p}{m_e n_o}$$

(here $f_{ec}=f_{ec}\hat{z}$ since magnetic field is in direction-z and $\vec{v}=v_{0x}\hat{x}+v_{0y}\hat{y}+v_{0z}\hat{z}$)

$$\Rightarrow 0 = -\vec{g} - v_{0y} f_{ec} \hat{x} + v_{0x} f_{ec} \hat{y} - \frac{T_e \nabla n_0}{m_e n_0}$$

$$\Rightarrow 0 = -g - v_{0y} f_{ec} - \frac{T_e}{m_e n_0} \frac{\partial n_0}{\partial x} \quad \text{(taking x component only)}$$

Since density gradient $\vec{\nabla} n \,||\, \hat{x}$

$n_0 = n_0 \left[1 + \frac{x}{L_n} \right]$, where L_n *is* the density scale length.

$$\Rightarrow \frac{\partial n}{\partial x} = \frac{n_0}{L_n} \Rightarrow \frac{1}{L_n} = \frac{1}{n_0} \frac{\partial n_0}{\partial x},$$

where $p = n_o T_e$ is the pressure

$$v_{oe} = -\frac{g}{f_{ec}} \hat{y} - \frac{v_{et}^2}{L_n f_{ec}} \hat{y} \quad . \tag{3.4}$$

The first term is ignored as the gravitational drift of electron is electron to ion mass ratio $\frac{m_e}{m_i}$ times smaller than that of ions, hence it is ignored. We get the dc drift velocity of electron as

$$v_{oe} = -\frac{v_{et}^2}{L_n f_{ec}} \hat{y} \, . \tag{3.5}$$

Similarly, for ions and dust the dc drift velocity is given as

$$v_{0i} = \left(\frac{g}{f_{ic}} + \frac{v_{it}^2}{L_n f_{ic}} \right) \hat{y} \, , v_{od} = \left(-\frac{g}{f_{dc}} - \frac{v_{dt}^2}{L_n f_{dc}} \right) \hat{y} \, . \tag{3.6}$$

Here $\mathrm{v}_{rt} = \left(\frac{T_r}{m_r} \right)^{1/2}$ are the thermal velocities of species, $L_n = \frac{1}{n_0} \frac{\partial n_0}{\partial x}$ is the density scale length, and $f_{rc} = \pm \left(\frac{Q_r B_0}{m_r c} \right)$ are the cyclotron frequencies of species, where Q_r is the charge on species and $r = e, i, d$ for electron ion and dust.

An electrostatic perturbation is applied in y-direction $\phi = \phi_o \exp\{-i(ft - k_y y)\}$, which gives rise to density and velocity perturbations

$$n_d = n_{0d} + n_{1d} \quad \text{and} \quad v_r = v_{0r} + v_{1d} \, . \tag{3.7}$$

Here n_{0d} and v_{0d} are the unperturbed number density and velocity of dust particles.

Equation of motion is solved by assuming the dust to be in strongly coupled state. The Generalised Hydrodynamic Model (GHD) **[34]** is a framework which incorporates both the fluid behaviour and the viscoelastic response arising due to the strong correlation among grains. The dust momentum equation is given by

$$\left(1+\tau_m\left(\frac{\partial}{\partial t}+u\cdot\nabla\right)\right)\left[\ m_d n_{0d}\frac{\partial}{\partial t}\delta\boldsymbol{u_d}+\nabla\delta P+m_d n_{0d}\boldsymbol{g}\ +Z_d e n_{0d}\delta\boldsymbol{E}+\frac{1}{c}Z_d e n_{0d}\delta\boldsymbol{u_d}\times\boldsymbol{B}_0\ \right] = \eta\nabla\cdot\nabla\delta\boldsymbol{u}_d+\left(\zeta+\frac{\eta}{3}\right)\nabla\left(\nabla\cdot\delta\boldsymbol{u}_d\right). \tag{3.8}$$

Here τ_m is the relaxation parameter, δP is pressure, u_d is the dust velocity, η and ζ are the viscoelastic coefficients,

The compressibility of dust fluid is given as **[35]**

$$\mu_d=\frac{\left(\partial_n P_d\right)_T}{T_d}=1+\frac{1}{3}u\left(\Gamma\right)+\frac{1}{9}\frac{\partial u\left(\Gamma\right)}{\partial\Gamma} \tag{3.9}$$

Here $u\left(\Gamma\right)$ is the excess internal energy given Slattery et. al. **[36]**

for $1\le\Gamma\le 120$ it is given by

$$u\left(\Gamma\right)=-0.89\Gamma+0.95\Gamma^{1/4}+0.19\Gamma^{-1/4}-0.82 \tag{3.10}$$

The variation of the viscoelastic coefficients η and ξ with Γ is given by the Monte Carlo simulations **[36,37]**

$$\eta'=\frac{\left(\zeta+\frac{4}{3}\eta\right)}{m_d n_{0d} f_{dp} r_d^2}\approx 0.02\,\Gamma^{1/2} \tag{3.11}$$

$$\tau_m^*=f_{dp}\tau_m\approx 0.375\,\Gamma^{1/2} \tag{3.12}$$

$$\tau_m=\left(\zeta+\frac{4}{3}\eta\right)\Big/ n_{0d}T_d\left(1-\gamma_d\mu_d+4u\left(\Gamma\right)/15\right) \tag{3.13}$$

Here γ_d is the adiabatic index, r_d is the interparticle distance among dust.

The equation of continuity for the dust fluid is given by

$$\frac{\partial}{\partial t}\delta n_d+\nabla\cdot\left(n_d\delta\boldsymbol{u_d}\right)=0 \tag{3.14}$$

The incompressibility condition is given by

$$\nabla.u=0 \tag{3.15}$$

The perturbed dust density is given by

$$n_{1d}=\frac{\mathrm{n}_{0d}Z_{de}\varphi}{m_d v_{td}^2 k L_n A}, \tag{3.16}$$

where $A=\left(\frac{1}{\left(f+\frac{kg}{f_{cd}}+\frac{kv_{td}^2}{L_n f_{cd}^2}-\frac{\eta k^2}{\left(1-i\tau_m f\right)}\right)}\right)$

Similarly for ions the term $\frac{kv_{ti}^2}{L_n f_{ci}^2}$ «1 and η→0 and $f_{cd}\to f_{ci}$, perturbed density will be

$$n_{1i} = -\frac{n_{0i} e\phi k^2}{m_i f_{ic}^2 M} \tag{3.17}$$

Here,

$$M = \frac{\frac{f_{ic}}{kL_n} + \left(f - \frac{kg}{f_{ic}}\right)}{\left(f - \frac{kg}{f_{ic}}\right)}$$

For electrons, mass is less gravitational term is ignored and using $f/f_{ci} \ll 1$ we get the perturbed electron density

$$n_{1e} = -\frac{n_{0e} e k^2 \varphi}{m_e f_{ce} k L_n f}. \tag{3.18}$$

The perturbed beam density is given by

$$n_{1b} = \frac{n_{0b} e k_z^2 \varphi}{m_b (f - k_z v_{0b})^2}. \tag{3.19}$$

Substituting the perturbed densities of various species into Poisson's equation

$$\nabla^2 \phi = 4\pi (n_{1e} e + z_d e n_{1d} - e n_{1i} - n_{1b} e), \tag{3.20}$$

we get

$$f_{rp}^2 = \frac{4\pi (Q_r e)^2 n_{0r}}{m_r},$$

where f_{rp} is the characteristic plasma frequency of oscillation for $r = d, i, b \text{ and } e$ corresponding to dust particles, ions, beam and electrons, respectively.

For the axial and azimuthal symmetry case, the equation takes the form of Bessel's equation

$$\frac{\partial^2 \phi}{\partial r^2} + \frac{1}{r}\frac{\partial \phi}{\partial r} + q^2 \phi = \frac{f_{bp}^2 k_\perp^2 \phi}{\left(f - k_z v_{0b}\right)^2}, \tag{3.21}$$

where $q^2 = -k_z^2 + \frac{f_{ep}^2 k^2}{f_{ec} k L_n f} - \frac{f_{dp}^2 f_{dc}}{v_{dt}^2 k L_n A} - \frac{f_{ip}^2 k^2}{f_{ic}^2 M}$.

In the absence of beam the R.H.S. of Eq. (3.21) vanishes and the wavefunction ϕ is given by

$$\phi = U J_0(q_x r) \tag{3.22}$$

here U is a constant and $J_0(q_x r)$ is zeroth-order Bessel function with argument $q_x r$, $J_0(q_x r) = 0$ on surface of waveguide **[38]**. Here $q_x r = \delta_n$, where δ_n gives the zeroes of the Bessel's function. Some of which are given as **[39]** $\delta_1 = 2.404, \delta_2 = 5.5, \delta_3 = 8.7, \delta_4 = 11.8$.

When influence of beam is considered (the R.H.S. of Eq. (3.21) is not zero) then ϕ is given as superposition of orthogonal wavefunctions

$$\phi = \sum_m A_m J_m(q_x r), \tag{3.23}$$

where the effective radial wave vector $q_x = 2.404/r_0$ is quantized. For the dominant mode x=y, Bessel's equation can be simplified due to the symmetry of the wave propagation.

Under assumptions $f >> \frac{kg}{f_{ic}}$ *and* $\frac{f_{ep}^2}{f_{ic}} \approx \frac{f_{ip}^2}{f_{ic}}$, in the hydrodynamic limit $(f\tau_m \ll 1)$, gives the dispersion relation for the compressional dust modes as

$$1+\frac{f_{dc}}{kL_n\left(f+\frac{kg}{f_{dc}}+\frac{kv_{td}}{L_n f_{dc}^2}-\frac{\eta k^2}{(1-i\tau_m f)}\right)}+\frac{f_{bp}^2 k_z^2 v_{td}^2 I}{f_{dp}^2 (f-k_z v_{0b})^2}=0\,. \tag{3.24}$$

Here $I=\frac{\int_0^{r_0} rJ_0(q_x r)J_0(q_y r)dr}{\int_0^{r} rJ_0(q_x r)J_0(q_y r)dr}$.

In the absence of beam, we get $f = k_z v_{0b}$ and $f=\eta k^2-\frac{kg}{f_{dc}}-\frac{f_{dc}}{kL_n}-\frac{kv_{dt}}{L_n f_{dc}^2}$. (3.25)

In the presence of beam, for small frequency mismatch, $f = f_r + i\gamma$ and in the limit $f_r \ll \gamma$, Eq. (3.24) yields the dispersion characteristics as real frequency f_r and growth rate γ of the instability as $\left(\varepsilon_r(f,k)\right)_{f=f_r}=0$ *and* $\gamma=-\left(\frac{\varepsilon_i(f,k)}{\frac{\partial\varepsilon_r(f,k)}{\partial f}}\right)_{f=f_r}$.

3.3 Results and Discussion

We have analyzed the effect of strong coupling parameter, beam velocity (energy), and density scale length L_n on RTI in strongly coupled dusty plasma cylinder. The slightly modified plasma parameters **[24,27,40]** have been utilised e.g., $m_e = 9.11\times10^{-31}kg$, $m_d = 10^{12}m_p = 10^{12}\times1836\,m_e$, $m_b = 6.49\times10^{-26}kg$, $n_{0e} = n_{0i} \approx 10^{12}cm^{-3}$ $n_{0b} \sim 10^{7}cm^{-3}$. We have used MATLAB (version 2020a, Natick, Massachusetts: The MathWorks Inc.) **[41]** to solve the equations, considering random values of the Coulomb coupling parameter within the range $1\leq \Gamma \leq \Gamma_c$, here Γ_c is the critical strong coupling parameter below which the dust is in the fluid state.

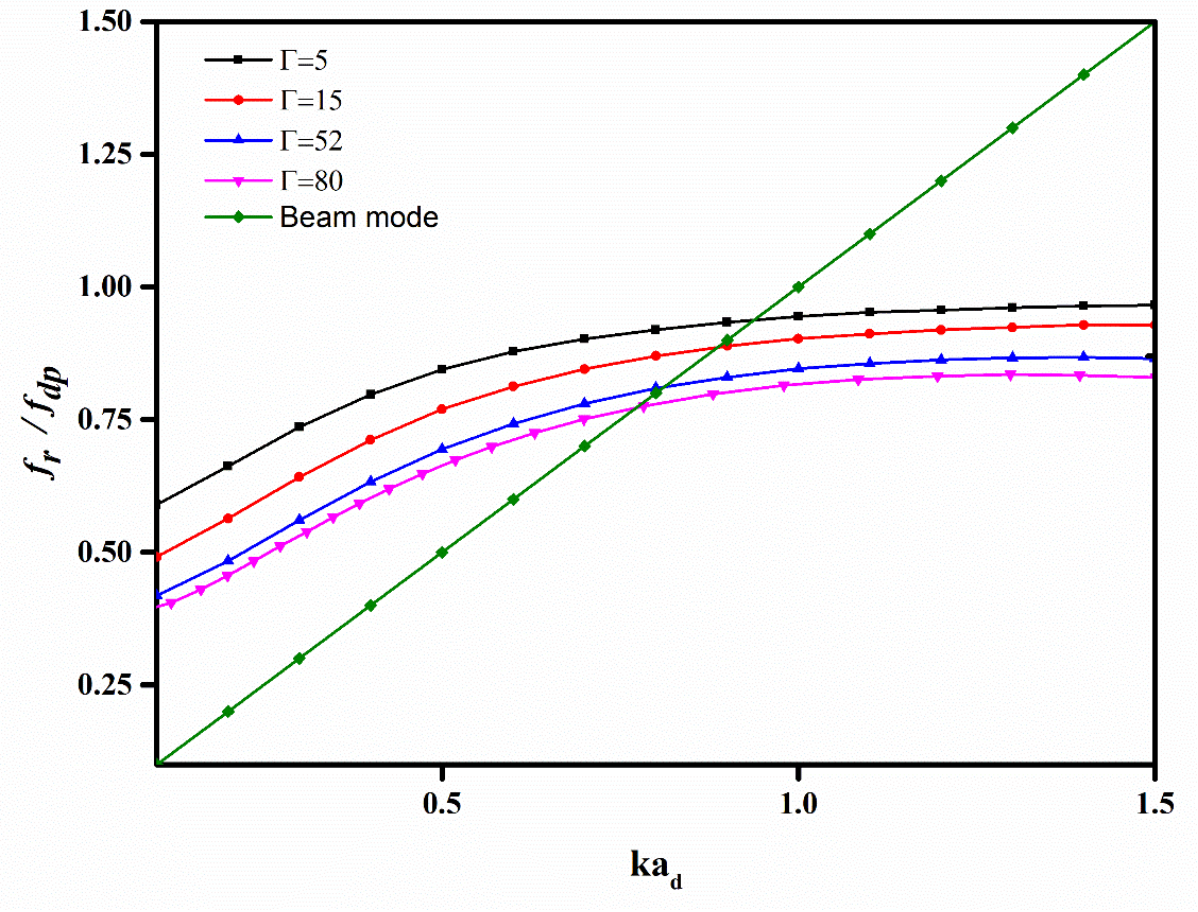

Fig.3.1 Variation of normalized frequency (f_r / f_{dp}) as a function of normalized wave vector (ka_d) for different values of strong coupling parameter Γ. The beam mode is represented by the green straight line corresponding to $\omega = k_z v_{0b}$.

Fig.3.1 reflects that the frequency of RTI grows steadily with the normalized wavevector in the long wavelength regime. The points of intersection of RTI mode with the beam mode gives frequencies and the corresponding wave numbers of the unstable waves. It has been observed that the normalized frequency of RTI descends with strong coupling parameters in the presence of an ion beam. It is observed that the frequency of beam driven instability is large for low values of strong coupling parameter, however, an increase in strong coupling parameter further decreases the frequency of unstable mode.

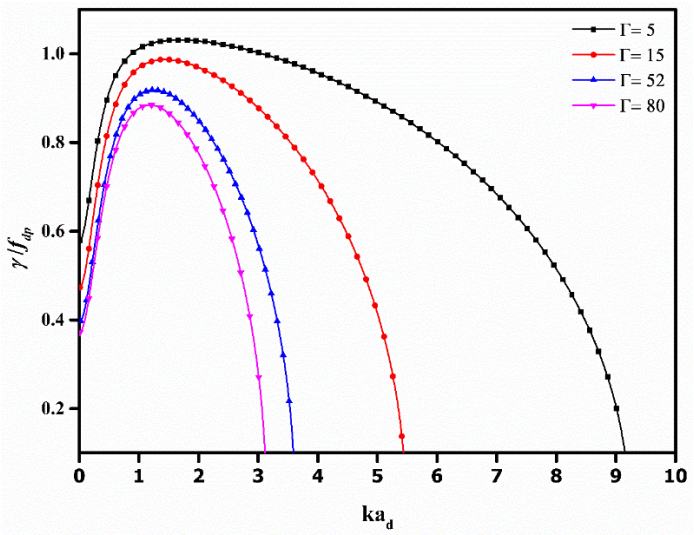

Fig. 3.2 Normalised growth rate (γ / f_{dp}) as a function of normalised wave vector (ka_d) for different values of Strong coupling parameter Γ.

The variation of the growth rate of beam driven instability with wave vectors for different Γ values has been depicted in Fig.3.2. RTI growth rate is large in the long wavelength region, and it stabilises in the shorter wavelength (i.e. high frequency region) meaning larger perturbations with longer wavelength evolve more rapidly than the smaller perturbations with shorter wavelength.

It may be attributed to the fact that potential energy stored in the density gradient is transferred to the instability in the form of kinetic energy, larger perturbations can tap more energy from the potential energy compared to the smaller perturbations. This fact indicates as there is less "resistance" from the surrounding fluid, larger perturbations can grow more quickly than smaller ones, which are more readily damped. The RTI growth rate is suppressed due to the increase in strong coupling parameter. This behaviour can be understood as the value of Γ increases the system behaves more like a solid, by losing its fluid-like properties necessary for the quick evolution of the instability. Further, the strong correlation leads to the “Caging” **[42]** effect where the neighbouring particles trap each other and restricts their movement and consequently limiting the growth of instability. The viscoelastic behaviour of the fluid comes into play as the value of Γ increases further dampening the growth rate of instability.

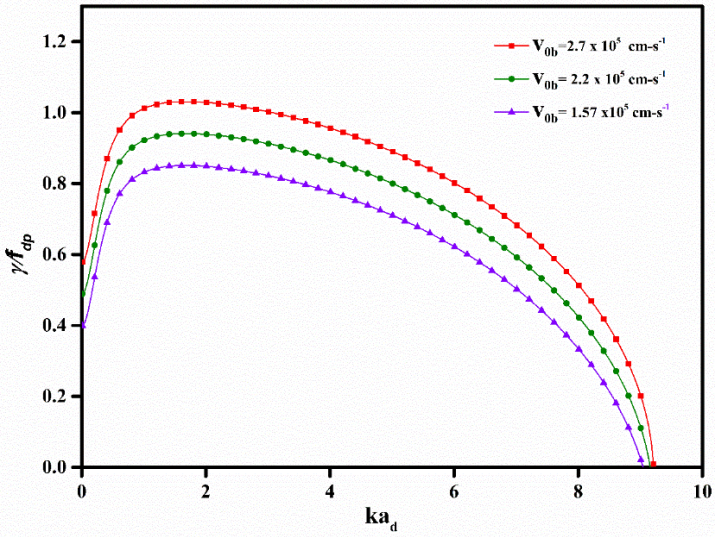

Fig.3.3 Variation of normalised growth rate(γ / f_{dp}) versus normalised wave(ka_d) vector for different beam velocities (v_{0b}) for strong coupling parameter Γ=15.

The variation of normalised growth rate as a function of normalised wavevector is studied for Γ=15 in Fig. 3.3 for different ion beam velocities i.e., energy of the beam. Here $v_{0b} = \sqrt{\frac{2E_b}{m_i}}$, is the beam velocity, E_b is beam energy and m_i is the mass of ion. v_{0b} =1.57×10^5cms^{-1}, 2.2×10^5 cms^{-1} , 2.7×10^5 cms^{-1} for E_b = 0.5eV, 1eV and 1.5eV, respectively. Higher beam velocity leads to a rapid and enhanced growth rate of RTI than for small beam energies because the beam's kinetic energy is transferred to the medium which causes the perturbations to grow quicker **[43]**.

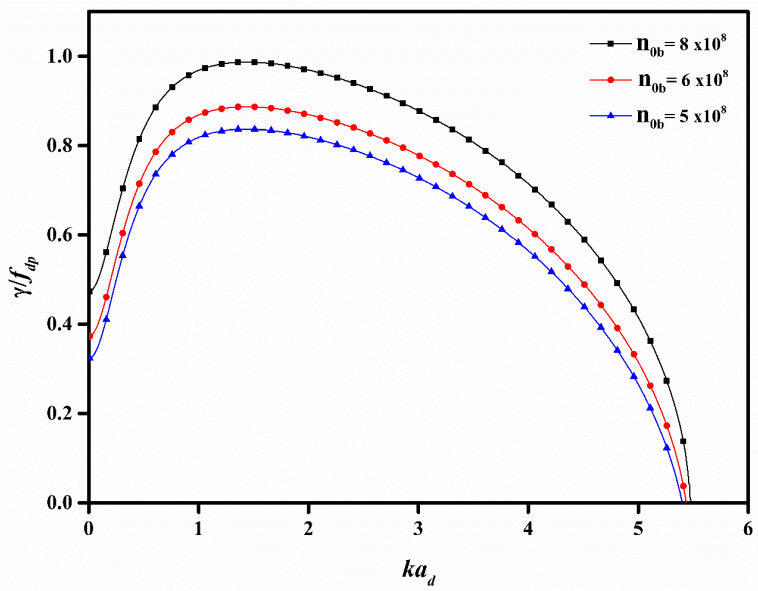

Fig.3.4 Variation of Normalised growth rate (γ / f_{dp}) Vs. normalised wavevector (ka_d) for different values of beam density n_{0b} in cm^{-3} at strong coupling parameter Γ=15.

The effect of beam density parameter on the growth rate has been analysed by plotting normalised growth rate as a function of the normalised wave vector for different values of the beam density parameter n_{0b}=$5\times10^{8}(cm^{-3})$, $n_{0b}=6\times10^{8}(cm^{-3})$ and $n_{0b}=8\times10^{8}(cm^{-3})$ in Fig. 3.4. It has been found that the growth rate is higher for higher beam densities as higher beam density leads to a larger momentum transfer to the plasma **[44]**, which aids in the growth rate of the perturbation. In the beam-plasma interaction, density perturbation at the interface leads to the evolution of RTI.

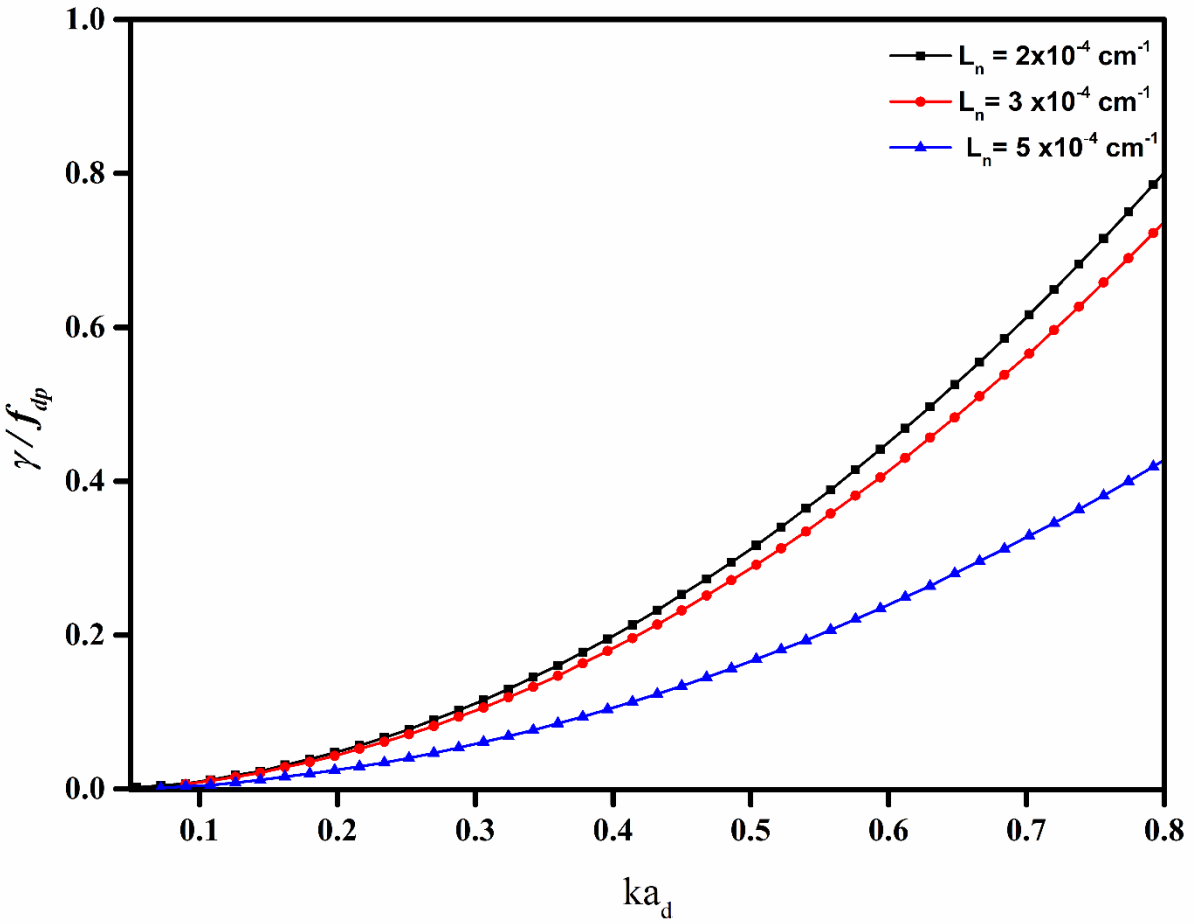

Fig. 3.5 Normalised growth rate(γ / f_{dp}) as a function of normalised wave vector (ka_d) for different density scale length (L_n) in cm^{-1} at the strong coupling parameter Γ=15.

It is clear from Fig. 3.5 that for a shorter scale length L_n (i.e., steeper density gradient of plasma) instability grows more rapidly; conversely longer density scale length (i.e., gradual density gradient) leads to slow growth of the instability stabilising the plasma system to some extent. This can be attributed to the fact the smaller density gradient reduces the driving force behind RTI leading to smaller growth rate **[45]**.

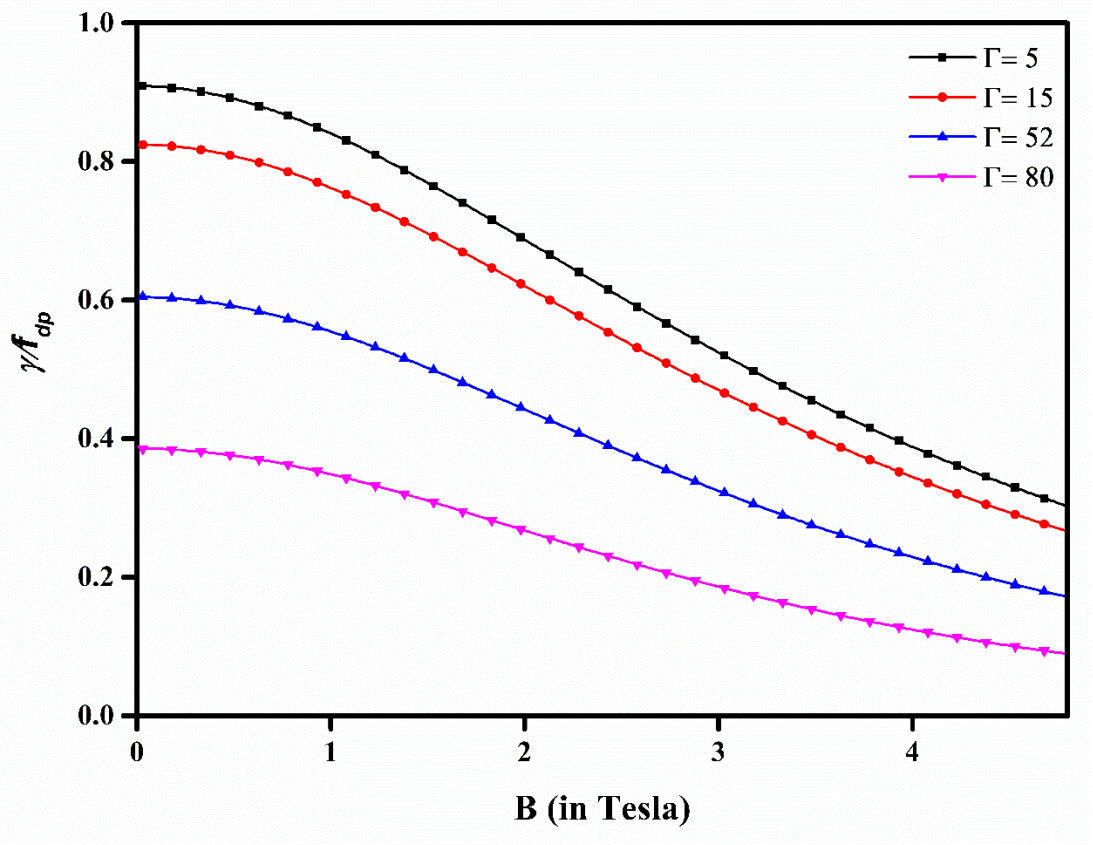

Fig. 3.6. Variation of normalised growth rate(γ / f_{dp}) with magnetic field B for various values of strong coupling Parameter Γ.

The effect of the magnetic field on the instability growth rate has been analysed by plotting the normalised growth rate against the magnetic field for different values of strong coupling parameter in Fig. 3.6. The instability is suppressed with the increase in the value of the magnetic field. This can be ascribed to the fact that the magnetic field introduces magnetic tension which counteracts against the driving force of the RTI, effectively limiting the growth rate of instability **[46]**. This magnetic tension opposes the fluid motion leading to stabilization of instability growth rate which is an important aspect of inertial confinement fusion devices. Additionally, the onset of quantum effects also aid in the suppression of the instability **[27]**.

3.4 Summary

To summarise we have systematically analysed beam driven Rayleigh Taylor instability's by using the GHD model. The combined effects of beam parameters, coupling strength and density scale length on frequency and growth rate have been taken into account. With the increase in coupling strength, the instability is suppressed, owing to the viscoelastic response of the medium that provides an elastic restoring force against perturbation. The instability growth rate is enhanced with a denser and higher energy beam, whereas the magnetic field has a dampening effect on the instability. Due to its prominence in the ICF and dwarf star, our results may be utilised for the mitigation strategies for the effects of RTI.

References

[1] Chandrasekhar S 1961 Hydrodynamic and hydromagnetic stability.

[2] Rayleigh 1882 Investigation of the Character of the Equilibrium of an Incompressible Heavy Fluid of Variable Density Proc. Lond. Math. Soc. s1-14 170–7.

[3] Srinivasan B, Dimonte G and Tang X-Z 2012 Magnetic field generation in Rayleigh-Taylor unstable inertial confinement fusion plasmas Phys. Rev. Lett. 108 165002.

[4] Kawata S 2021 Direct-drive heavy ion beam inertial confinement fusion: a review, toward our future energy source Adv. Phys. X 6 1873860.

[5] Yamanaka C 1999 Inertial confinement fusion: The quest for ignition and energy gain using indirect drive Nucl. Fusion 39 825–7.

[6] Komori A, Sato N and Hatta Y 1978 Excitation and Control of the Rayleigh-Taylor Instability in a Plasma with a Curved Magnetic Field Phys. Rev. Lett. 40 768–71.

[7] Sgattoni A, Sinigardi S, Fedeli L, Pegoraro F and Macchi A 2015 Laser-driven Rayleigh-Taylor instability: Plasmonic effects and three-dimensional structures Phys. Rev. E 91 013106.

[8] Kuranz C C, Park H-S, Huntington C M, Miles A R, Remington B A, Plewa T, Trantham M R, Robey H F, Shvarts D, Shimony A, Raman K, MacLaren S, Wan W C, Doss F W, Kline J, Flippo K A, Malamud G, Handy T A, Prisbrey S, Krauland C M, Klein S R, Harding E C, Wallace R, Grosskopf M J, Marion D C, Kalantar D, Giraldez E and Drake R P 2018 How high energy fluxes may affect Rayleigh–Taylor instability growth in young supernova remnants Nat. Commun. 9 1564.

[9] Rigon G, Casner A, Albertazzi B, Michel Th, Mabey P, Falize E, Ballet J, Van Box Som L, Pikuz S, Sakawa Y, Sano T, Faenov A, Pikuz T, Ozaki N, Kuramitsu Y, Valdivia M P, Tzeferacos P, Lamb D and Koenig M 2019 Rayleigh-Taylor instability experiments on the LULI2000 laser in scaled conditions for young supernova remnants Phys. Rev. E 100 021201.

[10] Clemens N T and Mungal M G 1995 Large-scale structure and entrainment in the supersonic mixing layer J. Fluid Mech. 284 171–216.

[11] Nakai S and Takabe H 1996 Principles of inertial confinement fusion - physics of implosion and the concept of inertial fusion energy Rep. Prog. Phys. 59 1071–131.

[12] Nakai S and Mima K 2004 Laser driven inertial fusion energy: present and prospective Rep. Prog. Phys. 67 321–49.

[13] Chu J H, Du J-B and I L 1994 Coulomb solids and low-frequency fluctuations in RF dusty plasmas J. Phys. Appl. Phys. 27 296–300.

[14] Pieper J B, Goree J and Quinn R A 1996 Experimental studies of two-dimensional and three-dimensional structure in a crystallized dusty plasma J. Vac. Sci. Technol. Vac. Surf. Films 14 519–24.

[15] Chu J H and I L 1994 Direct observation of Coulomb crystals and liquids in strongly coupled rf dusty plasmas Phys. Rev. Lett. 72 4009–12.

[16] Das A and Kaw P 2014 Suppression of Rayleigh Taylor instability in strongly coupled plasmas Phys. Plasmas 21 062102.

[17] Avinash K and Sen A 2015 Rayleigh-Taylor instability in dusty plasma experiment Phys. Plasmas 22 083707.

[18] Golden K I and Kalman G J 2000 Quasilocalized charge approximation in strongly coupled plasma physics Phys. Plasmas 7 14–32.

[19] Khrapak S A 2016 Thermodynamics of Yukawa systems and sound velocity in dusty plasmas Plasma Phys. Control. Fusion 58 014022.

[20] Kumar P and Sharma D 2021 Collective excitations of rotating dusty plasma under quasi-localized charge approximation of strongly coupled systems Phys. Plasmas 28 083704.

[21] Dalui S, Kumar P, Jana P and Sharma D 2025 Quantitative analysis of modulational instability in Yukawa fluids Phys. Plasmas 32 083701.

[22] Rozina C, Sania B, Poedts S, Ali S and Maryam N 2023 Rayleigh-Taylor instability in an adiabatic-radiative rare plasma Phys. Scr. 98 045616.

[23] Prajapati R P 2016 Rayleigh-Taylor instability in non-uniform magnetized rotating strongly coupled viscoelastic fluid Phys. Plasmas 23 022106.

[24] Wang L F, Yang B L, Ye W H and He X T 2012 Stabilization of the Rayleigh-Taylor instability in quantum magnetized plasmas Phys. Plasmas 19 072704.

[25] Khan N and Sharma P K 2023 Investigation of Rayleigh–Taylor instability and internal waves in strongly coupled rotating magnetized quantum plasma J. Astrophys. Astron. 44 7.

[26] Sun Y B, Zeng R H and Tao J J 2021 Effects of viscosity and elasticity on Rayleigh–Taylor instability in a cylindrical geometry Phys. Plasmas 28 062701.

[27] Hoshoudy G A 2009 Quantum effects on the Rayleigh–Taylor instability of stratified fluid/plasma through porous media Phys. Lett. A 373 2560–7.

[28] Kählert H, Carstensen J, Bonitz M, Löwen H, Greiner F and Piel A 2012 Magnetizing a Complex Plasma without a Magnetic Field Phys. Rev. Lett. 109 155003.

[29] Bhambhu R and Prajapati R P 2024 Radiation pressure-driven Rayleigh–Taylor instability in compressible strongly magnetized ultra-relativistic degenerate plasmas Phys. Plasmas 31 082708.

[30] Dolai B and Prajapati R P 2018 The rotating Rayleigh-Taylor instability in a strongly coupled dusty plasma Phys. Plasmas 25 083708.

[31] Bera R K, Song Y and Srinivasan B 2022 The effect of viscosity and resistivity on Rayleigh–Taylor instability induced mixing in magnetized high-energy-density plasmas J. Plasma Phys. 88 905880209.

[32] Bhambhu R and Prajapati R P 2024 Radiation pressure-driven Rayleigh–Taylor instability in compressible strongly magnetized ultra-relativistic degenerate plasmas Phys. Plasmas 31 082708.

[33] Wani R, Verma M and Tiwari S 2024 Rayleigh–Taylor turbulence in strongly coupled dusty plasmas Phys. Plasmas 31 082306.

[34] Kaw P K and Sen A 1998 Low frequency modes in strongly coupled dusty plasmas Phys. Plasmas 5 3552–9.

[35] Ichimaru S, Iyetomi H and Tanaka S 1987 Statistical physics of dense plasmas: Thermodynamics, transport coefficients and dynamic correlations Phys. Rep. 149 91–205.

[36] Slattery W L, Doolen G D and DeWitt H E 1980 Improved equation of state for the classical one-component plasma Phys. Rev. A 21 2087–95.

[37] Slattery W L, Doolen G D and DeWitt H E 1982 N dependence in the classical one-component plasma Monte Carlo calculations Phys. Rev. A 26 2255–8.

[38] Sünder D 1986 Principles of Plasma Electrodynamics. By A. F. Alexandrov, L. S. Bogdankevich, A. A. Rukhadze. Springer-Verlag. Berlin, Heidelberg, New York, Tokio. 1984. Springer Series in Electrophysics, Volume 9; edited by G. Ecker (Ruhr-Universität Bochum) Beitr. Aus Plasmaphys. 26 142–142.

[39] Abramowitz M, Stegun I A and Romer R H 1988 Handbook of Mathematical Functions with Formulas, Graphs, and Mathematical Tables Am. J. Phys. 56 958–958.

[40] Cao J, Ren H, Wu Z and Chu P K 2008 Quantum effects on Rayleigh–Taylor instability in magnetized plasma Phys. Plasmas 15 012110.

[41] Shampine L F and Reichelt M W 1997 The MATLAB ODE Suite SIAM J. Sci. Comput. 18 1–22.

[42] Donkó Z, Kalman G J and Golden K I 2002 Caging of Particles in One-Component Plasmas Phys. Rev. Lett. 88 225001.

[43] Mikhaeil M, Suchandra P, Ranjan D and Pathikonda G 2021 Simultaneous velocity and density measurements of fully developed Rayleigh-Taylor mixing Phys. Rev. Fluids 6 073902.

[44] Sun W, Lv C, Feng L, Wang J, Wang Z and He C 2023 Numerical study of the effect of a magnetic field on Rayleigh-Taylor instability with different density disturbances Front. Phys. 11 1203081.

[45] Song Y, Wang P and Wang L 2021 Numerical investigations of Rayleigh–Taylor instability with a density gradient layer Comput. Fluids 220 104869.

[46] Rudraiah N, Krishnamurthy B S, Jalaja A S and Desai T 2004 Effect of a magnetic field on the growth rate of the Rayleigh–Taylor instability of a laser-accelerated thin ablative surface Laser Part. Beams 22 29–33.

Chapter 4

Effect of Dust-Polarisation on Ion-Beam driven Kelvin Helmholtz Instability in a magnetised Dusty Plasma

4.1 Introduction

Among various plasma instabilities, the Kelvin–Helmholtz instability (KHI) plays a central role in the transport of mass, momentum, and energy in systems with velocity shear **[1,2]**. KHI has been extensively studied in space plasmas, particularly at planetary magnetopauses **[3]**, in solar wind–magnetosphere interactions **[4]**, comets **[5]** , and in astrophysical shear layers. In magnetized plasmas, the presence of a magnetic field modifies the instability threshold and growth rate through magnetic tension and compressibility effects **[6]**.

In dusty plasmas, the instability becomes more complex due to additional forces associated with dust inertia, dust charging, and collective dust dynamics. D'Angelo and Song **[7]** studied KHI in magnetized plasma for both negatively and positively charged dust. They evaluated the critical shear as a function of the charge carried by dust grains. Rawat and Rao **[8]** analysed the critical shear needed to trigger the KHI as a function of the equilibrium ratio of dust to ion charge density and showed that instability occurs only when the relative velocity between neighbouring dust fluid layers exceeds the dust-acoustic phase speed. Banerjee et al.**[9]** examined KHI in a non-Newtonian fluid using a shear rate dependent viscosity model. They found that, similar to compressibility, shear-thickening behaviour stabilizes the instability, whereas shear-thinning enhances its growth.

An et al **[10]** reported that negative ion plasma have enhanced diffusion rate due to mixing of ions in adjacent layers. Luo et al.**[11]** did the experimental analysis of the effect of negative charged dust grains on growth of KHI. The effect of grain charge fluctuation on KHI was studied by various researchers **[12–14]** . Hendrix and Keppens **[15]** observed that high dust-to-gas mass ratios are shown to significantly suppress the KHI growth rate, particularly at shorter wavelengths. Numerical simulations of KH modes in non linear regime has been done for plasma environment in noctilucent clouds by Wiechen **[16]**. Molecular dynamics (MD) simulations and Genralised Hydrodynamics (GH) model have been utilised by Ashwin and Ganesh to analyse the strong coupling effects in KHI **[17,18]**.

Moreover, in spatially nonuniform dusty plasmas, the influence of the dust polarization force has been examined in the context of different wave phenomena and plasma instabilities. When an external electric field is applied, gradients in the background plasma density lead to distortions of the dust Debye sheath, making polarization effects on dust grains significant. Consequently, polarization parameters play an important role in modifying both the dispersion relations and the instability growth rates across a wide range of laboratory and astrophysical dusty plasma conditions. The concept of the polarization force acting on a charged dust particle, along with its significance in the context of dusty plasmas, has been explained by Hamaguchi and Farouki **[19]** . The effect of dust grain polarisation on DA waves **[20]**, DA solitons **[21]**, dust acoustic cnoidal waves **[22]** have been taken into account in past by various

researchers. The polarisation effect on KHI have been studied previously in an incompressible, subsonic sheared dusty plasma while accounting for the effects of ion drag forces **[23]**. The presence of rotation, viscosity, and polarization forces leads to a reduction in the growth rate of the KHI **[24]**. Ion beams are frequently present in both laboratory and space plasmas and act as an efficient source of free energy for driving plasma instabilities. Previous studies have shown that beam-driven KHI **[25]** can significantly alter dispersion and instability thresholds.

According to our understanding the combined effect of beam and dust polarisation effect on the KHI have not been studied. Motivated by these considerations, the present work investigates the effect of dust polarisation on ion-beam driven KHI in a magnetized dusty plasma. A linear fluid model is developed that incorporates dust polarisation force along with ion beam dynamics and magnetic field effects. Thus, in the next section we will develop a theoretical model for taking into account the combined effect of ion beam dynamics and dust polarisation effects followed by the result and discussion section and conclusion.

4.2 Theoretical Model

We have considered an inhomogeneous plasma with A multispecies, collision-less, magnetized plasma column composed of electrons, ions, and charged dust grains. The externally applied magnetic field is directed along the axial direction, $B = B_o\hat{z}$. The equilibrium number density is assumed to vary radially according to $n_0 = Ne^{-\lambda r}$ where N is a constant and denotes the density gradient scale length **[11]** . The equilibrium densities of electrons, ions, and dust grains are represented by n_{0e}, n_{0i} *and* n_{0d}, respectively, while their corresponding charges, masses, and temperatures are $(-e, m_e, T_e), (e, m_i, T_i)$ and (q_{0d}, m_d, T_d) respectively. All plasma species are taken to flow along the magnetic field with an axial velocity v_{0z}. The equilibrium flow velocity is given by v_0 which is constant. The radial electric field, which could otherwise drive a transverse Kelvin–Helmholtz instability through shear in the perpendicular E×B drift, is assumed to be constant and sufficiently small so that parallel shear effects dominate **[10]**. In addition, an ion beam of mass m_b, uniform density n_{0b}, and radius r_b propagates along the magnetic field with velocity $v_{0b}\hat{z}$ through the plasma column.

The Beam plasma system prior to the perturbation is quasi-neutral and it is expressed as

$$en_{0e} - en_{0i} - en_{0b} + Q_{0d}n_{0d} = 0\,. \tag{4.1}$$

Equilibrium of the system is perturbed by an electrostatic perturbation given as

$$\phi_1 = \phi_1(r)e^{-i(ft-\vec{k}.\vec{r})}\,. \tag{4.2}$$

The Response of Plasma electron to perturbation is given by the momentum transfer equation

$$m_e\frac{d\vec{v}}{dt} = -e\vec{E} - \frac{e}{c}(\vec{v}\times\vec{B}) - \frac{\nabla(nT)}{n}\,. \tag{4.3}$$

On Linearization, we can obtain the perturbed velocity components for the plasma electrons as

$$v_{1x} = \frac{if_{ec}k_y}{f_{ec}^2 - f_1^2}\left(\frac{T_e}{m_e}\frac{n_{1e}}{n_{0e}} - e\frac{\phi_1}{m_e}\right), \tag{4.4}$$

$$v_{1y} = \frac{f_1k_y}{\left(f_{ec}^2 - f_1^2\right)}\left(\frac{e\phi_1}{m_e} - \frac{T_e}{m_e}\frac{n_{1e}}{n_{0e}}\right), \tag{4.5}$$

$$v_{1z} = -\frac{ek_z\phi_1}{m_e} + \frac{T_e}{m_e}\frac{n_{1e}}{n_{0e}}\frac{k_z}{f_1} + \frac{1}{if_1}v_{1x}\frac{\partial v_{0z}}{\partial x}, \tag{4.6}$$

where $f_{ec} = (eB_s / m_e c)$ is cyclotron frequency of electron, v_{0z} is the equilibrium velocity along the direction of applied magnetic field and $f_1 = (f - k_y v_{0y} - k_z v_{0z})$ is the doppler shifted frequency and the subscript '1' refers to the perturbed quantities. The perturbed number density for electrons and ions are obtained by substituting the perturbed velocities into the continuity equation in short wavelength limit

$$n_{1e} = \frac{n_{0e}\phi_1 e}{T_e} \ . \tag{4.7}$$

Similarly, the perturbed density of ions is given as

$$n_{1i} = \frac{n_{0i}e\phi_1}{m_i}\left(\frac{\frac{\nabla_\perp^2}{f_{ic}^2} + \frac{k_z^2}{f_1^2} + \frac{\lambda k_y}{f_1 f_{ic}} - \frac{k_y k_z}{f_1^2 f_{ic}}\frac{\partial v_{0z}}{\partial x}}{1 - \frac{k_z^2 v_{it}^2}{f_1^2} - \frac{\lambda k_y v_{it}^2}{f_1 f_{ic}} + \frac{k_y k_z v_{it}^2}{f_1^2 f_{ic}}\frac{\partial v_{0z}}{\partial x}}\right). \tag{4.8}$$

Presence of magnetic field and dust thermal force contribute to the different low frequency mode. The presence of an external electric field can cause deformation in sheath around the dust grains which provides polarisation force.

Total force acting on a dust charged grain in a non uniform plasma with external field is. In the limit $n_e T_i \ll n_i T_e$, the magnitude of polarisation force is given as

$$F = -Q\nabla\phi(1-P), \tag{4.9}$$

where P the polarisation parameter is given by $P = (1/4)(q_d e / \lambda_D \mathrm{T}_i)(1 - T_i / T_e)$, Q is charge on dust grain and λ_D is Debye length.

Modified dust momentum transfer is given by equation

$$\frac{\partial \vec{v}_d}{\partial t} - \frac{Q\nabla\phi(1-P)}{m_d} - \frac{Q}{m_d c}(\vec{v}_d \times \vec{B}) - \frac{v_{dt}^2 \nabla n_d}{m_d}, \tag{4.10}$$

Here $v_{dt}, m_d, v_{td} = \left(\frac{T_d}{m_d}\right)^{1/2}$ are the dust-fluid velocity, dust mass, and dust thermal speed.

Continuity equation for the dust fluid is given as

$$\frac{\partial n_d}{\partial t} + \nabla.(n_d v_d) = 0 \ . \tag{4.11}$$

Poisson's Equation for this configuration gives

$$\nabla^2\phi = -4\pi e(n_i - n_e) - 4\pi q_d n_d \ . \tag{4.12}$$

Linearising the equations we get the dust momentum equation as

$$\frac{\partial v_{d1}}{\partial t} = -q_{d0}\frac{\nabla\phi_1}{m_d}(1-P) - q_{d0}(v_{d1}\times \mathrm{B}) - \frac{v_{dt}^2}{n_{0d}}\nabla n_{1d}\,. \tag{4.13}$$

The continuity equation for the dust fluid becomes

$$\frac{\partial n_{1d}}{\partial t} + \vec{\nabla}.(n_{0d}v_{1d}) = 0\,, \tag{4.14}$$

Now to find the perturbed dust density , putting $\nabla = i\vec{k}$ and $\frac{\partial}{\partial t} = -if$ in eq.(4.14) we get,

$$-ifn_{1d} + n_{0d}i\vec{k}.\vec{v}_{1d} = 0$$

$$\Rightarrow \vec{k}.\vec{v}_{1d} = \frac{fn_{1d}}{n_{0d}} \tag{4.15}$$

Similarly Eq. (4.13) becomes

$$-ifv_{1d} = -\frac{q_{0d}}{m_d}ik\phi_1(1-P) - \frac{q_{0d}}{m_d c}B_0 v_{1d} - \frac{v_{dt}^2}{n_{0d}}\nabla n_{1d}$$

$$\Rightarrow -ifv_{1d} + \frac{q_{0d}}{m_d c}B_0 v_{1d} - \frac{v_{dt}^2}{n_{0d}}ikn_{1d} = -\frac{q_{0d}}{m_d}ik\phi_1(1-P)$$

Taking dot product with $\vec{k}$ both sides

$$\Rightarrow -if\vec{k}.v_{1d} + \frac{q_{0d}}{m_d}B_0\vec{k}.v_{1d} - \frac{v_{dt}^2}{n_{0d}}ik^2 n_{1d} = -\frac{q_{0d}}{m_d}ik^2\phi_1(1-P)$$

$$\vec{k}.v_{1d}(-if + \Omega_d) - v_{dt}^2 ik^2\frac{n_{1d}}{n_{0d}} = -\frac{q_{0d}}{m_d}ik^2\phi_1(1-P)$$

Substituting the value of $k.v_{1d}$ from the eq.(4.15)

$$\frac{fn_{1d}}{n_{0d}}(-if + \Omega_d) - v_{dt}^2 ik^2\frac{n_{1d}}{n_{0d}} = -\frac{q_{0d}}{m_d}ik^2\phi_1(1-P)$$

We get the perturbed dust density as

$$n_{1d} = \frac{q_{0d}n_{0d}k^2\phi_1(1-P)}{m_d\left[f^2 - i\Omega_d f - v_{dt}^2k^2\right]} \tag{4.16}$$

Where $\Omega_d = \frac{|q_{0d}|B_0}{m_d c}$ is dust cyclotron frequency

Current balance equation for charge fluctuation

$$\frac{\partial q_d}{\partial t} + v_d.\nabla q_d = I_e(q_d,\phi) + I_i(q_d,\phi) \tag{4.17}$$

With the application of Probe theory **[26–28]** to the dust grain charge on surface is balanced by the effects of plasma current

$$-\frac{\partial Q_{1d}}{\partial t} = I_{1e} + I_{1i} \tag{4.18}$$

The electron I_{1e} and ion I_{1i} currents on the surface of dust grain are given as

$$I_e = -\pi a^2 e n_e \sqrt{\frac{8KT_e}{\pi m_e}} exp\left(\frac{e}{KT_e}(\phi_m - V)\right), \tag{4.19}$$

$$I_i = -\pi a^2 e n_i \sqrt{\frac{8KT_i}{\pi m_i}} exp\left(\frac{e}{KT_i}(\phi_m - V)\right). \tag{4.20}$$

Equation for current can be expressed as $\phi_{m_1} = \frac{q_{d1}}{c}$, where c is dust capacitance

$w_0 = T_i - e\phi_{m0}$, here T_i is Ion temperature and ϕ_{m0} is the floating equilibrium potential, a is the dust grain radius , n_{0e} & n_{0i} are the electron and ion no. density in absence of dust grains, and $(\phi_m - V)$= Difference between potential on the surface of dust grains and bulk plasma potential. Under equilibrium conditions, the magnitudes of the electron and ion currents collected by a dust grain are equal, i.e., $I_{0e} = I_{0i}$, where I_{0e} and I_{0i} represent the steady-state electron and ion currents at the grain surface, respectively.

The equilibrium electron current is given as

$$I_{0e} = -\pi a^2 e n_{0e} \sqrt{\frac{8KT_e}{\pi m_e}} exp\left(\frac{e}{T_e}\phi_{m0}\right)$$

The dust charge fluctuation is found using

$$I_{1e} = I_{0e}\left[\frac{n_{1e}}{n_{0e}} + \frac{e\phi_{m1}}{KT_e}\right] \tag{4.21}$$

$$I_{1i} = I_{0i}\left[\frac{n_{1i}}{n_{0i}} - \frac{e\phi_{m1}}{w_0}\right] \tag{4.22}$$

$I_0 = -I_{oe} = I_{0i}$=equilibrium ion and electron currents ,

$$\frac{dQ_{1d}}{dt} + \eta Q_{1d} = -|I_{0e}|\left(\frac{n_{1i}}{n_{0i}} - \frac{n_{1e}}{n_{0e}}\right) \tag{4.23}$$

where $\eta = \frac{e|I_{0e}|}{C_d}\left[\frac{1}{T_e} + \frac{1}{w_0}\right]$, $Q_{1d} = Q_d - q_{0d}$ is the perturbed dust charge and C_d is the capacitance of the dust grain **[29]**.

Substituting the values of n_i, n_{1d} and n_{1e} in the eq. (4.23) we get

$$Q_{1d} = \frac{e|I_{0e}|}{i(f+i\eta)}\left[\frac{\frac{\nabla_y^2\phi_1}{m_i f_{ic}^2}+\frac{k_z^2\phi_1}{m_i f_1^2}+\frac{\lambda k_y\phi_1}{f_1 f_{ic}}-\frac{k_y k_z}{f_1^2 f_{ic}}\frac{\partial v_{0z}}{\partial x}}{1-\frac{k_z^2 v_{it}^2}{f_1^2}-\frac{\lambda k_y v_{it}^2}{f_1 f_{ic}}+\frac{k_y k_z v_{it}^2}{f_1^2 f_{ic}}\frac{\partial v_{0z}}{\partial x}}-\frac{\phi_1}{T_e}\right]. \tag{4.24}$$

By following the analysis of Sharma and Shrivastva **[30]** perturbed density for beam is given as

$$n_{1b} = \frac{n_{0b}e(k_y^2+k_z^2)\phi_1}{m_b(f_1-k_z v_{0b})^2}. \tag{4.25}$$

Substituting in the poisson's equation to obtain the dispersion relation $\nabla^2\phi_1 = 4\pi[n_{1e}e - n_{1i}e - n_{1b}e + n_{0d}Q_{1d} + Q_{0d}n_{1d}]$

$$\Rightarrow k^2\phi_1 = \frac{4\pi n_{0e}e^2\phi_1}{T_e} - \frac{4\pi n_{0i}e^2\phi_1}{m_i}\left(\frac{\frac{\nabla_\perp^2}{f_{ic}^2}+\frac{k_z^2}{f_1^2}+\frac{\lambda k_y}{f_1 f_{ic}}-\frac{k_y k_z}{f_1^2 f_{ic}}\frac{\partial v_{0z}}{\partial x}}{1-\frac{k_z^2 v_{it}^2}{f_1^2}-\frac{\lambda k_y v_{it}^2}{f_1 f_{ic}}+\frac{k_y k_z v_{it}^2}{f_1^2 f_{ic}}\frac{\partial v_{0z}}{\partial x}}\right) - \frac{4\pi n_{0b}e^2(k_y^2+k_z^2)\phi_1}{m_b(f_1-k_z v_{0b})^2}$$

$$+\frac{4\pi n_{0d}e|I_{0e}|}{i(f+i\eta)}\left[\frac{\frac{\nabla_\perp^2\phi_1}{m_i f_{ic}^2}+\frac{k_z^2\phi_1}{m_i f_1^2}+\frac{\lambda k_y\phi_1}{f_1 f_{ic}}-\frac{k_y k_z\phi_1}{f_1^2 f_{ic}}\frac{\partial v_{0z}}{\partial x}}{1-\frac{k_z^2 v_{it}^2}{f_1^2}-\frac{\lambda k_y v_{it}^2}{f_1 f_{ic}}+\frac{k_y k_z v_{it}^2}{f_1^2 f_{ic}}\frac{\partial v_{0z}}{\partial x}}-\frac{\phi_1}{T_e}\right]+\frac{4\pi q_{0d}^2 n_{0d}k^2\phi_1(1-P)}{m_d\left[f^2-i\Omega_d f-v_{dt}^2k^2\right]} \tag{4.26}$$

$$\Rightarrow 1-\frac{f_{bp}^2c_s^2\delta k^2}{f_{ip}^2(f_1-k_z v_{0b})^2}-\frac{k_z^2\alpha_1^2}{f_1^2}-\frac{\lambda k_y\alpha_1^2}{f_1 f_{ic}}+\frac{k_y k_z\alpha_1^2}{f_1^2 f_{ic}}\frac{\partial v_{0z}}{\partial x}-\frac{i\beta}{f+i\eta}\left(\frac{k_z^2c_s^2}{f_1^2}+\frac{\lambda k_y c_s^2}{f_1 f_{ic}}-\frac{k_y k_z c_s^2}{f_1^2 f_{ic}}\frac{\partial v_{0z}}{\partial x}\right)$$

$$+\frac{4\pi q_{0d}^2 n_{0d}(1-P)}{m_d\left[f^2-i\Omega_d f-v_{dt}^2k^2\right]}\left(1-\frac{k_z^2v_{it}^2}{f_1^2}-\frac{\lambda k_y v_{it}^2}{f_1 f_{ic}}+\frac{k_y k_z v_{it}^2}{f_1^2 f_{ic}}\frac{\partial v_{0z}}{\partial x}\right)=0. \tag{4.27}$$

Here, $f_{bp} = (4\pi n_{0b}e^2/m_b)^{1/2}$, $f_{ip} = (4\pi n_{0i}e^2/m_i)^{1/2}$ $f_{dp} = (4\pi n_{0d}Q_{0d}e^2/m_d)^{1/2}$ are the plasma frequencies of beam, ions and dust grains respectively. Also,

$$\beta = \frac{|I_{0e}|}{c}\frac{n_{0d}}{n_{0e}} \qquad \delta = \frac{n_{oi}}{n_{0e}}, \quad v_{et} = \left(\frac{T_e}{m_e}\right)^{1/2},$$

$$\alpha_1^2 = v_{it}^2 + c_s^2\delta - \frac{f_{bp}^2c_s^2\delta v_{it}^2(k_y^2+k_z^2)}{f_{ip}^2(f_1-k_z v_{0b})^2} \quad \text{and} \quad \alpha_2^2 = \alpha_1^2 + (i\beta/(f+i\eta))c_s^2$$

$$k^2 \simeq k_\perp^2 \simeq k_y^2 \qquad \because k_\perp^2 \gg k_z^2 \text{ also } \frac{f_{pd}^2}{f_1^2} \ll 1 \quad .$$

$$\Rightarrow f_1^2\left[1+\frac{4\pi q_{0d}^2 n_{0d}(1-P)}{m_d\left[f^2-v_{dt}^2k^2\right]}-\frac{f_{bp}^2c_s^2\delta(k_y^2+k_z^2)}{f_{ip}^2(f_1-k_zv_{0b})^2}\right]-\frac{f_1.\lambda k_y}{f_{ic}}\left[\alpha_2^2+\frac{4\pi q_{0d}^2 n_{0d}(1-P)v_{it}^2}{m_d\left[f^2-v_{dt}^2k^2\right]}\right]$$

$$-k_z^2\left[\alpha_2^2+\frac{4\pi q_{0d}^2 n_{0d}(1-P)v_{it}^2}{m_d\left[f^2-v_{dt}^2k^2\right]}\right]+\frac{k_yk_z}{f_1^2f_{ic}}\frac{\partial v_{0z}}{\partial x}\left[\alpha_2^2+\frac{4\pi q_{0d}^2 n_{0d}(1-P)v_{it}^2}{m_d\left[f^2-v_{dt}^2k^2\right]}\right]=0\,. \tag{4.28}$$

Simplifying it we get

$$f_1^2\left[1+\frac{f_{dp}^2(1-P)}{\left[f^2-v_{dt}^2k^2\right]}-\frac{f_{bp}^2c_s^2\delta(k_y^2+k_z^2)}{f_{ip}^2(f_1-k_zv_{0b})^2}\right]-\frac{f_1.\lambda k_y}{f_{ic}}\left[\alpha_2^2+\frac{f_{dp}^2(1-P)v_{it}^2}{\left[f^2-v_{dt}^2k^2\right]}\right]-k_z^2\left[\alpha_2^2+\frac{f_{dp}^2(1-P)v_{it}^2}{\left[f^2-v_{dt}^2k^2\right]}\right]$$

$$+\frac{k_yk_z}{f_1^2f_{ic}}\frac{\partial v_{0z}}{\partial x}\left[\alpha_2^2+\frac{f_{dp}^2(1-P)v_{it}^2}{\left[f^2-v_{dt}^2k^2\right]}\right]=0\,. \tag{4.29}$$

Let $\left[1+\frac{f_{dp}^2(1-P)}{\left[f^2-v_{dt}^2k^2\right]}-\frac{f_{bp}^2c_s^2\delta(k_y^2+k_z^2)}{f_{ip}^2(f_1-k_zv_{0b})^2}\right]=S$ & $\left[\alpha_2^2+\frac{f_{dp}^2(1-P)v_{it}^2}{\left[f^2-v_{dt}^2k^2\right]}\right]=\alpha_3^2$

Eq. (4.29) can be rewritten as

$$\Rightarrow f_1^2-\frac{f_1.\lambda k_y}{f_{ic}}\frac{\alpha_3^2}{S}-k_z^2\frac{\alpha_3^2}{S}+\frac{k_yk_z}{f_1^2f_{ic}}\frac{\partial v_{0z}}{\partial x}\frac{\alpha_3^2}{S}=0$$

$$\Rightarrow\left(\frac{f_1}{f_{ic}}\right)^2-\left(\frac{f_1}{f_{ic}}\right)\frac{\lambda k_y}{f_{ic}^2}\frac{\alpha_3^2}{S}-k_z^2\frac{\alpha_3^2}{f_{ic}^2S}+\frac{k_yk_z}{f_1^2f_{ic}}\frac{\partial v_{0z}}{\partial x}\frac{\alpha_3^2}{f_{ic}^2S}=0\,.$$

The dispersion relation for the KHI that is driven by the ion beam is given as

$$\Omega^2-\frac{\beta_1\Lambda\Omega}{S}-\frac{\gamma(\gamma-\beta_1\mu)}{S}=0\,. \tag{4.30}$$

Here $\frac{f_1}{f_{ic}}=\Omega$, $\rho_i^2=\frac{\alpha_3^2}{f_{ic}^2}$, $\Lambda=\lambda\rho_i, \gamma=k_z\rho_i, \beta_1=k_y\rho_i$ and $\mu=\frac{1}{f_{ic}}\frac{\partial v_{0z}}{\partial x}$ is shear parameter. In

Also, we have imposed the conditions $\beta_1^2\le 1$ (i.e. $k_y^2\rho_i^2\le 1$) and $\gamma^2\le 1$ (i.e. $k_z^2\rho_i^2\le 1$), which imply that the ion Larmor radius is smaller than both the perpendicular and parallel wavelengths of the perturbation. In the absence of the ion beam and dust grain polarisation our dispersion relation is same as obtained by Luo et al. **[11]**, and and D'Angelo and Song **[7]** We

express the wave frequency as $f_1 = f_{1r} + if_{1i}$ and assume that the mode is either weakly damped or unstable, such that $(|f_{ir}| \ll |f_{1i}|)$

From dispersion relation (4.30) we have obtained the maximised growth rate Γ $(= f_{1i} / f_{ic})$

$$\Omega = \frac{f_1}{f_{ic}} = \frac{f_r}{f_{ic}} + i\frac{f_i}{f_{ic}} = \Omega_r + i\Gamma$$

$$\Omega = \frac{\beta_1 \Lambda}{2Q} \pm \sqrt{\left(\frac{\beta_1 \Lambda}{2Q}\right)^2 + \frac{\gamma(\gamma - \beta_1 \mu)}{Q}}\,.$$

The maximised growth rate is given by

$$\frac{d\Gamma}{d\gamma} = \frac{2\gamma}{Q} - \frac{\beta_1 \mu}{Q} = 0 \Rightarrow \gamma = \frac{\beta_1 \mu}{2}\,.$$

$$\Omega = \frac{\beta_1 \Lambda}{2Q} + i\left[\frac{1}{4}\beta_1^2\left(\frac{\mu^2}{Q} - \frac{\Lambda^2}{Q^2}\right)\right]^{1/2}\,.$$

$$\Gamma = \left[\frac{1}{4}\beta_1^2\left(\frac{\mu^2}{Q} - \frac{\Lambda^2}{Q^2}\right)\right]^{1/2}\,. \tag{4.31}$$

In the absence of beam, grain charge fluctuation and grain polarisation Eq. (4.31) becomes similar to that of Luo et al. **[11]**(see Eq. (2))

4.3 Results and Discussion

We have utilised the following experimental parameters $n_{0d} = 5\times10^{-9}$, dust size $a = 0.4\times10^{-4}$, $B_S \approx 3\times10^3 G$, $k_y = 1\,cm^{-1}$, scale length $\lambda = 2cm^{-1}$, shear parameter $\mu \approx$ 0.6-2.0, We have utilised the beam parameters as energy of the beam $E_B = 6-10\,eV$, $r_0 = 3\,cm$ is the beam radius and n_{0b} *is* the beam density .

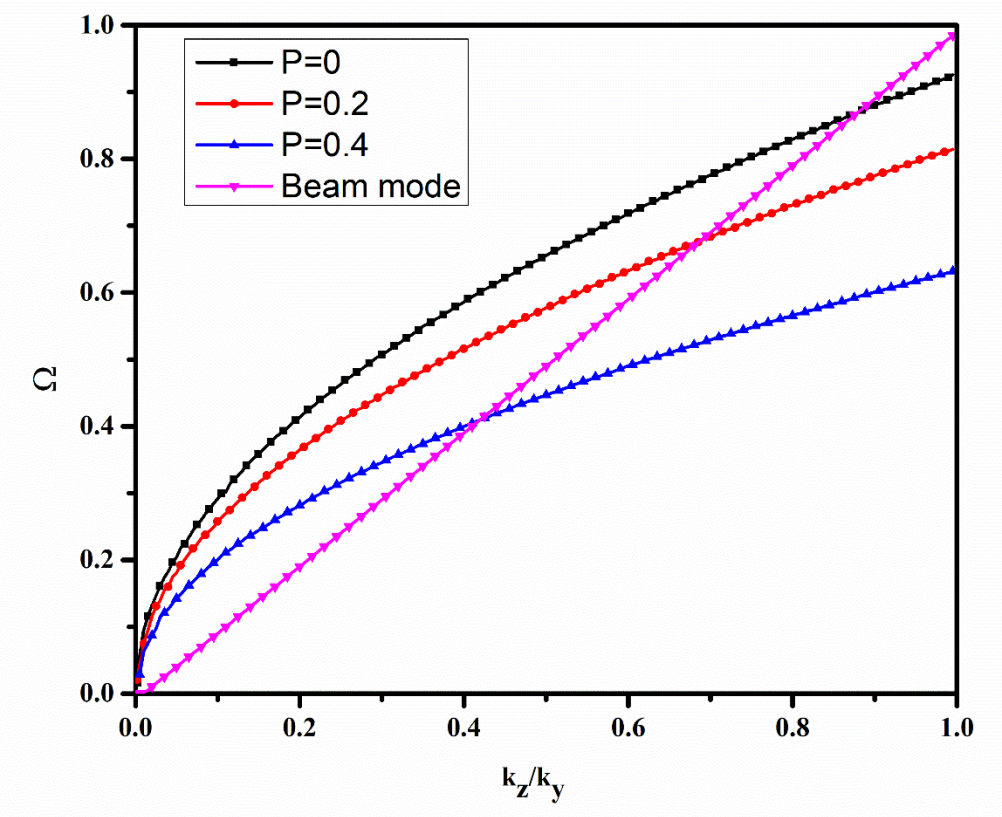

Fig. 4.1 Variation of the normalised real frequency Ω versus the normalised wave vector k_z / k_y for different P values.The pink line corresponds to beam mode $f = k_z v_{0b}$

We have plotted the dependence of real frequency of the KHI mode and beam mode $f = k_z v_{0b}$ on the normalised wave vector (cf. Fig. 4..1) for different polarisation parameter P .The real frequency increase with the increase in wave number. In the long-wavelength (low-frequency) region, dust polarisation results in a reduction of the real frequency of the wave modes. This may be attributed to the fact that it opposes the electrostatic field, and effectively "cancels out" a portion of the restoring force that would otherwise drive the wave oscillation. The real frequency of a wave is determined by the "stiffness" of the medium (its ability to return to equilibrium). Because the polarization force opposes the primary electrostatic restoring force, it effectively "softens" the medium. This reduces the net restoring force on the dust grains.

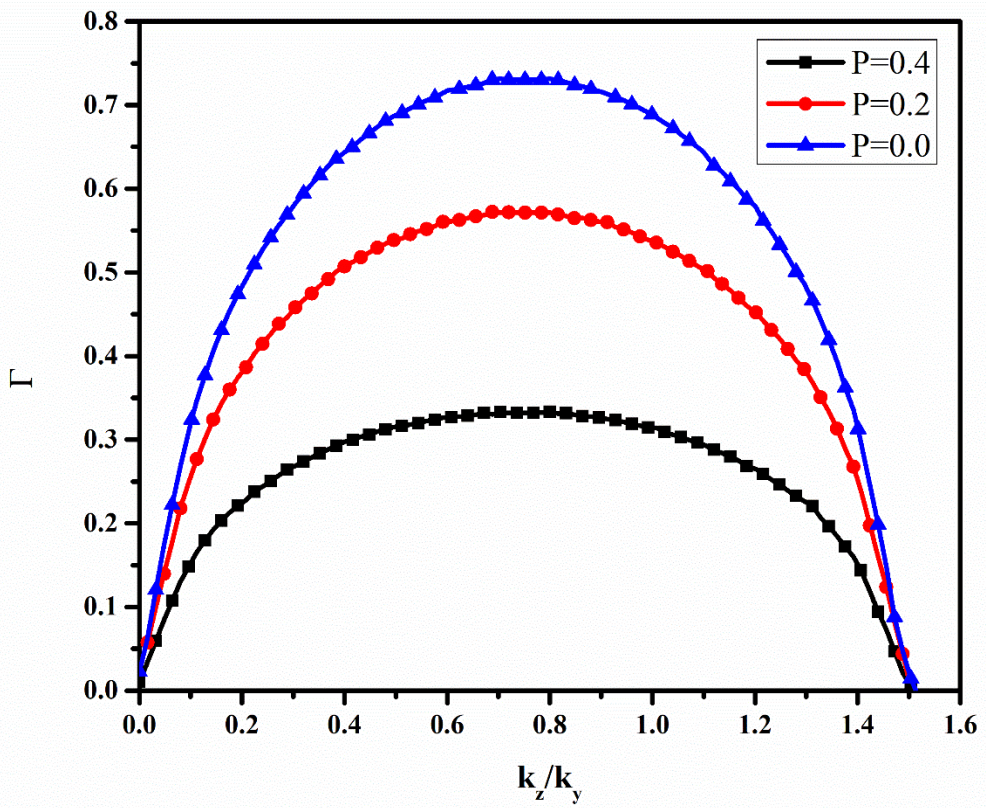

Fig.4.2 Normalised growth rate Γ of the instability versus the normalised wave no, k_z / k_y for different P values.

The effect of grain polarisation on the growth of KH mode has been analysed (cf. fig.4.2) by plotting the dependence of growth rate of KHI on the normalised wave vector for different values of polarisation parameter. The polarization force acts as a restoring force, which generally opposes the perturbations that drive the KHI. Physically, the polarization force acts opposite to the electrostatic force, effectively reducing the net restoring force and damping the wave-like perturbations that drive KHI.

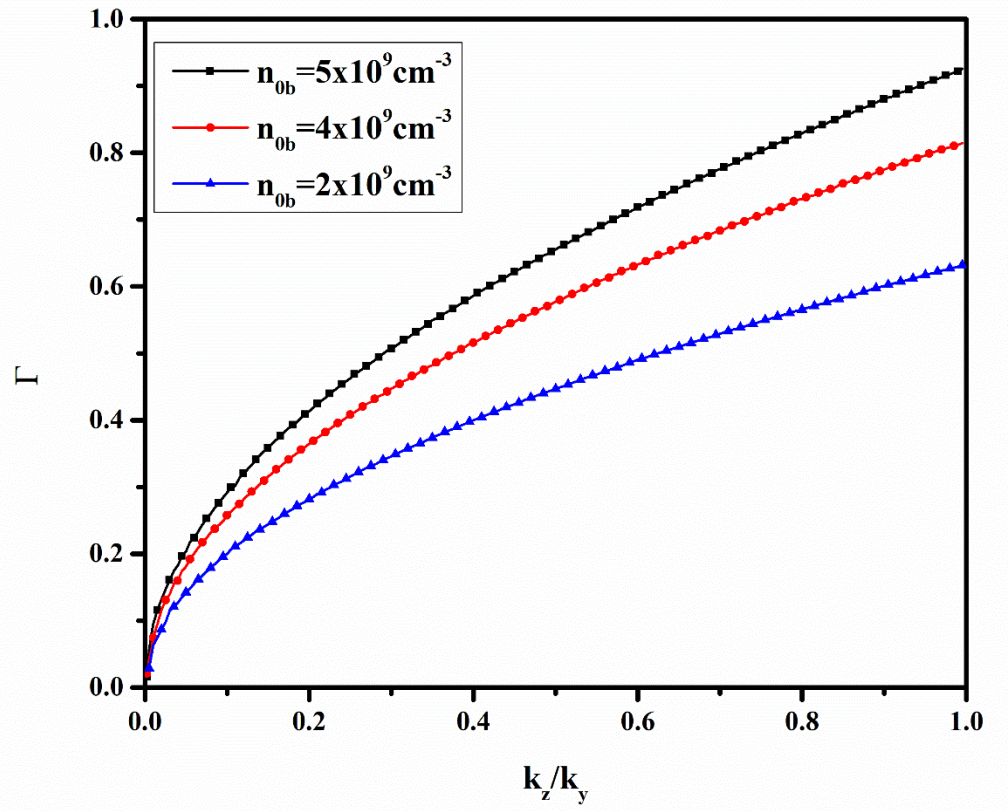

Fig. 4.3 Variation of normalised growth rate Γ versus the normalised wave vector k_z / k_y for different ion beam density n_{0b}.

We have studied the effect of beam density on the instability growth rate. The growth rate of the instability is plotted in the long wavelength region . Different ion beam density is considered i.e. $n_{0b} = 5\times10^9 cm^{-3}, 4\times10^9 cm^{-3}$ & $2\times10^9 cm^{-3}$ .The beam interacts with the plasma through the Cerenkov interaction $\left(f = k_z v_{0b}\right)$ and it alters the dynamics of the plasma system. Increasing ion beam density enhances the growth rate of the Kelvin-Helmholtz Instability (KHI) through Cerenkov interaction, making it grow faster. Larger density of beam particle allows more transfer of momentum from beam particles to the plasma. Consequently a more vigorous instability growth rate is observed . In essence, a denser ion beam fuels the KHI, making it more vigorous.

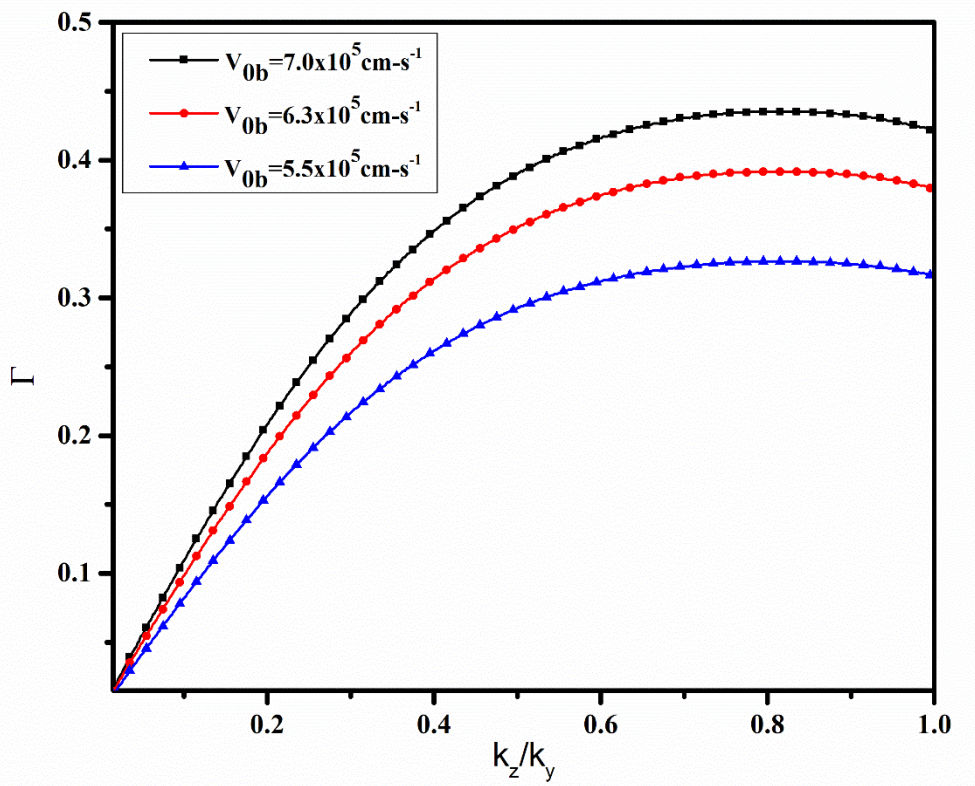

Fig. 4.4 Normalised Growth rate as a function of normalised wave vector for different velocity of beam particles.

The effect of the energy (velocity) of the beam has been analysed by plotting the variation of the normalised growth rate versus normalised wave vector for different ion beam velocities. . The ion beam velocities (energies) considered are $v_{0b} = 7\times10^5, 6.3\times10^5 \, and \, 5.5\times10^5$ corresponding to the beam energy $E_b = 10, 8 \, and \, 6 \, eV$. Higher growth rate is observed for faster beams; this may be happening because of a larger momentum is transferred to the plasma particles when they interact with the beam which has particles with more energy.

4.4 Conclusion

This study examines the combined effects of dust polarization and ion-beam dynamics on the Kelvin–Helmholtz instability (KHI) in a magnetized dusty plasma using a linear fluid model. The results show that dust polarization reduces the real frequency and suppresses the growth rate of the ion-beam–driven KHI by opposing the electrostatic restoring force, particularly in the long-wavelength regime. In contrast, increasing ion beam density and velocity enhances instability growth through stronger momentum transfer. These findings are relevant to laboratory dusty plasma experiments, fusion devices containing dust and energetic ions, and space and astrophysical plasmas such as cometary tails and magnetospheric shear layers, where dust polarization can significantly influence plasma stability and transport

4.5 References

[1] Helmholtz H 1868 „Über discontinuierliche Flüssigkeitsbewegungen“ Sitzungsberichte der Preußischen Akademie der Wissenschaften zu Berlin 23 215–28.

[2] Thomson W 1871 XLVI. Hydrokinetic solutions and observations The London, Edinburgh, and Dublin Philosophical Magazine and Journal of Science 42 362–77.

[3] Pu Z and Kivelson M G 1983 Kelvin-Helmholtz instability at the magnetopause: Energy flux into the magnetosphere Journal of Geophysical Research: Space Physics 88 853–61.

[4] Hasegawa H, Fujimoto M, Phan T-D, Reme H, Balogh A, Dunlop M, Hashimoto C and TanDokoro R 2004 Transport of solar wind into Earth’s magnetosphere through rolled-up Kelvin–Helmholtz vortices Nature 430 755–8.

[5] Ershkovich A I 1980 Kelvin-Helmholtz instability in type-1 comet tails and associated phenomena Space Science Reviews 25 3–34.

[6] Miura A and Pritchett P L 1982 Nonlocal stability analysis of the MHD Kelvin-Helmholtz instability in a compressible plasma J. Geophys. Res. 87 7431–44.

[7] D’Angelo N and Song B 1990 The Kelvin-Helmholtz instability in dusty plasmas Planetary and Space Science 38 1577–9.

[8] Rawat S P S and Rao N N 1993 Kelvin-Helmholtz instability driven by sheared dust flow Planetary and Space Science 41 137–40.

[9] Banerjee D, Garai S, Janaki M S and Chakrabarti N 2013 Kelvin-Helmholtz instability in non-Newtonian complex plasma Physics of Plasmas 20 073702.

[10] An T, Merlino R L and D’Angelo N 1996 The effect of negative ions on the Kelvin-Helmholtz instability in a magnetized potassium plasma Physics Letters A 214 47–52.

[11] Luo Q Z, D’Angelo N and Merlino R L 2001 The Kelvin–Helmholtz instability in a plasma with negatively charged dust Physics of Plasmas 8 31–5.

[12] Singh S, Rao N and Bharuthram R 1998 The Kelvin–Helmholtz instability in the presence of dust charge fluctuations Physics of plasmas 5 2477–9.

[13] Li L, Zhong-Yuan L and Zhen-Xing L 2000 Effect of dust charge fluctuations on Kelvin–Helmholtz instability in a cold dust plasma Physics of Plasmas 7 424–7.

[14] Rao N 1999 Electrostatic modes and instabilities in nonideal dusty plasmas with sheared flows and grain charge fluctuations Physics of Plasmas 6 2349–58.

[15] Hendrix T and Keppens R 2014 Effect of dust on Kelvin-Helmholtz instabilities A&A 562 A114.

[16] Wiechen H M 2007 Simulations of Kelvin–Helmholtz modes in the dusty plasma environment of noctilucent clouds Journal of plasma physics 73 649–58.

[17] J . A and Ganesh R 2010 Kelvin Helmholtz Instability in Strongly Coupled Yukawa Liquids Phys. Rev. Lett. 104 215003.

[18] J. A and Ganesh R 2010 Parallel shear flow instabilities in strongly coupled Yukawa liquids: A comparison of generalized hydrodynamic model and molecular dynamics results Physics of Plasmas 17 103706.

[19] Hamaguchi S and Farouki R T 1994 Polarization force on a charged particulate in a nonuniform plasma Phys. Rev. E 49 4430–41.

[20] Khrapak S, Ivlev A, Yaroshenko V and Morfill G 2009 Influence of a polarization force on dust acoustic waves Physical review letters 102 245004.

[21] Mayout S, Bentabet K and Tribeche M 2016 Effect of the polarization force on the dust–acoustic soliton energy Contributions to Plasma Physics 56 99–103.

[22] Singh K, Ghai Y, Kaur N and Singh Saini N 2018 Effect of polarization force on dust-acoustic cnoidal waves in dusty plasma The European Physical Journal D 72 160.

[23] Dolai B and Prajapati R P 2022 Kelvin–Helmholtz instability in sheared dusty plasma flows including dust polarization and ion drag forces Physica Scripta 97 065603.

[24] Gwala K, Pathan T A, Pensia R K, Mansuri S and Dashora H 2024 Polarization and coriolis forces impact on the Kelvin- Helmholtz instability of viscous dusty plasma Chinese Journal of Physics 90 572–9.

[25] Segwal K R and Sharma S C 2018 Theoretical Modeling of an Ion-Beam-Driven Kelvin–Helmholtz Instability in a Plasma Cylinder Having Negatively Charged Dust Grains IEEE Transactions on Plasma Science 46 775–81.

[26] Whipple E C, Northrop T G and Mendis D A 1985 The electrostatics of a dusty plasma J. Geophys. Res. 90 7405–13.

[27] Jana M R, Sen A and Kaw P K 1993 Collective effects due to charge-fluctuation dynamics in a dusty plasma Phys. Rev. E 48 3930–3.

[28] Varma R K, Shukla P K and Krishan V 1993 Electrostatic oscillations in the presence of grain-charge perturbations in dusty plasmas Phys. Rev. E 47 3612–6.

[29] Barnes M S, Keller J H, Forster J C, O'Neill J A and Coultas D K 1992 Transport of dust particles in glow-discharge plasmas Physical review letters 68 313.

[30] Sharma S C and Srivastava M P 2001 Ion beam driven ion-cyclotron waves in a plasma cylinder with negative ions Physics of Plasmas 8 679–86.

Chapter 5

Conclusion, Social Impact and Future Scope

5.1 Conclusion

The present work highlights a detailed theoretical study of waves and instabilities in magnetized dusty plasmas, covering both weakly and strongly coupled regimes. The main objective of this work was to analyse the dispersion behaviour of magnetised dusty plasma while taking into account the effect of strong correlation, magnetic field, bounded geometry, density gradient and the polarisation effects. So that, a better understanding could be developed about the waves and instabilities in laboratory and astrophysical situations.

The results indicate that strong correlation among dust grains introduces viscoelastic behavior that significantly alters dispersion characteristics of wave and the instability thresholds. In comparison with weakly coupled plasmas, strongly coupled dusty plasmas exhibit modified dispersion characteristics while having the longitudinal mode it also exhibits a novel transverse(shear) mode. Here elastic restoring forces due to the medium and strong correlation-induced caging effects play a vital role. The analysis of beam driven Rayleigh–Taylor and Kelvin–Helmholtz instabilities further demonstrate that beam-driven flows and velocity shear act as sources of free energy that makes the instability more vigorous, strong coupling, magnetic fields, and dust polarization can effectively suppress or regulate instability growth.

The study also highlights the significance of dust charge fluctuations and finite geometry, as both factors substantially influence wave dispersion and growth rates in bounded plasma systems. Overall, the present work lay emphasis on the fact that dusty plasmas cannot be adequately described using ideal plasma models alone and require advanced theoretical frameworks to capture their complex collective behavior.

5.2 Social Impact

Although the nature of the present work is theoretical in nature but it may have some meaningful and significant impact on the society. One of the most significant areas is ongoing research in the fusion energy, where the formation of dust grains and their dynamics pose challenges to the process of plasma confinement, safety of the reactor, and material durability. By improving the understanding of wave dynamics and instability control in dust-laden plasmas, this work contributes to the broader aim of developing clean, safe, and sustainable fusion-based energy sources. The findings are also pertinent to space and atmospheric sciences, specifically for understanding the dust dynamics in in planetary magnetospheres, comets, the Earth's mesosphere, and interplanetary space. Better understanding of instabilities in dusty plasma helps into better analysis of satellite data, space weather forecasting, and the protection of space-based communication and navigation systems, all of this are of great

societal and economical significance. Additionally, the domain of dusty plasmas aligns with environmental and industrial applications, dynamics of aerosol, plasma-assisted material processing, and semiconductor manufacturing.

Finally, the interdisciplinary nature of this work contributes to scientific education and capacity building by training researchers equipped to address complex problems across plasma physics, space science, and materials research.

5.3 Future Scope

Several aspects for future research naturally emerge from the current work. Extending our analysis to the nonlinear regimes would help us in the study of wave saturation, mode coupling, and turbulent transport in dusty plasmas. Taking into account the time-dependent dust charging, non-Maxwellian particle distributions, and distributions of dust grain size would further enhance the applicability of theoretical models. Future works may also explore three-dimensional geometries, non-uniform or curved magnetic fields, and rotating dusty plasmas, which are relevant to both laboratory and astrophysical environments. Combining analytical models with advanced numerical approaches, such as hybrid PIC–MD simulations, would allow analysis of parameter regimes beyond the reach of linear theory.

On the experimental side, targeted laboratory studies could be designed to verify the predicted roles of strong coupling, dust polarization, and beam-driven instabilities. Such experimental validation would strengthen the theoretical framework and improve its applicability to real plasma systems. In summary, this thesis provides a solid foundation for understanding wave phenomena and instabilities in dusty plasmas and opens multiple pathways for future research with relevance to laboratory, fusion, space, and astrophysical plasma science.